

Coherent Photoproduction of π^0 -Meson from the Deuteron Including Polarization Effects*

Eed M. Darwish^{1,2,†}

¹Physics Department, Faculty of Science, Sohag University, Sohag 82524, Egypt

²Physics Department, Faculty of Science, Taibah University,

P. O. Box 30002, Al-Madinah Al-Munawarah 41411, Saudi Arabia

(Dated: February 13, 2018)

Coherent photoproduction of π^0 -meson from the deuteron is investigated within an approach which includes the reaction amplitudes of the impulse approximation, two-step process with intermediate πN - and ηN -rescattering, and the higher order terms in the multiple scattering series for the intermediate ηNN interaction. This approach is based on realistic separable representations of the driving two-body interaction in the πN , ηN , and NN subsystems. For the elementary $\gamma N \rightarrow \pi N$ operator, the unitary isobar model MAID2007 is used which describes well the elementary reaction. The radial deuteron wave function in the initial and final states are taken from the realistic CD-Bonn potential. Results for unpolarized and polarized cross sections as well as for all possible polarization observables with polarized photons and/or oriented deuterons are predicted and compared with available data, and differences with other theoretical models are analyzed. The contribution of $\gamma d \rightarrow \pi^0 d$ to the deuteron spin asymmetry is calculated and its contribution to the Gerasimov-Drell-Hearn (GDH) integral is explicitly evaluated by integration up to a photon lab-energy of 900 MeV. The helicity E -asymmetry is also estimated. This work is motivated by the measurements of the CLAS Collaboration at Jefferson laboratory, where a cusp-like structure in the energy dependence of the differential cross section has been observed near η -production threshold at extremely backward pion angles, and the measurements of the VEPP-3 electron storage ring, where very recent data for the tensor-deuteron spin asymmetries have been measured. The effect of intermediate ηNN three-body interaction is significant in certain spin asymmetries, specially at extreme backward pion angles. It turns out that the inclusion of a full ηNN three-body contribution is quite essential. At forward angles, the contribution from the pure impulse approximation is dominated. The sensitivity of the obtained results to the elementary $\gamma N \rightarrow \pi N$ amplitude and the choice of the NN potential model governs the deuteron wave function is investigated and considerable dependences are found. Compared to the experimental data from CLAS Collaboration for differential cross section, from YerPhi Collaboration for the linear photon asymmetry, and from VEPP-3 electron storage ring for the tensor target asymmetries, sizeable discrepancies are found.

PACS numbers: 13.60.Le, 25.20.Lj, 24.70.+s, 21.45.-v, 14.20.-c, 11.55.Hx, 25.30.Fj, 29.25.Pj, 11.55.Hx

Keywords: Meson production, Photoproduction reactions, Polarization phenomena in reactions, Few-Body Systems, Spin observables, Sum rules, Final-state interactions, Polarized beams, Polarized targets.

Contents

I. Introduction and Physics Motivation	2	C. Target Asymmetries for Polarized Deuterons	13
II. The Theoretical Model	4	D. Beam-Target Asymmetries for Circularly Polarized Photons and Polarized Deuterons	14
A. Kinematics and Cross Section	4	E. Beam-Target Asymmetries for Linearly Polarized Photons and Polarized Deuterons	15
B. Definition of Polarization Observables	5	F. Spin Asymmetries of the Total Cross Section	16
C. The $\gamma d \rightarrow \pi^0 d$ Amplitude	7	G. Helicity-Dependent Cross Sections	16
1. The Impulse Approximation	8	H. The Helicity E-Asymmetry	19
2. The Rescattering Effects	9	I. Contribution of $\gamma d \rightarrow \pi^0 d$ to the Deuteron GDH Integral	20
III. Results and Discussion	11	J. Sensitivity to the Elementary $\gamma N \rightarrow \pi N$ Amplitude	21
A. Differential and Total Cross Sections	11	K. Dependence on Modern NN Potential Models	22
B. Beam Asymmetry for Linearly Polarized Photons	13	L. Comparison with Experimental Data and Other Theoretical Models	27
		IV. Conclusions and Outlook	31
		Acknowledgments	33
		A. Explicit Expressions for Unpolarized Differential Cross Section and Various Spin	

*Will be submitted to the Permanent Scientific Committee of Physics (Egypt) in partial fulfillment of the requirements for the scientific title *Professor* in *Theoretical Nuclear Physics*.

[†]Electronic address: darwish@science.sohag.edu.eg

Asymmetries	33
B. An Elementary Pion Photoproduction Operator	34
C. Three-body treatment of the ηNN interaction	35
References	37

I. INTRODUCTION AND PHYSICS MOTIVATION

The determination of the dynamics underlying single pion production has been a major challenge in hadronic physics for several decades. However, despite this long history and large efforts in both theory and experiment, the reaction mechanisms are still far from being understood, mainly because of the contributions from a substantial number of hadronic resonances which are difficult to disentangle.

New perspectives for the study of these resonances have been opened by the possibility of performing experiments using linearly or circularly polarized photon beams and polarized targets, e.g. at MAMI in Mainz and ELSA in Bonn (Germany), at JLab in Newport News and LEGS in Brookhaven (USA), at MAX-Lab in Lund (Sweden), at SPring-8 in Osaka and ELPH in Tohoku University (Japan), at GRAAL in Grenoble (France), and at VEPP-2 and VEPP-3 electron storage rings in Novosibirsk (Russia). A comprehensive overview concerning the status of these experiments is given in Ref. [1]. By careful selection of the new observables, enhanced sensitivities to specific electromagnetic multipoles and, consequently, to a few selected hadronic resonances are obtained. The use of polarization degrees of freedom allows one also to obtain complete information on all possible reaction matrix elements. Furthermore, polarization observables are expected to be sensitive to important dynamical details and thus allow in general much more stringent tests of theoretical models.

Therefore, a lot of valuable information about the structure of nucleons and nuclei can be obtained, in particular, in high precision experiments on pion photoproduction, including measurements of polarization observables. Regarding pion photoproduction from the nucleon, the most understood channels are the proton ones since a relatively large number of experimental data are available for these channels at energies up to 2 GeV (see the SAID database [2]). Meanwhile, the study of neutron channels is needed to complete our understanding about pion photoproduction from the nucleon. Since free neutron targets are not available to study the neutron channels, one needs to use light nuclei such as the deuteron or ^3He as effective neutron targets. The deuteron is particularly well suited because of its small binding energy and its simple structure.

Electromagnetic pion production from the deuteron is of fundamental interest and thus constitute a major topic in medium energy nuclear physics. One of the interesting aspects is that it can provide complementary information on the elementary pion production process on the nucleon. Studying pion production from the deuteron can also give information on pion production on off-shell nucleons. This is of course important for the study of pion production on all other nuclei as well. With respect to pion production from the deuteron, the coherent and incoherent reactions are worth to be studied. Coherent pion production from the deuteron may be used as an isospin filter and is especially sensitive to the coherent sum of the $\gamma p \rightarrow \pi^0 p$ and $\gamma n \rightarrow \pi^0 n$ amplitudes. On the other hand, incoherent pion production from the deuteron may be used to obtain information about neutron cross section in quasifree kinematics. In this work, we focus our attention on the coherent π^0 -photoproduction reaction from the deuteron in the energy region near the η -production threshold. This study is motivated by the measurements of the CLAS Collaboration at Jefferson Laboratory [3, 4] for the differential cross section, the YerPhi Collaboration [5] for the linear photon asymmetry, and the VEPP-2 and VEPP-3 electron storage rings [6–8] for the tensor target asymmetries. This study is of interest both for development of theory and future experimental investigations.

Previously, coherent π^0 -photoproduction from the deuteron has been studied extensively at photon lab-energies below 400 MeV as a source of information on the elementary π^0 -photoproduction on the neutron [9–15]. This reaction is characterized by high momentum transfer at large pion center-of-mass (c.m.) production angles. Thus, one expects that rescattering mechanisms, such as two-step process, dominate the reaction dynamics at this kinematics and the reaction can be used to study these. The reaction $\gamma d \rightarrow \pi^0 d$ has been first studied in Ref. [9] by including the contribution from pion rescattering with charge-exchange contributions. This effect was then verified in studies of this reaction in the π -threshold region [10]. An approach of $NN - N\Delta$ coupled channels for describing the reaction $\gamma d \rightarrow \pi^0 d$ in the $\Delta(1232)$ -resonance region was used in Ref. [11], whereas relativistic Feynman diagrams have been evaluated in another approach developed in [12]. Blaazer *et al.* [13] studied rescattering corrections to all orders by solving Faddeev equations of the πNN system. They have concluded that the contributions of the neutron and the proton cannot be separated because of the charge-exchange rescattering of the pion. Using a microscopic approach based on the Kerman-McManus-Thaler (KMT) multiple scattering theory [14] in momentum space, Kamalov *et al.* [15] have studied the reaction $\gamma d \rightarrow \pi^0 d$ in the $\Delta(1232)$ -resonance region in a coupled channel approach.

The reaction $\gamma d \rightarrow \pi^0 d$ is quite well understood at energies between π -threshold and the $\Delta(1232)$ resonance region. But this reaction is not well understood at higher energies, because the resonances and mechanism of mul-

multiple scattering play an important role for description of the process. For more than a decade, the CLAS Collaboration has been carrying out intense experimental studies aimed at the investigation of the reaction $\gamma d \rightarrow \pi^0 d$ near the η -production threshold at backward c.m. pion angles [3, 4]. It was found that the unpolarized differential cross section showed at extreme backward pion angles an indication of a cusp-like structure between 600 and 800 MeV. This nontrivial energy dependence of the differential cross section was explained in [16] within a model which based on the impulse approximation (IA) and first-order rescattering approximation with intermediate production of both π - and η -mesons (henceforth denoted by FOR). It was demonstrated that the first-order rescattering with intermediate ηN -rescattering dominates over IA and intermediate πN -rescattering, and can explain the cusp structure experimentally observed by the CLAS Collaboration [3, 4]. Later on, this effect was analyzed in Ref. [17] on the basis of a theoretical model which includes, in addition to the IA and FOR, the full dynamics in the intermediate ηNN three-body system only in the s -wave state 1S_0 [$J^\pi = 0^-, T = 1$] (in what follows denoted by TBM). Results for only the unpolarized differential cross section were given in [17]. It was concluded that a three-body treatment of the intermediate ηNN interaction is of special importance.

We would like to emphasize that the calculations of Refs. [16, 17] do not explain the features of entire set of available data. The differential cross section was found to be revealed remarkable differences even if the rescattering effects are included. Furthermore, none of these theoretical studies consider polarization observables for the reaction $\gamma d \rightarrow \pi^0 d$ near the threshold of η -production and/or investigate the sensitivity of results to the elementary $\gamma N \rightarrow \pi^0 N$ amplitude and to the choice of NN potential model governs the deuteron wave function. Indeed, polarization observables constitute much more stringent tests of theoretical models, being more sensitive to small, but interesting amplitudes.

Therefore, in Ref. [18] we have considered the reaction $\gamma d \rightarrow \pi^0 d$ in the pure IA with special emphasize on polarization observables. This work was improved and extended in Refs. [19, 20] to study the influence of FOR on differential and total cross sections as well as on polarization observables. The justification for this work was to investigate the influence of two-body process on polarization observables which, to the best of our knowledge, had not been considered before in the literature in the kinematics of the current situation. It was reported that the differential cross section as well as polarization observables are influenced by the inclusion of two-step process. In many cases, the deviation among results obtained using the pure IA alone and with inclusion of FOR was found to be large. Nevertheless, perturbative models, like two-body process approximation noted in Refs. [16, 19, 20], where only the leading order terms are kept in the multiple scattering series, are unable to reproduce the real dynamics of the intermediate ηNN system. In

addition, the comparison of theoretical predictions and the experimental data from [3, 4, 21] for the differential cross section in Ref. [20] as well as in the previous study of Ref. [17] gave clear indication that a genuine three-body treatment of the intermediate ηNN interaction is required. This effect can not be described within the perturbative approach and requires three-body formalism.

Recently, the role of complete ηNN three-body calculation on various observables for the reaction $\gamma d \rightarrow \pi^0 d$ near the η -production threshold at backward c.m. pion angles was investigated in Refs. [22–28]. Results for unpolarized differential and total cross sections as well as for all possible polarization observables with polarized photons and/or oriented deuterons were given in said work. Also, the sensitivity of results to the elementary $\gamma N \rightarrow \pi^0 N$ amplitude and the NN potential model governs the deuteron wave function was investigated. The main concern of this work was to see to what extent the full dynamics in the intermediate ηNN interaction will influence the dynamical properties of the $\gamma d \rightarrow \pi^0 d$ reaction. It was found that the effect of intermediate ηNN interaction is significant in certain spin asymmetries at extreme backward pion angles. The interference of the pure IA and complete three-body calculation was found to be quite important for understanding the reaction dynamics. In addition, the deviation among results obtained using different elementary amplitudes and deuteron wave functions was very large.

In the following, we would like to explain the main differences between the calculation presented in Ref. [24] and the previous one given in Ref. [17]. First of all, the author of Ref. [17] was used for the elementary $\gamma N \rightarrow \pi N$ amplitude the unitary isobar model MAID2003 [29], while the extended version MAID2007 [30] is used in [24]. The latter is well adopted for predictions and analysis of the observables in pion photo- and electroproduction. It describes the elementary production amplitude in a consistent way and provides a well-defined transition from the elementary process to the nuclear process. The sensitivity of the results for differential and total cross sections as well as for polarization observables with inclusion of the full dynamics in the intermediate ηNN system to the elementary $\gamma N \rightarrow \pi N$ amplitude and the deuteron wave function was investigated in [22–26], but this has not been studied in Ref. [17]. To the best of our knowledge, this has not been done previously in the current kinematics. In Ref. [17], the results for differential cross section was compared with the, at that time, preliminary data from CLAS Collaboration [3], but our calculations presented in [22–26] are compared with the published version of CLAS data [4]. In Refs. [22–26], we also investigated the role of three-body effect in the intermediate ηNN interaction on polarization observables, but there are no calculations for these observables were given in Ref. [17]. Indeed, the influence of rescattering effects on polarization observables may be an important question. Finally, the author of Ref. [17] gives no total cross section results. We will return to this point in section III

(subsection III L).

Experimental data on the $\gamma d \rightarrow \pi^0 d$ observables with a polarized photon beam and/or a polarized deuteron target exist only for the linear photon asymmetry Σ and the tensor target spin asymmetries T_{2M} ($M=0,1,2$). The linear photon Σ asymmetry has been measured at $\theta=130^\circ$ in the c.m. system by the YerPhi Collaboration in Yerevan [5]. With regard to the deuteron spin asymmetries, the tensor target asymmetries T_{2M} ($M=0,1,2$) have been measured so far only at the VEPP-2 and VEPP-3 electron storage rings in Novosibirsk [6]. In the recent years, the tensor deuteron spin asymmetry T_{20} has been measured for a photon energy range 200-600 MeV and for a c.m. pion angle range 90° - 140° [7, 8]. A theoretical understanding of these experimental data may provide new information about the pion photoproduction amplitude on the free neutron, which is not well known yet, but is required for a complete understanding of the Δ -excitations in the pion photoproduction process. To the best of our knowledge, there are no photon-deuteron spin asymmetries in the $\gamma d \rightarrow \pi^0 d$ process have been measured yet.

The calculations presented in this review are of high interest because, on the one hand, it provides an important test of our understanding of the elementary neutron amplitude in the absence of a free neutron target. On the other hand, we would like to see whether the cusp structure observed in the differential cross section at backward direction by the CLAS Collaboration [3, 4] can be explored via polarization observables.

This review is structured as follows. In the next section we briefly outline the theoretical model for coherent photoproduction of π^0 -meson from the deuteron. The kinematical framework used for our calculation of the $\gamma d \rightarrow \pi^0 d$ reaction is given in this section. Formal expressions for the unpolarized cross section and various polarization observables are also given section II. The essential ingredients for the calculation of the scattering matrix in the pure IA and with the inclusion of rescattering contributions are also described. The results on the unpolarized differential and total cross sections as well as on various polarization observables for the $\gamma d \rightarrow \pi^0 d$ reaction are presented and discussed in section III together with a comparison with available experimental data and other theoretical models. The last section IV is devoted to conclusions and outlook. Throughout this work we use natural units $\hbar = c = 1$.

II. THE THEORETICAL MODEL

A. Kinematics and Cross Section

As a starting point, we briefly outline the kinematic framework for coherent π^0 -photoproduction from the deuteron which contains only two particles in the initial and in the final states. The general form of the two-body

reaction is

$$a(p_a) + b(p_b) \rightarrow c(p_c) + d(p_d), \quad (1)$$

where $p_i = (E_i, \vec{p}_i)$ denotes the four-momentum of particle “ i ” with $i \in \{a, b, c, d\}$.

Following the conventions of Bjorken and Drell [31], the general form for the differential cross section of a two-particle reaction in the c.m. system is given by

$$\frac{d\sigma}{d\Omega_c} = \frac{1}{(2\pi W)^2} \frac{p_c}{p_a} \frac{E_a E_b E_c E_d}{F_a F_b F_c F_d} \frac{1}{s} \times \sum_{\mu_d \mu_c \mu_b \mu_a} |\mathcal{M}_{\mu_d \mu_c \mu_b \mu_a}^{fi}(\vec{p}_d, \vec{p}_c, \vec{p}_b, \vec{p}_a)|^2 \quad (2)$$

with $\mathcal{M}_{\mu_d \mu_c \mu_b \mu_a}^{fi}$ as reaction matrix, μ_i denoting the spin projection of particle “ i ” on some quantization axis, and F_i is a factor arising from the covariant normalization of the states and its form depends on whether the particle is a boson ($F_i = 2E_i$) or a fermion ($F_i = E_i/m_i$), where E_i and m_i are its energy and mass, respectively. The factor $s = (2s_a + 1)(2s_b + 1)$ takes into account the averaging over the initial spin states, where s_a and s_b denote the spins of the incoming particles a and b , respectively. If particle a is a real photon, then $s_a = 1/2$ because the real photon is a boson with two polarization states. All momenta are functions of the invariant mass of the two-body system W , i.e. $p_i = p_i(W)$, where $W = E_a + E_b = E_c + E_d$.

Now, we focus on coherent π^0 -photoproduction from the deuteron

$$\gamma(q, \vec{\epsilon}_\lambda) + d(d) \rightarrow \pi^0(k) + d(d'), \quad (3)$$

where $q = (E_\gamma, \vec{q})$, $k = (E_\pi, \vec{k})$, $d = (E_d, \vec{d})$, and $d' = (E'_d, \vec{d}')$ denote the four-momenta of the incident photon, outgoing pion, initial and final deuterons, respectively. The circular polarization vector of the incoming photon is defined by $\vec{\epsilon}_\lambda$ with $\lambda = \pm 1$. The F_i factor is given by

$$F_a = 2E_\gamma, \quad F_b = 2E_d, \quad F_c = 2E_\pi, \quad F_d = 2E'_d \quad (4)$$

and therefore one finds $s = 6$ taking into account the averaging of the cross section over the initial two possible polarizations of the real photon and the three spin projections of the deuteron. For the deuteron states, a non-covariant notation is used which removes the standard additional factors $1/2E_d$ and $1/2E'_d$.

For the description of cross sections and polarization observables, we consider the reaction (3) in the photon-deuteron (γd) c.m. frame. There, we choose the z -axis pointing in the direction of the incoming photon momentum \vec{q} ($\vec{e}_z = \hat{q} = \vec{q}/q$) which also serves as quantization axis for the deuteron spin states. The direction of the outgoing meson momentum \vec{k} is characterized by the spherical angles (θ, ϕ) with $\cos\theta = \hat{k} \cdot \hat{q}$. It defines together with the photon momentum the reaction plane. The geometry is shown in Fig. 1. If the incoming photon beam is not linearly polarized, then the x -axis may

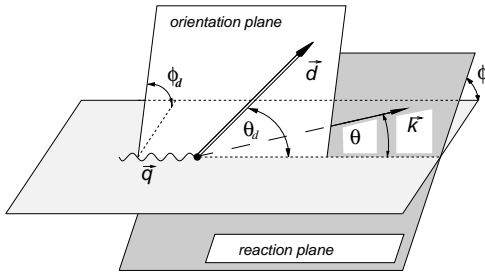


FIG. 1: Kinematical variables of the coherent π^0 -photoproduction reaction from the deuteron in the γd c.m. frame.

be chosen arbitrarily, as there is no dependence on the angle ϕ .

Using standard normalization of particle states, the unpolarized differential cross section of the reaction $\gamma d \rightarrow \pi^0 d$ in the c.m. system is then given from (2) by

$$\frac{d\sigma}{d\Omega_\pi} = \frac{\mathcal{K}}{6} \sum_{m_d \lambda m'_d} \left| \mathcal{M}_{m_d \lambda m'_d}^{fi}(\vec{q}, \vec{k}) \right|^2, \quad (5)$$

where m_d and m'_d are the initial and final deuteron spin projections, respectively. The kinematic factor \mathcal{K} is given in the γd c.m. frame by

$$\mathcal{K} = \frac{1}{16\pi^2} \frac{k}{q} \frac{E_d E'_d}{W_{\gamma d}^2}, \quad (6)$$

where the initial and final deuteron energies are given by $E_d = \sqrt{q^2 + M_d^2}$ and $E'_d = \sqrt{k^2 + M_d^2}$, respectively, with M_d as deuteron mass. The c.m. three-momenta of the photon and the pion are given by \vec{q} and \vec{k} , respectively. The absolute values of these quantities are given as functions of the photon energy in the laboratory frame by

$$q = \frac{1}{2W_{\gamma d}} (W_{\gamma d}^2 - M_d^2) = E_\gamma \quad (7)$$

and

$$k = \frac{\sqrt{[W_{\gamma d}^2 - (M_d - m_\pi)^2][W_{\gamma d}^2 - (M_d + m_\pi)^2]}}{2W_{\gamma d}}. \quad (8)$$

Moreover, the invariant energy of the γd system is given as

$$\begin{aligned} W_{\gamma d} &= E_\gamma + E_d = |\vec{q}| + \sqrt{q^2 + M_d^2}, \\ &= E_\pi + E'_d = \sqrt{k^2 + m_\pi^2} + \sqrt{k^2 + M_d^2}, \end{aligned} \quad (9)$$

where m_π is the pion mass.

B. Definition of Polarization Observables

The cross section for arbitrary polarized photons and initial deuterons can be computed for a given \mathcal{M} -matrix

by applying the density matrix formalism similar to that given for deuteron photodisintegration [32]. All observables for coherent π^0 -photoproduction from the deuteron have the general form

$$\begin{aligned} \mathcal{O} &= \mathcal{K} \sum_{\tilde{m}'_d \tilde{\lambda} \tilde{m}_d} \sum_{m'_d \lambda m_d} \mathcal{M}_{\tilde{m}'_d \tilde{\lambda} \tilde{m}_d}^* \Omega_{\tilde{m}'_d m'_d} \mathcal{M}_{m'_d \lambda m_d} \\ &\times \rho_{\tilde{\lambda} \tilde{\lambda}}^\gamma \rho_{m_d \tilde{m}_d}^d, \end{aligned} \quad (10)$$

where ρ^γ and ρ^d are the density matrices for incoming photon and initial deuteron polarization, respectively. A polarimeter for final deuterons would be formally described by the operator Ω . However, in this work, we will always set $\Omega = 1$, i.e., we do not consider any polarization analysis of the outgoing deuteron.

The direction of the x -axis is defined by the density matrix of the photon polarization with respect to the basis of circular polarization states. The initial state density matrix of the photon has the form [33]

$$\rho_{\lambda \lambda'}^\gamma = \frac{1}{2} \left(\delta_{\lambda \lambda'} + \vec{P}^\gamma \cdot \vec{\sigma}_{\lambda \lambda'} \right), \quad \lambda, \lambda' = \pm 1, \quad (11)$$

where $\vec{\sigma}$ denotes the Pauli spin operator. Here, $|\vec{P}^\gamma|$ describes the total degree of polarization, $P_z^\gamma = P_c^\gamma$ the degree of circular photon polarization and $P_l^\gamma = \sqrt{(P_x^\gamma)^2 + (P_y^\gamma)^2}$ the degree of linear photon polarization. By a proper rotation of the frame of reference around the z -axis, i.e., around the photon momentum \vec{q} one can choose the x -axis in the direction of maximum linear polarization, i.e., $P_x^\gamma = -P_l^\gamma$ and $P_y^\gamma = 0$. Thus, we have explicitly [33]

$$\rho_{\lambda \lambda'}^\gamma = (1 + \lambda P_c^\gamma) \delta_{\lambda \lambda'} - P_l^\gamma \delta_{\lambda, -\lambda'} e^{2i\lambda\phi}. \quad (12)$$

A possible target orientation is described by the deuteron density matrix ρ^d which can be expressed in terms of the irreducible spin operators $\tau^{[I]}$ with respect to the deuteron spin space [33]

$$\rho_{m_d m'_d}^d = \frac{1}{3} \sum_{I=0}^2 \sum_{M=-I}^I (-)^M \hat{I} \langle 1m_d | \tau^{[I]} | 1m'_d \rangle P_{I-M}^d, \quad (13)$$

where P_{IM}^d characterizes the initial state polarization, $P_{00}^d = 1$, and P_{1-M}^d and P_{2-M}^d describe vector and tensor polarization components of the deuteron, respectively. Furthermore, we use throughout the notation $\hat{I} = \sqrt{2I+1}$. The spin operators are defined by their reduced matrix elements

$$\langle 1 || \tau^{[I]} || 1 \rangle = \sqrt{3} \hat{I} \quad \text{for } I = 0, 1, 2. \quad (14)$$

In view of the experimental methods for orienting deuterons, it is sufficient to assume that the deuteron density matrix is diagonal; the elements with $m_d \neq m'_d$ will therefore vanish, with respect to a certain orientation axis \vec{d} . This axis is characterized by spherical angles θ_d and ϕ_d with respect to the coordinate system associated

with the scattering plane in the γd c.m. frame. Then, one has with respect to \vec{d} as quantization axis

$$\rho_{m_d m'_d}^d = p_{m_d} \delta_{m_d m'_d}, \quad (15)$$

where p_{m_d} denotes the probability for finding the deuteron in a state $|1m_d\rangle$ with respect to an orientation axis parallel to the z -axis, the orientation parameters have a particularly simple form [33]

$$P_{IM}^d(\vec{d}) = P_I^d \delta_{M0}, \quad (16)$$

where the orientation parameters P_I^d are related to the p_{m_d} by

$$\begin{aligned} P_I^d &= \sqrt{3} \hat{I} \sum_{m_d} (-)^{1-m_d} \begin{pmatrix} 1 & 1 & I \\ m_d & -m_d & 0 \end{pmatrix} p_{m_d} \\ &= \delta_{I0} + \sqrt{\frac{3}{2}} (p_1 - p_{-1}) \delta_{I1} \\ &\quad + \frac{1}{\sqrt{2}} (1 - 3p_0) \delta_{I2}. \end{aligned} \quad (17)$$

The orientation parameters with respect to the photon momentum as quantization axis are obtained by the rotation

$$\begin{aligned} P_{IM}^d(\vec{z}) &= P_I^d D_{0M}^I(0, -\theta_d, -\phi_d) \\ &= P_I^d e^{iM\phi_d} d_{M0}^I(\theta_d), \quad (I = 1, 2), \end{aligned} \quad (18)$$

where D_{0M}^I denotes a rotation matrix [34, 35] describing the transformation of irreducible tensors under a spatial rotation, $d_{mm'}^j$ denotes a small rotation matrix. Correspondingly, the deuteron density matrix with the basis states $|1m_d\rangle$ becomes

$$\begin{aligned} \rho_{m_d m'_d}^d &= \langle 1m'_d | \rho^d | 1m_d \rangle \\ &= \frac{1}{\sqrt{3}} (-)^{1-m_d} \sum_{I=0}^2 P_I^d \sum_{M=-I}^I \hat{I} \\ &\quad \times \begin{pmatrix} 1 & 1 & I \\ m'_d & -m_d & M \end{pmatrix} e^{-iM\phi_d} d_{M0}^I(\theta_d), \end{aligned} \quad (19)$$

where the symbol in round brackets denotes the Wigner $3j$ -symbol for which we use the convention of Edmonds [35]. This means, the deuteron target is characterized by four parameters, namely the vector and tensor polarization parameters P_1^d and P_2^d , respectively, and by the orientation angles θ_d and ϕ_d .

Formal expressions for the differential cross section in coherent pseudoscalar meson photoproduction from an oriented deuteron target have been given in [11, 13] in terms of beam, target and beam-target spin asymmetries. Here, we follow the more general approach of [36]. The general form of the differential cross section can be described by the unpolarized differential cross section and

various spin asymmetries as follows

$$\begin{aligned} \frac{d\sigma}{d\Omega} &= \frac{d\sigma_0}{d\Omega} \left[1 + P_I^\gamma \left\{ \Sigma \cos 2\phi \right. \right. \\ &\quad \left. \left. + \sum_{I=1}^2 P_I^d \sum_{M=-I}^I T_{IM}^l \cos[\psi_M - \delta_{I1} \frac{\pi}{2}] d_{M0}^I(\theta_d) \right\} \right. \\ &\quad \left. + \sum_{I=1}^2 P_I^d \sum_{M=0}^I \left(T_{IM} \cos[M(\phi_d - \phi) - \delta_{I1} \frac{\pi}{2}] \right. \right. \\ &\quad \left. \left. + P_c^\gamma T_{IM}^c \sin[M(\phi_d - \phi) + \delta_{I1} \frac{\pi}{2}] \right) d_{M0}^I(\theta_d) \right], \end{aligned} \quad (20)$$

where $\psi_M = M(\phi_d - \phi) + 2\phi$. This expression defines the unpolarized differential cross section $d\sigma_0/d\Omega$ and the various photon, deuteron, and photon-deuteron asymmetries Σ , T_{IM} , T_{IM}^c , and T_{IM}^l as functions of the scattering angle θ . In order to express these observables in terms of the reduced t -matrix, it is convenient to define, in complete analogy to the procedure for deuteron photodisintegration in Ref. [32], the two quantities

$$\begin{aligned} \mathcal{V}_{IM} &= \frac{\mathcal{K}}{\sqrt{3}} \hat{I} \sum_{m'_d m_d} (-)^{1-m_d} \begin{pmatrix} 1 & 1 & I \\ m'_d & -m_d & M \end{pmatrix} \\ &\quad \times \sum_{m'_d} t_{m'_d 1 m'_d}^* t_{m'_d 1 m_d}, \end{aligned} \quad (21)$$

and

$$\begin{aligned} \mathcal{W}_{IM} &= -\frac{\mathcal{K}}{\sqrt{3}} \hat{I} \sum_{m'_d m_d} (-)^{1-m_d} \begin{pmatrix} 1 & 1 & I \\ m'_d & -m_d & M \end{pmatrix} \\ &\quad \times \sum_{m'_d} t_{m'_d 1 m'_d}^* t_{m'_d -1 m_d}. \end{aligned} \quad (22)$$

Then, the unpolarized differential cross section and various spin asymmetries can be derived as follows [11]:

(i) The unpolarized differential cross section:

$$\frac{d\sigma_0}{d\Omega} = \mathcal{V}_{00}. \quad (23)$$

(ii) The photon asymmetry for linearly polarized photons and unpolarized deuterons:

$$\Sigma \frac{d\sigma_0}{d\Omega} = \mathcal{W}_{00}. \quad (24)$$

(iii) The target asymmetry for vector polarized deuterons and unpolarized photons:

$$T_{11} \frac{d\sigma_0}{d\Omega} = 2 \Im m \mathcal{V}_{11}. \quad (25)$$

(iv) The target asymmetries for tensor polarized deuterons and unpolarized photons:

$$T_{2M} \frac{d\sigma_0}{d\Omega} = (2 - \delta_{M0}) \Re e \mathcal{V}_{2M}, \quad \text{for } 0 \leq M \leq 2. \quad (26)$$

(v) The beam-target double spin asymmetries for circularly polarized photons and vector polarized deuterons:

$$T_{1M}^c \frac{d\sigma_0}{d\Omega} = -(2 - \delta_{M0}) \Re e \mathcal{V}_{1M}, \quad \text{for } 0 \leq M \leq 1. \quad (27)$$

(vi) The beam-target double spin asymmetries for circularly polarized photons and tensor polarized deuterons:

$$T_{2M}^c \frac{d\sigma_0}{d\Omega} = -(2 - \delta_{M0}) \Im m \mathcal{V}_{2M}, \quad \text{for } 0 \leq M \leq 2. \quad (28)$$

(vii) The beam-target double spin asymmetries for linearly polarized photons and vector polarized deuterons:

$$T_{1M}^l \frac{d\sigma_0}{d\Omega} = i \mathcal{W}_{1M}, \quad \text{for } -1 \leq M \leq 1. \quad (29)$$

(viii) The beam-target double spin asymmetries for linearly polarized photons and tensor polarized deuterons:

$$T_{2M}^l \frac{d\sigma_0}{d\Omega} = \mathcal{W}_{2M}, \quad \text{for } -2 \leq M \leq 2. \quad (30)$$

Because the quantity \mathcal{V}_{I0} is real according to the following property under complex conjugation

$$\mathcal{V}_{IM}^* = (-)^M \mathcal{V}_{I-M}, \quad (31)$$

the asymmetries T_{10} and T_{20}^c vanish identically. We would like to point out that in extremely forward and backward pion emission, i.e. for $\theta = 0$ and π , the following spin asymmetries have to vanish

$$\begin{aligned} \Sigma &= 0, \\ T_{IM} &= 0 \quad \text{for } M \neq 0, \\ T_{IM}^c &= 0 \quad \text{for } M \neq 0, \\ T_{IM}^l &= 0 \quad \text{for } M \neq 2, \end{aligned} \quad (32)$$

because in that case the differential cross section cannot depend on the azimuthal angle ϕ , since at $\theta = 0$ or π the angle ϕ is undefined or arbitrary. For completeness, we list in Appendix A the explicit expressions for unpolarized differential cross section and various spin asymmetries in terms of the reduced t -matrix elements.

The spin asymmetry with respect to circularly polarized photons and the deuteron spin oriented parallel (P) and antiparallel (A) to the photon spin is related to the beam-target double spin asymmetry T_{10}^c according to [33]

$$\frac{d(\sigma^P - \sigma^A)}{d\Omega} = \sqrt{6} \frac{d\sigma_0}{d\Omega} T_{10}^c. \quad (33)$$

The asymmetry T_{10}^c is of special interest, because it is related to the spin asymmetry $\sigma^P - \sigma^A$ which determines the Gerasimov-Drell-Hearn (GDH) sum rule [37].

Finally, the general form of the total cross section with inclusion of photon and deuteron polarization effects is

obtained from (20) by integrating $d\sigma/d\Omega$ over the pion spherical angle $d\Omega$ and reads [33]

$$\begin{aligned} \sigma(P_l^\gamma, P_c^\gamma, P_1^d, P_2^d) &= \sigma_0 \left[1 + P_2^d \tilde{T}_{20} \frac{1}{2} (3 \cos^2 \theta_d - 1) \right. \\ &\quad \left. + P_c^\gamma P_1^d \tilde{T}_{10}^c \cos \theta_d \right. \\ &\quad \left. + P_l^\gamma P_2^d \tilde{T}_{22}^l \cos(2\phi_d) \frac{\sqrt{6}}{4} \sin^2 \theta_d \right]. \end{aligned} \quad (34)$$

It is clear that in this form only a few spin asymmetries survive. The unpolarized total cross section σ_0 and the corresponding spin asymmetries \tilde{T}_{20} , \tilde{T}_{10}^c and \tilde{T}_{22}^l are given by

$$\sigma_0 = \int d\Omega \frac{d\sigma_0}{d\Omega}, \quad (35)$$

$$\sigma_0 \tilde{T}_{20} = \int d\Omega \frac{d\sigma_0}{d\Omega} T_{20}, \quad (36)$$

$$\sigma_0 \tilde{T}_{10}^c = \int d\Omega \frac{d\sigma_0}{d\Omega} T_{10}^c, \quad (37)$$

$$\sigma_0 \tilde{T}_{22}^l = \int d\Omega \frac{d\sigma_0}{d\Omega} T_{22}^l. \quad (38)$$

C. The $\gamma d \rightarrow \pi^0 d$ Amplitude

To obtain the scattering \mathcal{M} -amplitude of coherent π^0 -photoproduction from the deuteron, one may start with the amplitude of the pure IA, i.e., the one-body contribution, to which the contributions from FOR and TBM are added. A diagrammatical overview of these three contributions which are considered in the present work is given in Fig. 2. Diagrams (a), (b), and (c) in Fig. 2 describe the pure IA, the contribution from FOR, and the additional contribution from TBM, respectively. In order to avoid double counting, diagrams (d) and (e) in Fig. 2 are removed from the three-body amplitude since they possess the same topology as that already included in diagrams (a) and (b). For the calculation of diagrams (c), (d), and (e) only the s -wave state 1S_0 ($J^\pi = 0^-, T = 1$) is considered in the present work. In addition, the $T_{S_{11}}$ amplitude of photoproduction of the $S_{11}(1535)$ -resonance from the deuteron (see Fig. 3 for its diagrammatic representation) is calculated only in the s -wave state 1S_0 ($J^\pi = 0^-, T = 1$). It should be noted that diagrams when the elementary operators act on nucleon '2' are not shown in Figs. 2 and 3 but are included in the present calculations. In the calculations of the present work, each diagram shown in Figs. 2 and 3 goes accompanied by the diagram obtained by the exchange $N_1 \leftrightarrow N_2$.

We would like to mention that possible contributions from two-nucleon mechanisms to the scattering amplitude are neglected. Thus, the treatment of the \mathcal{M} -matrix is completely analogous to previous work on coherent π^0 -photoproduction from the deuteron [17], but it is performed on significantly higher level in comparison to

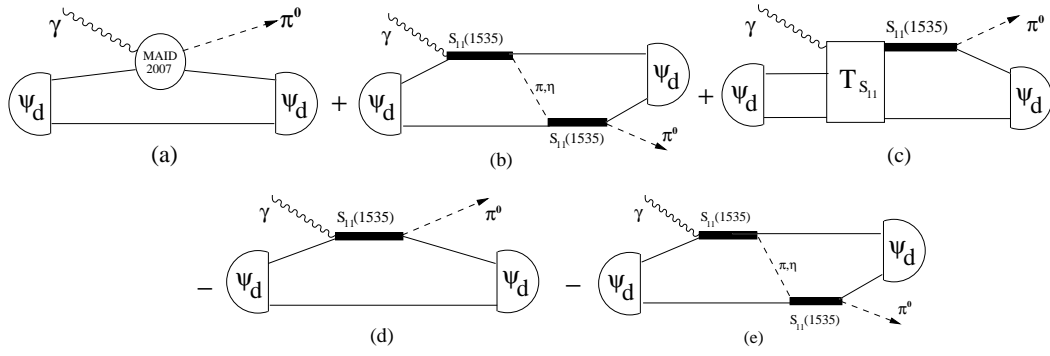


FIG. 2: The considered diagrams in coherent π^0 -photoproduction from the deuteron in the near η -threshold region, (a) impulse approximation (IA), (b) contribution from two-step process with intermediate production of both π - and η -mesons [called also first-order rescattering] (FOR), and (c) additional contribution from intermediate ηNN three-body dynamics (TBM). In order to avoid double counting, diagrams (d) and (e) are removed from the three-body amplitude since they possess the same topology as the ones already included in diagrams (a) and (b). For the calculation of diagrams (c), (d), and (e) only the s -wave state 1S_0 ($J^\pi = 0^-, T = 1$) is considered. The diagrammatic representation of the $T_{S_{11}}$ amplitude of photoproduction of the $S_{11}(1535)$ -resonance from the deuteron is shown in Fig. 3. Diagrams when the elementary operators act on nucleon '2' are not shown in the figure but are included in the calculations. In the calculations, each diagram shown in the figure goes accompanied by the diagram obtained by the exchange $N_1 \leftrightarrow N_2$.

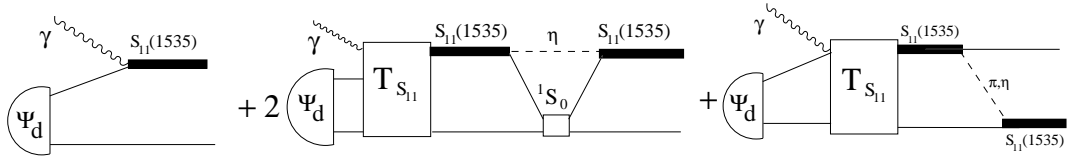


FIG. 3: Diagrammatic representation for the $T_{S_{11}}$ amplitude of photoproduction of the $S_{11}(1535)$ -resonance on the deuteron (as shown in diagram (c) of Fig. 2) calculated only in the s -wave state 1S_0 ($J^\pi = 0^-, T = 1$).

what was done in Refs. [16, 19, 20] since the full dynamics in the intermediate ηNN system was not considered in the latter works. The three contributions in diagram (a), diagrams (a)+(b), and diagrams (a)+(b)+(c) of Fig. 2 present three different successively improved levels of approximation to the reaction amplitude. In this approximation, the total transition \mathcal{M}_{fi} -matrix element is given by the sum

$$\mathcal{M}_{m_d \lambda m'_d}(\vec{q}, \vec{k}) = \mathcal{M}_{m_d \lambda m'_d}^{\text{IA}}(\vec{q}, \vec{k}) + \mathcal{M}_{m_d \lambda m'_d}^{\text{FOR}}(\vec{q}, \vec{k}) + \mathcal{M}_{m_d \lambda m'_d}^{\text{TBM}}(\vec{q}, \vec{k}). \quad (39)$$

Choosing the z -axis in the direction of the incoming photon one can expand the \mathcal{M} -matrix in spherical harmonics depending only on the pion momentum and its direction. Introducing a partial wave decomposition and isolating the azimuthal dependence, one finds for the scattering matrix the relation

$$\mathcal{M}_{m'_d \lambda m_d}^{fi}(\vec{q}, \vec{k}) = e^{i(\lambda+m_d)\phi} t_{m'_d \lambda m_d}^{fi}(W_{\gamma d}, \theta), \quad (40)$$

where the reduced t -matrix elements are defined by separating the ϕ -dependence from the \mathcal{M} -matrix elements. These matrix elements are the basic quantities that determine cross sections and polarization observables. If parity is conserved, the reduced t -matrix elements obey

the following symmetry property

$$t_{-m'_d - \lambda - m_d}^{fi}(W_{\gamma d}, \theta) = (-)^{1+m'_d + \lambda + m_d} t_{m'_d \lambda m_d}^{fi}(W_{\gamma d}, \theta). \quad (41)$$

1. The Impulse Approximation

For the IA contribution of coherent photoproduction of π^0 -meson from the deuteron (diagram (a) in Fig. 2), one has the scattering amplitude $\mathcal{M}_{m_d \lambda m'_d}^{\text{IA}}$ for the transition between the deuteron target states with spin projections m_d and m'_d on the z -axis, chosen along the photon momentum \vec{q} ,

$$\mathcal{M}_{m_d \lambda m'_d}^{\text{IA}}(\vec{q}, \vec{k}) = 2 \int \frac{d^3 p}{(2\pi)^3} \phi_{m'_d}^\dagger(\vec{p}') \times t_{\pi\gamma}^\lambda(\vec{q}, \vec{p}_i, \vec{k}, \vec{p}_f) \phi_{m_d}(\vec{p}) \quad (42)$$

with $t_{\pi\gamma}^\lambda$ denotes the corresponding elementary pion photoproduction operator on the nucleon. Furthermore, the vectors \vec{p}_i and \vec{p}_f denote the initial and final momenta of the active nucleon in the deuteron, for which we have $\vec{p}_i = \vec{p} - \vec{q}/2$ and $\vec{p}_f = \vec{p} - \vec{k} + \vec{q}/2$, and $\vec{p}' = \vec{p} + (\vec{q} - \vec{k})/2$ denotes the relative momentum in the final deuteron state.

For the deuteron wave function we use the familiar ansatz

$$\begin{aligned} \phi_{m_d}(\vec{p}) &= \sum_{L=0,2} \sum_{m_L m_S} (L m_L 1 m_S | 1 m_d) u_L(p) \\ &\times Y_{L m_L}(\hat{p}) \chi_{m_S} \zeta_0, \end{aligned} \quad (43)$$

where χ_{m_S} and ζ_0 denote spin and isospin wave functions, respectively. The S and D components of the deuteron wave function are given by $u_0(p)$ and $u_2(p)$, respectively. In the present work, we compute the radial deuteron wave function in the initial and final states using the realistic high-precision CD-Bonn potential form [38].

For nuclear application it is convenient to split the elementary pion photoproduction amplitude $t_{\pi\gamma}^\lambda$, involving an invariant product between the photon polarization ϵ_μ and the electromagnetic current J_μ , into spin independent and spin-flip amplitudes as follows (the index λ is omitted for convenience in the following expressions) [22]

$$\begin{aligned} t_{\pi\gamma} &= \epsilon_\mu J^\mu \\ &= \mathcal{L} + i\vec{\sigma} \cdot \vec{K} \\ &= \sum_{n=0,1} (-i)^n \sqrt{2n+1} \left[\boldsymbol{\sigma}^{(n)} \otimes \mathbf{K}^{(n)} \right]^{(0)}, \end{aligned} \quad (44)$$

where $\vec{\sigma}$ denote the Pauli spin matrices with $\boldsymbol{\sigma}^{(0)} = 1$, \mathcal{L} and \vec{K} are functions of the invariant pion photoproduction amplitudes A_i ($i=1, 2, 3, 4$) with $\mathbf{K}^{(0)} = \mathcal{L}$. The elementary production amplitudes \mathcal{L} and \vec{K} are calculated from the non-relativistic reduction of the elementary operator [15, 39] and are given in Appendix B.

Since both initial and final states of the deuteron are unpolarized, the sums over the spin projections can be performed by means of

$$\sum_{m_d m'_d} \left| \mathcal{M}_{m_d m'_d} \right|^2 = \sum_{\Lambda, m_\Lambda} \left| \mathcal{M}_{m_\Lambda}^{(\Lambda)} \right|^2. \quad (45)$$

Then, using standard angular momentum algebra, the reaction amplitude (42) can be put into the following form

$$\begin{aligned} \mathcal{M}_{m_d m'_d}^{\text{IA}}(\vec{q}, \vec{k}) &= 2\sqrt{3} \sum_{\Lambda=0}^2 \sum_{M_\Lambda} (-1)^{M_\Lambda} \sqrt{2\Lambda+1} \\ &\times (1 m_d \Lambda - M_\Lambda | 1 m'_d) \\ &\times \sum_{LL'=0,2} \int \frac{d^3 p}{(2\pi)^3} \left[\begin{Bmatrix} L & 1 & 1 \\ 1 & L' & \Lambda \end{Bmatrix} \right] \\ &\times \{ Y^{[L]}(\hat{p}') \otimes Y^{[L]}(\hat{p}) \}_{M_\Lambda}^{[\Lambda]} \mathcal{L} \\ &- (-1)^\Lambda \sqrt{6} \sum_{\ell=0}^3 \sqrt{2\ell+1} \left\{ \begin{Bmatrix} \Lambda & 1 & 1 \\ 1 & 1 & 1 \\ \ell & L & L' \end{Bmatrix} \right\} \\ &\times \{ \{ Y^{[L']}(\hat{p}') \otimes Y^{[L]}(\hat{p}) \}^{[\ell]} \otimes K^{[1]} \}_{M_\Lambda}^{[\Lambda]} \\ &\times u_{L'}(\vec{p}') u_L(\vec{p}). \end{aligned} \quad (46)$$

As for the isospin structure, it is easy to understand that from all three amplitudes in the isospin decomposition of the elementary operator for pion photoproduction with Cartesian index $\alpha=1, 2, 3$ [40]

$$t_{\pi\gamma} = M^{(0)} \tau_\alpha + M^{(-)} \frac{1}{2} [\tau_\alpha, \tau_3] + M^{(+)} \delta_{\alpha 3}, \quad (47)$$

only $M^{(+)}$ can contribute to the coherent process from the deuteron.

In the present work, we use as realistic elementary pion production operator the MAID2007 model [30] which has been developed to analyze the world data for pion production off protons and neutrons. The MAID model is a unitary isobar model for a partial wave analysis, where all parameters are fitted to experimental observables as cross sections and polarization asymmetries from pion photo- and electroproduction in the energy range from pion threshold up to $W_{\gamma^* N} = 2$ GeV and photon virtualities $Q^2 < 5$ GeV². It is based on a non-resonant background described by Born terms and vector-meson exchange contributions in the t -channel and 13 four star nucleon resonance excitations in the s -channel below 2 GeV. This model uses effective Lagrangian methods to calculate the Born background, including ρ - and E_γ -meson exchange processes. The background amplitudes are unitarized with a $(1 + i f_{\ell\pm}^{\pi N})$ factor, where $f_{\ell\pm}^{\pi N}$ are the πN -scattering amplitudes. Moreover, the following four star nucleon resonances were included in the MAID2007 model: $P_{33}(1232)$, $P_{11}(1440)$, $D_{13}(1520)$, $S_{11}(1535)$, $S_{31}(1620)$, $S_{11}(1650)$, $D_{15}(1675)$, $F_{15}(1680)$, $D_{33}(1700)$, $P_{13}(1720)$, $F_{35}(1905)$, $P_{31}(1910)$, and $F_{37}(1950)$. These resonances are described by Breit-Wigner forms. The MAID2007 model is parameterized in terms of invariant amplitudes and allows for the evaluation in any frame of reference. Feynman diagrams of the MAID elementary amplitude of pion photoproduction on the nucleon are shown in Fig. 4.

2. The Rescattering Effects

In what follows, we describe the matrix elements for the calculation of the additional contributions of two-body process $\mathcal{M}_{m_d \lambda m'_d}^{\text{FOR}}$ (diagram (b) in Fig. 2) and the full ηNN three-body dynamics $\mathcal{M}_{m_d \lambda m'_d}^{\text{TBM}}$ (diagram (c) in Fig. 2). These two contributions are governed by various hadronic and electromagnetic two-body reactions included in our treatment of diagrams (b) and (c) in Fig. 2. Due to the strong coupling between the ηN and πN channels in the $S_{11}(1535)$ -resonance region, the transitions $\eta N \leftrightarrow \pi N$ must, in general, be taken into account. Therefore, in the present work, only the $S_{11}(1535)$ -resonance is taken into account in the calculation of the π - and η -exchange contributions and all contributions from other resonances are neglected. This neglect leads to an underestimation of the π -rescattering effect, but it should not strongly affect the quality of the

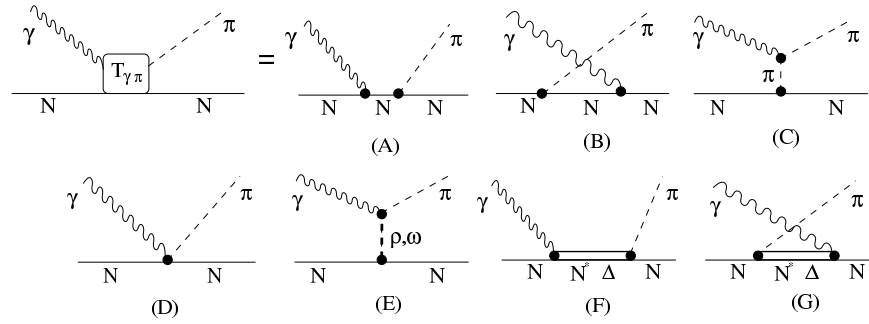


FIG. 4: Feynman diagrams for pion photoproduction from free nucleons. Born terms: (A) direct nucleon pole or s -channel, (B) crossed nucleon pole or u -channel, (C) pion in flight or t -channel, and (D) Kroll-Rudermann contact term; (E) vector-meson exchange; resonance excitations: (F) direct or s -channel and (G) crossed or u -channel.

results (see also Refs. [17, 22, 24, 25]). The reason for this stems from the fact that this effect does not contribute into the formation of the peak structure observed in the differential cross section at extremely backward pion angles around the production of η -threshold [3, 4]. In Ref. [12] where the pion-exchange mechanism was calculated more precisely the corresponding effect in the second resonance region is less than 20%. This means that the role of pion-exchange seems to be not very essential.

As already indicated in the caption of Fig. 2, the three-body problem for the intermediate $\eta N N$ system is solved only for the lowest s -wave three-body configuration 1S_0 ($J^\pi = 0^-, T = 1$). It is the state of lowest orbital angular momentum ($\ell = 0$) which is mostly distorted by the multiple scatterings between particles in the intermediate two-body systems and coupled with angular momentum $\ell = 0$ of the third particle with respect to the pair [41]. The remaining partial waves with higher orbital angular momentum can be included perturbatively up to the first order within the rescattering approximation (diagrams (a)+(b)). This approximation is well justified by the strong s -wave dominance in the intermediate two-body interactions. As was shown in Refs. [41, 42], it is the lowest s -wave three-body state, that is very sensitive to the higher-order scattering contributions. The higher partial waves are well approximated by the first-order rescattering terms.

For the elementary amplitudes appearing in diagrams (b) and (c) of Fig. 2, we assume that the π - and η -photoproduction reactions on the nucleons as well as their interactions with nucleons were assumed to proceed exclusively via the excitation of the $S_{11}(1535)$ -resonance. According to this assumption, the separable transition matrix $T_{\alpha N \rightarrow \beta N}$ ($\alpha, \beta \in \{\pi, \eta\}$) of meson-nucleon scattering is given by the conventional isobar model [43]

$$T_{\alpha N \rightarrow \beta N}(\vec{p}, \vec{p}'; W) = \frac{g_\alpha(\vec{p}) g_\beta(\vec{p}')}{W - M_0 - \Sigma_\eta(W) - \Sigma_\pi(W) - \Sigma_{\pi\pi}(W)}, \quad (48)$$

as a function of the invariant energy of the on-shell meson-nucleon scattering W , where $\alpha, \beta \in \{\pi, \eta\}$ and $\Sigma_\pi(W)$, $\Sigma_\eta(W)$, and $\Sigma_{\pi\pi}(W)$ denote the $S_{11}(1535)$ self

energy contributions from the πN , ηN , and $\pi\pi N$ channels, respectively. \vec{p} and \vec{p}' denote the relative on-shell momenta in the initial and final states of meson-nucleon scattering, respectively. The $T_{\alpha N \rightarrow \beta N}$ matrix is determined by the bare resonance mass $M_0 = 1598$ MeV and the parameters of the vertex functions $g_\alpha(\vec{p})$. For the latter, we take a simple Hulthén form

$$g_\alpha(\vec{p}) = g_\alpha \left(1 + \frac{p^2}{\Lambda_\alpha^2}\right)^{-1}, \quad (49)$$

containing the strength of the coupling g_α and the range of the Hulthén form factor Λ_α . As in Ref. [17], the scattering parameters $g_\pi = 2.51$, $g_\eta = 2.0$, $\Lambda_\pi = 404.5$ MeV, and $\Lambda_\eta = 694.6$ MeV are used. These parameters are adjusted to fit the ηN scattering length $a_{\eta N} = (0.5 + i0.3)$ fm and at the same time to provide a reasonably good description of the reactions $\gamma N \rightarrow \alpha N$ and $\pi^- p \rightarrow \eta n$ in the $S_{11}(1535)$ channel (see also Refs. [17, 44, 45]). This value of $a_{\eta N}$ is considered as an approximate average of the scattering lengths provided by modern ηN scattering analyses.

The contributions to the self energy from the various channels are expressed in terms of $g_\alpha(\vec{p})$ ($\alpha, \beta \in \{\pi, \eta\}$) as follows

$$\Sigma_\alpha(W) = \frac{1}{2\pi^2} \int_0^\infty \frac{q^2 dq}{2\omega_\alpha(q)} \frac{g_\alpha^2(q)}{W - E_N(q) - \omega_\alpha(q) + i\varepsilon}, \quad (50)$$

with E_N and ω_α denoting the on-shell energies of nucleon and meson, respectively. Since the double pion channel $\pi\pi N$ is not explicitly included in the present calculations, primarily because of its rather weak coupling to the $S_{11}(1535)$ -resonance, we parameterize, following [43], the corresponding self energy in a simplified manner as a pure imaginary contribution proportional to the three-particle phase space

$$\Sigma_{\pi\pi}(W) = -\frac{i}{2} \gamma_{\pi\pi} \frac{W - M_N - 2m_\pi}{m_\pi}, \quad (51)$$

with $\gamma_{\pi\pi} = 4.3$ MeV.

For the π^- - and η -photoproduction amplitudes on the nucleon, we take the same ansatz as in (48) where one hadronic vertex function is replaced by the electromagnetic vertex $g_{\gamma N}$ for $\gamma N \rightarrow S_{11}(1535)$ which depends only on the invariant energy of the on-shell $\gamma N \rightarrow \alpha N$ interaction $W_{\gamma N}$ and is parameterized in the form

$$g_{\gamma p}(W_{\gamma N}) = \begin{cases} \frac{e}{\sqrt{4\pi}} \sum_{n=0}^4 a_n \left(\frac{k}{m_\pi} \right)^n, & \text{for } W_{\gamma N} \geq M_N + m_\pi, \\ g_{\gamma p}(M_N + m_\pi), & \text{else,} \end{cases} \quad (52)$$

$$g_{\gamma n}(W_{\gamma N}) = -0.82 g_{\gamma p}(W_{\gamma N}),$$

where $a_0 = 0.5502$, $a_1 = -0.01923$, $a_2 = 0.1018$, $a_3 = 0.002255$, and $a_4 = -0.007042$ [17]. The pion c.m. momentum corresponding to the total invariant energy $W_{\gamma N}$ is given by

$$k = \frac{\sqrt{[W_{\gamma N}^2 - (M_N + m_\pi)^2][W_{\gamma N}^2 - (M_N - m_\pi)^2]}}{2W_{\gamma N}}. \quad (53)$$

The isospin dependence of the $S_{11}(1535)$ photo-excitation amplitude is taken in this work according to the approximate quantity [46]

$$\frac{\sigma(\gamma p \rightarrow \eta p)}{\sigma(\gamma n \rightarrow \eta n)} \approx 0.67. \quad (54)$$

As mentioned above, the parameters, appear in the expressions (48) through (52), are chosen in such a way that, the reactions $\gamma N \rightarrow \alpha N$ ($\alpha \in \{\pi, \eta\}$) and $\pi^- p \rightarrow \eta n$ are well reproduced in the $S_{11}(1535)$ channel (see also Refs. [44, 45]). Also, the chosen parameter set predicts the value $a_{\eta N} = (0.5 + i0.3)$ fm for the ηN scattering length which has been considered in Ref. [17] as an approximate average of the various values provided by the ηN analyses.

For the numerical solution of the three-body problem for the intermediate ηNN interaction we use the method described in Ref. [41]. For completeness, details of the essential ingredients of the formalism for this method are given in Appendix C. Here, we only would like to mention that the key point of the method is the separable representation of the driving two-body interaction in the πN , ηN , and NN subsystems. The corresponding $T_{\alpha N \rightarrow \beta N}$ ($\alpha, \beta \in \{\pi, \eta\}$) matrix for meson-nucleon multiple channel scattering is given by the isobar formula (48), which is driven exclusively by the dominant $S_{11}(1535)$ resonance. For the NN interaction, we use the separable representation of the Bonn potential as given in Ref. [47] for the 1S_0 and 3S_1 configurations.

As is well known, the separable ansatz makes it possible to reformulate the three-body problem in terms of two-body scattering between quasiparticles without loss

of essential physics. As a consequence, the solution of the problem is given by an amplitude $T_{S_{11}}$ of the effective transition $\gamma d \rightarrow NS_{11}$ as presented in Fig. 3. The needed physical amplitude $\gamma d \rightarrow \pi^0 d$ is then obtained through an additional loop integration (diagram (c) in Fig. 2).

III. RESULTS AND DISCUSSION

Now, we will discuss our results for coherent photoproduction of π^0 -meson from the deuteron near the η -production threshold. In particular, we concentrate our discussion on results at backward pion angles, where a cusp-like structure in the energy dependence of the differential cross section has been observed at extreme backward direction [3, 4]. Our calculations are based on a theoretical approach which includes the amplitudes of the pure IA, two-step process with intermediate πN - and ηN -rescatterings, and the higher order terms in the multiple scattering series for the intermediate ηNN three-body interaction. We would like to mention that possible recoil polarization of the final deuteron is neglected.

The pion photoproduction amplitude is evaluated by taking a realistic NN potential model for the deuteron wave functions. In our calculation, the wave function of the CD-Bonn potential model [38] has been used. For the elementary pion photoproduction operator, the extended version of the unitary isobar MAID2007 model [30] has been considered. For the various hadronic and electromagnetic two-body reactions included in our treatment of the rescattering diagrams, only the $S_{11}(1535)$ resonance was taken into account. In addition, the photoproduction of π^- and η -mesons on the nucleon as well as their interactions with nucleons were assumed to be proceed exclusively via the extraction of the $S_{11}(1535)$ resonance. The intermediate ηNN three-body problem has been solved by using separable representation of the driving two-body interaction in the πN , ηN , and NN subsystems. The corresponding amplitudes for πN and ηN scattering are given by the isobar formula (48). For the NN subsystem, the separable representation of the Bonn potential [47] for the 1S_0 and 3S_1 channels has been used.

A. Differential and Total Cross Sections

We start the discussion with the results for differential and total cross sections for coherent π^0 -photoproduction from the deuteron near η -threshold as plotted in Figs. 5 and 6 in the pure IA and with rescattering effects [24].

The calculated differential cross section at several fixed values of $\cos \theta$ in the γd c.m. frame is plotted in Fig. 5 as a function of photon lab-energy (the experimental CLAS data [3, 4] are at the same values of $\cos \theta$). It is clear that the contribution from IA amplitude (dotted curve) dominates the differential cross section for $\cos \theta = 0$. The rela-

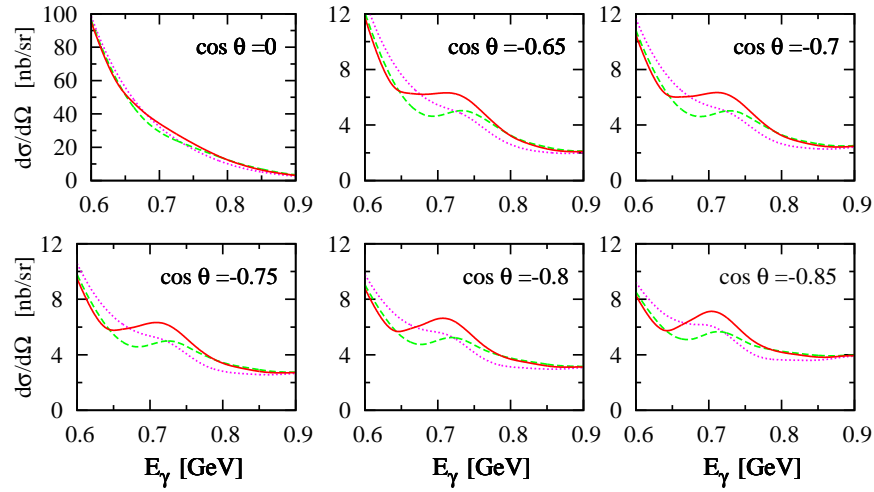


FIG. 5: (Color online) The differential cross section of $\gamma d \rightarrow \pi^0 d$ versus photon lab-energy at various values of $\cos \theta$ in the γd c.m. frame using MAID2007 [30] for the elementary amplitude and CD-Bonn potential [38] for the deuteron wave function. Curve conventions: dotted, IA; dashed, IA+FOR; solid, IA+FOR+TBM.

tive contribution from other amplitudes increases as $\cos \theta$ approaches -0.85 . This means that the differential cross section shows at forward direction very little influence of the two-step processes and all terms in the multiple scattering series within a three-body model. With increasing pion angles, a noticeable contribution from the two-step processes and intermediate ηNN three-body interaction is obtained in the photon lab-energy range from $E_\gamma \simeq 600$ to 800 MeV. It becomes maximum at extremely backward pion angles. This maximum is getting more pronounced at $\cos \theta \rightarrow -0.85$.

Figure 5 demonstrates the peak observed in the energy dependence of the differential cross section at extremely backward pion angles and photon lab-energy slightly above 700 MeV [3, 4]. As was mentioned in Ref. [16], the main origin of this effect is the presence of the $S_{11}(1535)$ -resonance in the diagram with ηN -rescattering. In addition, the contribution from intermediate ηNN three-body interaction make also a slight contribution to the formation of the bump structure. Our present results confirm these statements. When the full dynamics in the intermediate ηNN system is included (solid curve in Fig. 5), a much more prominent peak structure is observed at photon lab-energy slightly above 700 MeV. This structure accompanied by a slight shift towards lower energies. Therefore, the difference between the solid and dashed curves in Fig. 5 demonstrates the importance of the higher order contributions in the multiple scattering series for the intermediate ηNN interaction. This means, in particular, that the physics behind the cusp structure observed in the differential cross section for coherent π^0 -photoproduction from the deuteron [3, 4] near η -threshold at backward direction may be complicated than was discussed in Ref. [16]. We would like to point out that the cusp structure caused by the opening of the ηN channel is strongly smeared by the Fermi motion effect and can hardly be visible in the reaction on a

deuteron. The structure which we see at backward angles in Fig. 5 is nothing but a consequence of interference between IA and rescattering contributions in Eq. (39).

In comparison with the calculation of Ref. [17], we can only compare with results at $\cos \theta = 0$ and -0.85 , where differences are found. These differences seem likely to be due to the fact that the author of Ref. [17] used the MAID2003 model [29] for the elementary $\gamma N \rightarrow \pi^0 N$ amplitude and the Bonn potential (OBEPQ version) [48] for the deuteron wave function, while in the present work we used the extended version MAID2007 model [30] for the former and the CD-Bonn potential [38] for the latter. We will return to this point in subsection III L, where we found that the computations with different elementary amplitudes are quite different.

We show in the left panel of Fig. 6 the results for total cross section as a function of photon lab-energy near η -threshold using the MAID2007 model [30] for the elementary amplitude and the CD-Bonn potential [38] for the deuteron wave function. A comparison of the dotted to the solid curves demonstrates the effect of the modified three-body calculation. It is clear that the curves are almost coincide. One notes in general a weak influence from the rescattering effects which is not the case for differential cross section. These effects become a few percent in the minimum and in the peak position, where a slight enhancement in the maximum is found. It reduces the total cross section by a few percent at $E_\gamma \simeq 630$ MeV and shifts its maximum towards a slightly higher position at $E_\gamma \simeq 750$ MeV. In order to give a more detailed and the relative size of rescattering effects, we have plotted in the right panel of Fig. 6 the relative deviations $\sigma_{IA+FOR}^{\text{tot}}/\sigma_{IA}^{\text{tot}}$ (dashed curve) and $\sigma_{IA+FOR+TBM}^{\text{tot}}/\sigma_{IA}^{\text{tot}}$ (solid curve) as functions of photon lab-energy. One notes in general a weak influence from the rescattering effects.

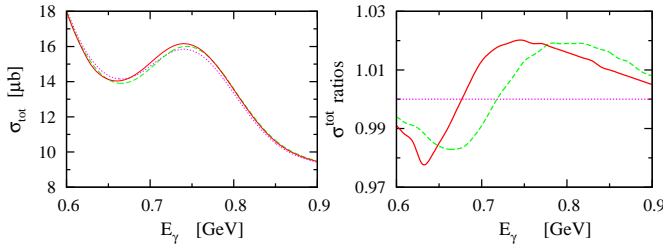


FIG. 6: (Color online) Left panel: Total $\gamma d \rightarrow \pi^0 d$ cross section as a function of photon lab-energy using MAID2007 [30] for the elementary amplitude and CD-Bonn potential [38] for the deuteron wave function. Curve conventions as in Fig. 5. Right panel: The relative deviations $\sigma_{IA+FOR}^{\text{tot}}/\sigma_{IA}^{\text{tot}}$ (green dashed) and $\sigma_{IA+FOR+TBM}^{\text{tot}}/\sigma_{IA}^{\text{tot}}$ (red solid) as functions of E_γ .

B. Beam Asymmetry for Linearly Polarized Photons

As next, we discuss the results for the photon asymmetry Σ for linearly polarized photons and unpolarized deuterons of the $\vec{\gamma}d \rightarrow \pi^0 d$ reaction [22]. For an unpolarized deuteron, i.e. $P_1^d = P_2^d = 0$, and photons linearly perpendicular and parallel to the reaction plane, the corresponding cross sections are

$$\frac{d\sigma_\perp}{d\Omega} = \frac{d\sigma_0}{d\Omega} [1 - P_l^\gamma \Sigma(\theta)] \quad \text{for } \phi = \frac{\pi}{2}, \quad (55)$$

$$\frac{d\sigma_\parallel}{d\Omega} = \frac{d\sigma_0}{d\Omega} [1 + P_l^\gamma \Sigma(\theta)] \quad \text{for } \phi = 0. \quad (56)$$

Thus measuring the cross sections for parallel and perpendicular linear polarization allows one to determine the photon asymmetry

$$\Sigma(\theta) = \frac{1}{P_l^\gamma} \frac{d\sigma_\parallel - d\sigma_\perp}{d\sigma_\parallel + d\sigma_\perp}. \quad (57)$$

Figure 7 illustrates the energy dependence for the linear photon asymmetry calculated at fixed values of $\cos\theta$ in the γd c.m. frame in IA (dotted curves), IA+FOR (dashed curves), and IA+FOR+TBM (solid curves). In general, we see that the photon asymmetry has positive values. It is quite large at $\cos\theta=0$ and decreases with increasing pion angle. At backward direction, one notes a different behavior of the photon asymmetry. The deep minimum at $E_\gamma \simeq 630$ MeV is not obvious at $\cos\theta=0$. The beam asymmetry Σ exhibits quite a broad structure at $E_\gamma \simeq 700$ MeV for extreme backward direction which is not the case at $\cos\theta=0$.

The inclusion of FOR decreases the photon asymmetry Σ when the photon lab-energy changes from $E_\gamma \simeq 580$ to 730 MeV. At higher energies, one notes that the inclusion of FOR increases the photon asymmetry in comparison to the IA values. At backward direction, it is obvious that Σ exhibits a maximum at $E_\gamma \simeq 650$ MeV when only the IA prediction is considered. When the FOR

contribution is switched on, this maximum is shifted towards higher energies. When the full rescattering terms are taken into account, this maximum is shifted towards lower energies with larger values of photon asymmetry. One notes also that the Σ -asymmetry decreases with increasing pion angle until it reaches zero at $\theta = \pi$. Clearly, the influence of FOR and TBM contributions is noticeable even at $\cos\theta=0$. This means that the Σ -asymmetry is quite sensitive to the interference of rescattering effects.

C. Target Asymmetries for Polarized Deuterons

By proper choices of the deuteron orientation axis one can extract the target asymmetries T_{IM} for unpolarized photons. Figure 8 provides an overview over the vector (T_{11}) and the tensor (T_{20} , T_{21} , T_{22}) target asymmetries for $\vec{\gamma}d \rightarrow \pi^0 d$ as functions of photon lab-energy at various values of $\cos\theta$ [22]. In general, one notes strong sensitivity to the rescattering effects at backward direction and also at $\cos\theta=0$. The vector target asymmetry T_{11} is positive at $\cos\theta=0$, but it has negative values at extreme backward direction. It is sensitive to the imaginary parts of the scattering amplitudes and shows a broad energy dependence over the whole angular range. The structure of T_{11} changes significantly with pion angle. While at $\cos\theta=0$ one finds a maximum around 620 MeV, one notes a backward negative minimum around 650 MeV. The results of T_{11} indicate that the influence of intermediate ηNN three-body calculation is important at backward direction, specially for photon energies close to the η -threshold. One notices also that the T_{11} -asymmetry decreases with increasing pion angle. It becomes zero at $\theta = \pi$.

The tensor target asymmetries of the reaction $\vec{\gamma}d \rightarrow \pi^0 d$ are much more sensitive to the rescattering effects (see also Ref. [20] where only the first-order rescattering was considered). This is apparent in the T_{20} , T_{21} , and T_{22} asymmetries for tensor polarized deuterons and unpolarized photons as shown in Fig. 8. The T_{20} -asymmetry has negative values. It exhibits at backward direction a rapid increase with increasing photon energy. We found that T_{20} is very sensitive to the rescattering contributions. In the region of $620 \text{ MeV} < E_\gamma < 800 \text{ MeV}$, the contribution of TBM is more important even at $\cos\theta=0$. The contribution of FOR dominates at photon energies greater than 800 MeV at extreme backward direction. The results of T_{21} and T_{22} asymmetries are also sensitive to the rescattering effects at backward direction. The difference between the dotted (IA) and the solid (IA+FOR+TBM) curves in Fig. 8 is noticeable at $E_\gamma > 600$ MeV and backward direction. This difference is small at $\cos\theta=0$ in the case of T_{21} -asymmetry. At backward direction, the T_{21} -asymmetry shows an oscillatory behavior and a drastic influence of rescattering effects when the full rescattering terms are switched on. T_{21} exhibits a sharp peak at $E_\gamma \simeq 650$ MeV and clearly differs in size between IA and IA+FOR+TBM, being even opposite in phase

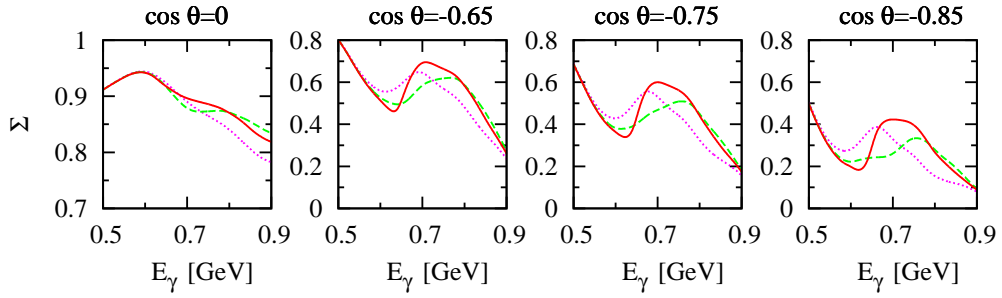


FIG. 7: (Color online) Same as in Fig. 5 but for the beam asymmetry Σ for linearly polarized photons of $\vec{\gamma}d \rightarrow \pi^0 d$.

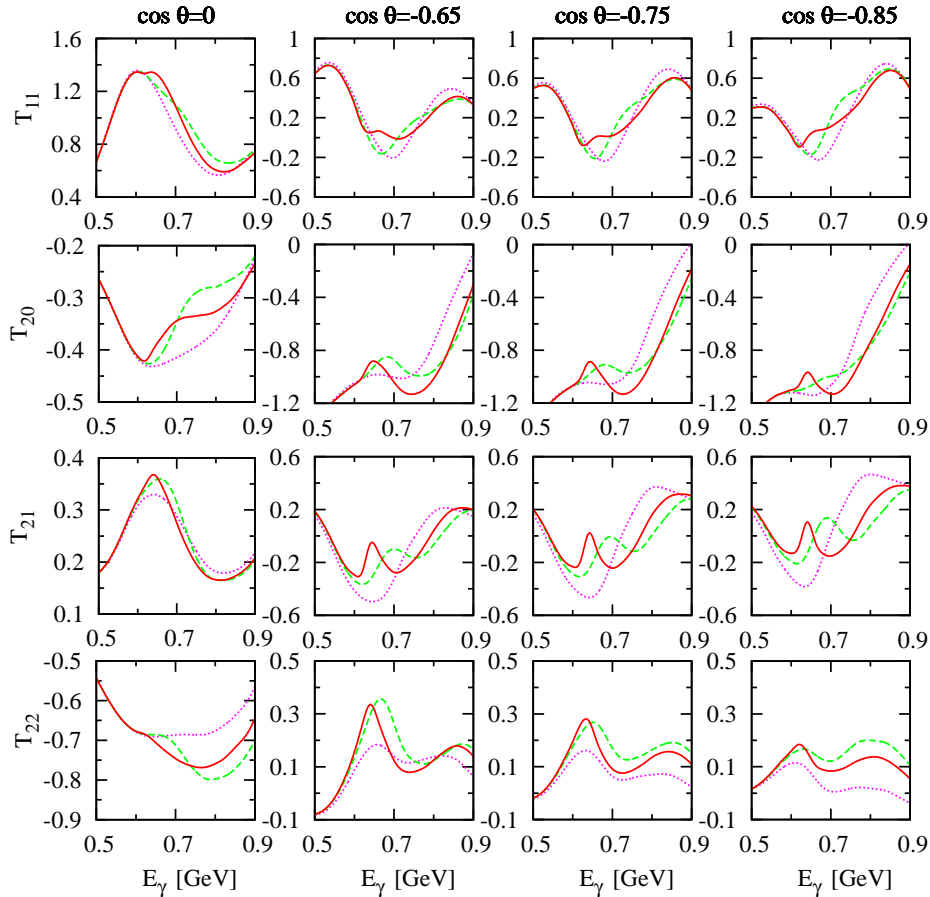


FIG. 8: (Color online) Same as in Fig. 5 but for the target asymmetries T_{11} , T_{20} , T_{21} , and T_{22} of $\vec{\gamma}d \rightarrow \pi^0 d$.

around photon energies of 650 MeV. The T_{22} -asymmetry has negative values at $\cos\theta=0$ and a noticeable contribution from the rescattering effects is noted. At backward direction, the T_{22} -asymmetry exhibits a peak near $E_\gamma=650$ MeV that becomes broader with increasing pion angle. The top of this peak decreases with increasing pion angle. We want to remind that the T_{21} and T_{22} asymmetries are equal zero at $\theta = \pi$.

We find that the single-spin asymmetries for the $\vec{\gamma}d \rightarrow \pi^0 d$ reaction are sensitive to the contribution of intermediate ηNN three-body interaction.

D. Beam-Target Asymmetries for Circularly Polarized Photons and Polarized Deuterons

Next we discuss the beam-target double spin asymmetries for circularly polarized photons and polarized deuterons [22]. We display in Fig. 9 the asymmetries T_{10}^c and T_{11}^c for circularly polarized photons and vector polarized deuterons and in Fig. 10 the asymmetries T_{21}^c and T_{22}^c for circularly polarized photons and tensor polarized deuterons. We note that all of these asymmetries are non-vanishing. An exception are the asymmetries T_{11}^c , T_{21}^c , and T_{22}^c which equal zero at $\theta = \pi$. As al-

ready mentioned in section II, the T_{20}^c -asymmetry vanish identically.

The vector asymmetry T_{10}^c is quite sizeable in the backward direction and also at $\cos\theta=0$. We want to remind that this beam-target double spin asymmetry determines the GDH sum rule [37]. We found that the influence of rescattering effects is important, in particular at backward direction. One can also see that the energy dependence is strong. When the rescattering effects are switched on, one sees for $\theta=90^\circ$ that the T_{10}^c -asymmetry has a peak at $E_\gamma \simeq 650$ MeV. The results of T_{10}^c is then rapidly falloff to negative values. At backward direction, we note that T_{10}^c has a negative minimum around $E_\gamma=650$ MeV. It is also clear that T_{10}^c is quite sensitive to the interference of rescattering contributions. The other vector asymmetry, T_{11}^c , shows a rather different behavior. The influence of rescattering effects is sizeable at photon energies greater than 650 MeV. T_{11}^c decreases with increasing photon energy until it reaches a minimum value and then increases again. This minimum value shifts toward lower energies with increasing pion angle. The T_{11}^c -asymmetry is considerably larger at backward direction, but it is a little less sensitive to the rescattering effects in comparison to the T_{10}^c asymmetry, specially at backward direction. The role of rescattering effects becomes important in the energy range of $E_\gamma=650$ –800 MeV.

The tensor asymmetries T_{21}^c and T_{22}^c (Fig. 10) are more sensitive to the rescattering effects. This is particularly apparent at backward direction. The T_{21}^c -asymmetry shows that the pure IA is dominant at photon energies less than 630 MeV. When $\cos\theta=0$, we see that T_{21}^c increases with increasing photon energy until $E_\gamma \simeq 600$ MeV and then rapidly decreases to negative values. On the contrary, it decreases at backward direction until it reaches a minimum value at about 630 MeV and then rapidly increases with increasing photon energy until a broad maximum is reached and then slowly decreases. The T_{22}^c -asymmetry has a similar behavior. However, rescattering effects are much larger in this case at backward direction. When $\theta=90^\circ$, the inclusion of rescattering effects decreases the T_{22}^c -asymmetry for $E_\gamma > 650$ MeV. At backward direction, one sees that the inclusion of rescattering contributions increases the T_{22}^c -asymmetry. We observe also that the inclusion of FOR alone would lead to quite different results for T_{21}^c and T_{22}^c -asymmetries as can be seen from Fig. 10. When the full rescattering terms are considered, one notes that T_{22}^c decreases with increasing photon energy until a minimum value at about 600 MeV is reached. With increasing photon energy, T_{22}^c increases until a maximum value at about 650 MeV is obtained and then decreases again. A peak at extreme backward direction is obvious for $E_\gamma \simeq 650$ MeV. When only the FOR effect is considered, one sees a second peak at about 800 MeV. This peak is not clearly obvious when in addition the TBM contribution is taken into account, because the T_{22}^c asymmetry has large negative value of IA at this value of energy.

E. Beam-Target Asymmetries for Linearly Polarized Photons and Polarized Deuterons

We now turn to the beam-target double spin asymmetries for linearly polarized photons and polarized deuterons [22]. The vector asymmetries T_{10}^l and $T_{1\pm 1}^l$ are shown in Fig. 11, while the tensor asymmetries T_{20}^l , $T_{2\pm 1}^l$, and $T_{2\pm 2}^l$ are displayed in Fig. 12. A quick glance reveals that the different contributions from rescattering terms manifest themselves in quite different ways in the various asymmetries. We note that all of these asymmetries are quite sizable in the backward direction and at $\cos\theta=0$. They are also sensitive to the rescattering effects. The influence of the rescattering mechanism can be seen by comparing the pure IA (dotted curves) with the full calculations (solid curves). Its contribution is biggest in the $E_\gamma=600$ –800 MeV region. Here, we want also to remind that the T_{10}^l , $T_{1\pm 1}^l$, T_{20}^l , and $T_{2\pm 1}^l$ asymmetries vanish identically at $\theta = \pi$.

At $\cos\theta=0$, one notes for the T_{10}^l and $T_{1\pm 1}^l$ asymmetries that the IA contribution is dominant in the energy region until 620 MeV. At higher energies, the rescattering effects contribute and a small cancellation between FOR and TBM is seen. Indeed, the rescattering effects are important in T_{11}^l , but much less important in T_{10}^l and T_{1-1}^l asymmetries. At backward direction, one notes also a small cancellation between FOR and TBM in $T_{1\pm 1}^l$ asymmetries, which is not the case for T_{10}^l . In addition, one sees that the asymmetry T_{10}^l differs in size between IA and IA+rescattering, being opposite in phase around 650 MeV. It shows enhanced sensitivity to TBM. The influence of rescattering effects increases significantly when going from $T_{1\pm 1}^l$ to T_{10}^l . We found that the interference between IA and rescattering terms in T_{11}^l is strongly angle dependent. It is also obvious that the T_{2-2}^l asymmetry becomes quite smaller at photon energies greater than 600 MeV if the TBM is included. At smaller energies, the TBM contribution is negligible.

Of the corresponding tensor asymmetries in Fig. 12, T_{20}^l is the largest. At $\cos\theta=0$, the effect of FOR and TBM is small. An exception is the T_{20}^l asymmetry where a notable effect is seen at photon energies greater than 600 MeV. At backward direction, one observes some of the rescattering effects in $T_{2\pm 1}^l$, whereas quite drastic influences of the rescattering effects can be seen in T_{20}^l and $T_{2\pm 2}^l$ asymmetries. It is obvious that $T_{2\pm 2}^l$ asymmetries show enhanced sensitivity to the contribution of TBM at energies greater than 650 MeV. As one notices, the interference between IA and IA+FOR+TBM in T_{2-2}^l is strongly dependent on photon energy and pion angle. This asymmetry has small positive values at extreme backward direction, but not vanish identically at $\theta = \pi$.

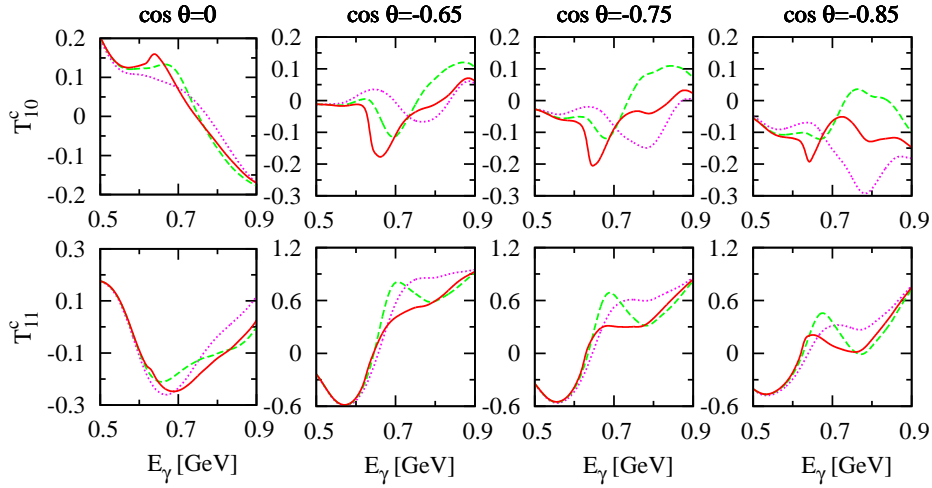


FIG. 9: (Color online) Same as in Fig. 5 but for the beam-target spin asymmetries T_{10}^c and T_{11}^c for circularly polarized photons and vector polarized deuterons of $\tilde{\gamma}d \rightarrow \pi^0 d$.

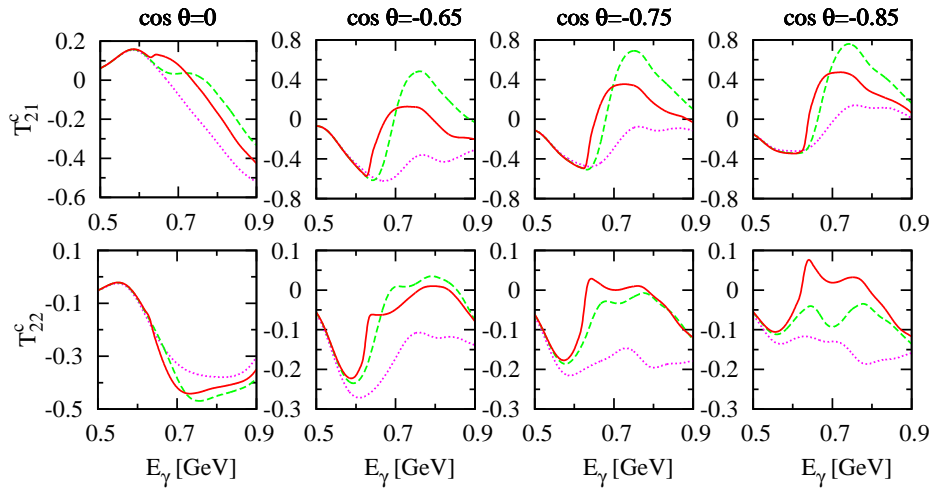


FIG. 10: (Color online) Same as in Fig. 5 but for the beam-target spin asymmetries T_{21}^c and T_{22}^c for circularly polarized photons and tensor polarized deuterons of $\tilde{\gamma}d \rightarrow \pi^0 d$.

F. Spin Asymmetries of the Total Cross Section

The spin asymmetries of the total cross section $\sigma_0 \tilde{T}_{20}$, $\sigma_0 \tilde{T}_{10}^c$, and $\sigma_0 \tilde{T}_{22}^l$ are shown in Fig. 13 as functions of photon lab-energy [22]. The left panel displays the asymmetry $\sigma_0 \tilde{T}_{20}$ for tensor polarized deuterons and unpolarized photons, the middle panel presents $\sigma_0 \tilde{T}_{10}^c$ for circularly polarized photons and vector polarized deuterons, and the right panel illustrates the $\sigma_0 \tilde{T}_{22}^l$ asymmetry for linearly polarized photons and tensor polarized deuterons. We found that the asymmetries $\sigma_0 \tilde{T}_{20}$ and $\sigma_0 \tilde{T}_{10}^c$ have negative values, whereas the $\sigma_0 \tilde{T}_{22}^l$ asymmetry has positive ones. A comparison of the dotted (IA) to the solid (IA+FOR+TBM) curves demonstrates the effect of the complete three-body calculation. It is clear that the three curves are almost coincide. As in the case of unpolarized total cross section (Fig. 6), one notes that

the influence of rescattering effects is quite marginal although not negligible. These effects become a few percent in the minimum and in the peak position.

G. Helicity-Dependent Cross Sections

Now, we start the discussion of the results for the doubly polarized differential and total cross sections for parallel and antiparallel spins of photon and deuteron as shown in Figs. 14 through 17 [25]. Special emphasize is given to their dependence on the complete intermediate ηNN three-body calculation.

Fig. 14 shows the helicity dependent differential cross section $d\sigma^P/d\Omega$ for parallel spins of photon and deuteron as a function of photon lab-energy at different values of $\cos\theta$ in the γd c.m. frame. The dotted, dashed,

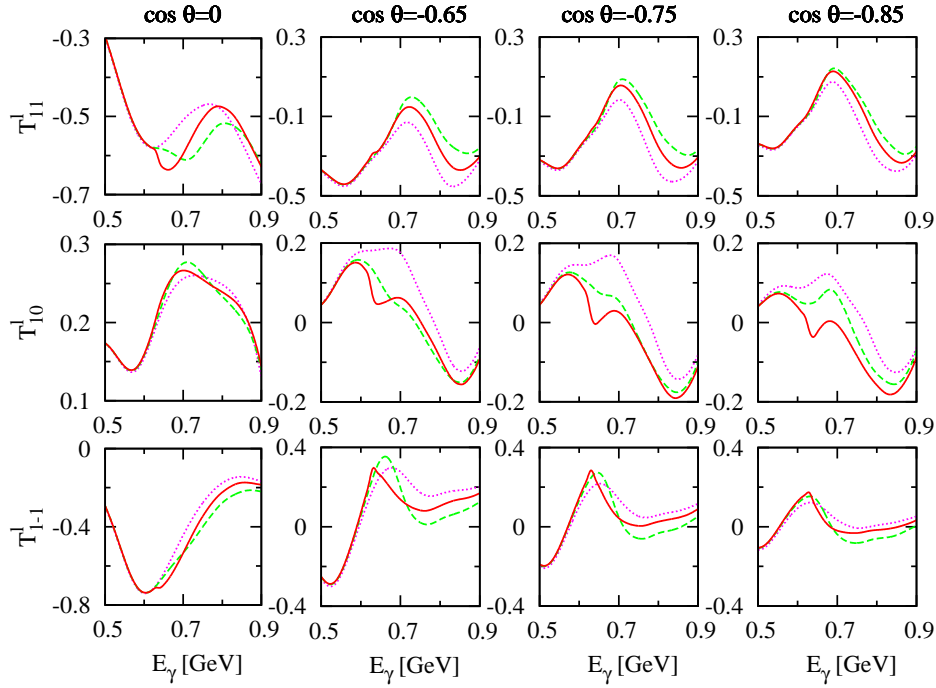


FIG. 11: (Color online) Same as in Fig. 5 but for the beam-target spin asymmetries T_{10}^l and $T_{1\pm 1}^l$ for linearly polarized photons and vector polarized deuterons of $\vec{\gamma}d \rightarrow \pi^0 d$.

and solid curves show the results of IA, IA+FOR, and IA+FOR+TBM, respectively. In general, it is obvious that $d\sigma^P/d\Omega$ rapidly decreases with increasing pion angle. Also, increasing pion angle from $\cos\theta = -0.65$ to -0.85 at $E_\gamma = 500$ MeV leads to a decrease in $d\sigma^P/d\Omega$ from 4.5 nb/sr to 0.5 nb/sr. At $\cos\theta = 0$, one sees that the results exponentially decrease with increasing photon energy. The effect of FOR and TBM is rather small in this case and the main contribution comes from the IA term. Rescattering effects appear mainly at extreme backward direction, where one observes a large cancellation between FOR and TBM contributions which becomes strong with increasing photon energy. The inclusion of these effects reduces the values of $d\sigma^P/d\Omega$. An exception of this reduction occurs at $\cos\theta = -0.85$, where the IA value is found to be smaller than the IA+FOR+TBM one in the photon energy range $E_\gamma \simeq 670-750$ MeV. It is also clear from Fig. 14 that the inclusion of FOR alone leads to quite different results.

Apparently, our calculation with complete rescattering effects exhibits a broad maximum at extreme backward direction when the photon energy changes from $E_\gamma = 700$ to 800 MeV. This phenomena takes place because η -production in hadron-hadron collision near the threshold is enhanced, because the cross section for excitation of the nearby baryonic resonance $S_{11}(1535)$ is large and this resonance is strongly coupled to the ηN channel.

In Fig. 15 we present our results for the differential polarized cross section $d\sigma^A/d\Omega$ for antiparallel spins of photon and deuteron as a function of photon energy at different values of $\cos\theta$. As in the case of $d\sigma^P/d\Omega$, we see

here that $d\sigma^A/d\Omega$ rapidly decreases with increasing pion angle. It begins with 200 nb/sr at $E_\gamma = 500$ MeV and $\cos\theta = 0$, while it decreases to 4 nb/sr at $\cos\theta = -0.85$ and the same energy. At $\cos\theta = 0$, one sees that the three curves of different contributions to the scattering amplitude almost coincide. This would imply that the rescattering effects be very small. But, if one goes to extreme backward pion angles, the rescattering effects seem to be substantially large. These effects are biggest in the $E_\gamma = 600-800$ MeV region and extreme backward direction. The FOR contribution leads to a strong reduction of $d\sigma^A/d\Omega$ in this energy region and a broad minimum is seen at about $E_\gamma = 670$ MeV, The inclusion of TBM shifts this minimum towards lower energies with larger values of $d\sigma^A/d\Omega$.

Fig. 16 displays the helicity dependent differential cross section difference $d(\sigma^P - \sigma^A)/d\Omega$ for parallel and antiparallel spins of photon and deuteron. Here, we see that the interference between IA and rescattering contributions is strongly angle dependent, leading to an obvious decrease in $d(\sigma^P - \sigma^A)/d\Omega$ at extreme backward angles. It is seen in Fig. 16 that the dependence of $d(\sigma^P - \sigma^A)/d\Omega$ on rescattering effects is small at energies less than $E_\gamma = 600$ MeV, but it becomes visible at higher energies and extreme backward angles. An exception is the result at $\cos\theta = 0$ where one finds a very small contribution from rescattering effects. At extreme backward direction, one observes a very strong cancellation between FOR and TBM contributions which becomes stronger in the photon energy range $E_\gamma = 650-800$ MeV. Thus, the inclusion of both FOR and TBM is seen

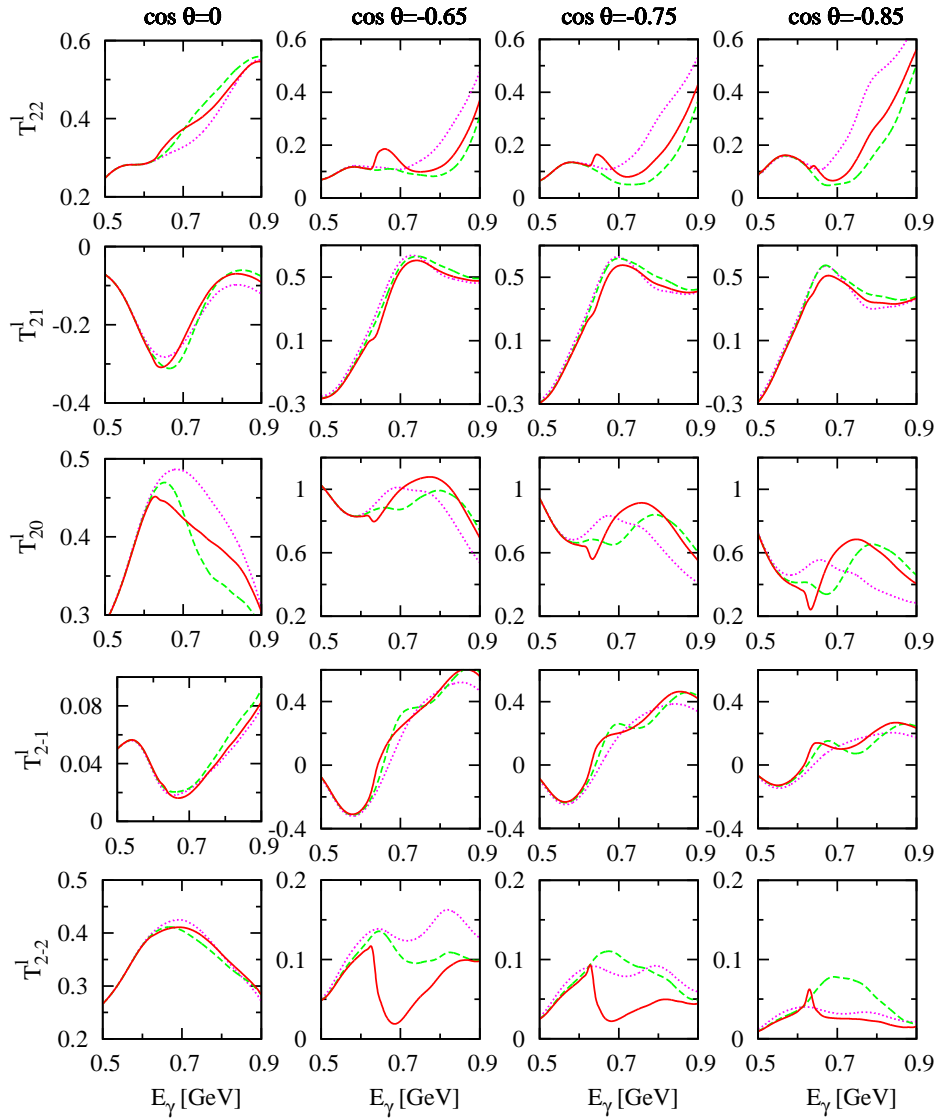


FIG. 12: (Color online) Same as in Fig. 5 but for the beam-target spin asymmetries T_{20}^l , $T_{2\pm 1}^l$, and $T_{2\pm 2}^l$ for linearly polarized photons and tensor polarized deuterons of $\vec{\gamma}\vec{d} \rightarrow \pi^0 d$.

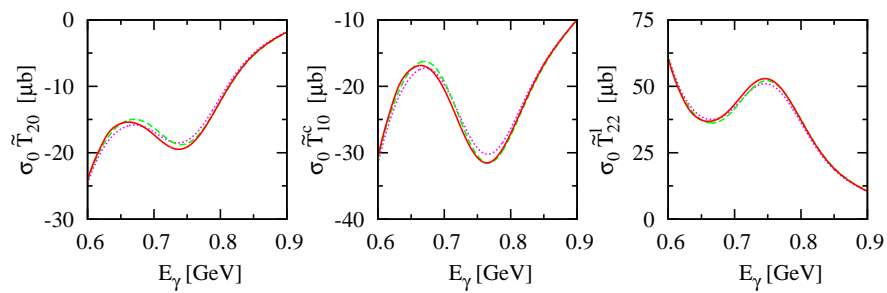


FIG. 13: (Color online) Same as in Fig. 5 but for the spin asymmetries $\sigma_0 \tilde{T}_{20}^l$, $\sigma_0 \tilde{T}_{10}^c$, and $\sigma_0 \tilde{T}_{22}^l$ of the total cross section.

very important in this energy range. The negative values in $d(\sigma^P - \sigma^A)/d\Omega$ at backward direction are due to large positive values in $d\sigma^A/d\Omega$.

An integration of $d\sigma^P/d\Omega$, $d\sigma^A/d\Omega$, and $d(\sigma^P -$

$\sigma^A)/d\Omega$ over the solid angle $d\Omega$ gives σ^P , σ^A and their difference $\sigma^P - \sigma^A$ of the doubly polarized total cross sections which are presented in Fig. 17. The upper part shows the total photo-absorption cross sections σ^P for

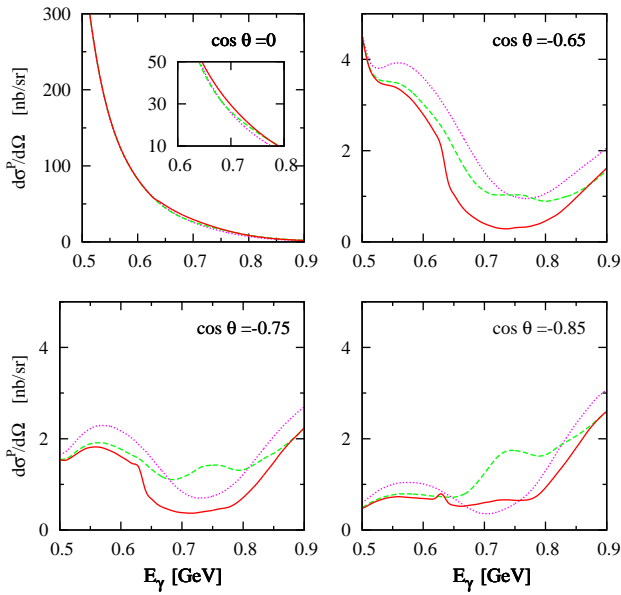


FIG. 14: (Color online) Same as in Fig. 5 but for the differential polarized cross section $d\sigma^P/d\Omega$ for parallel spins of photon and deuteron. The insert at $\cos\theta = 0$ shows the results on a larger scale.

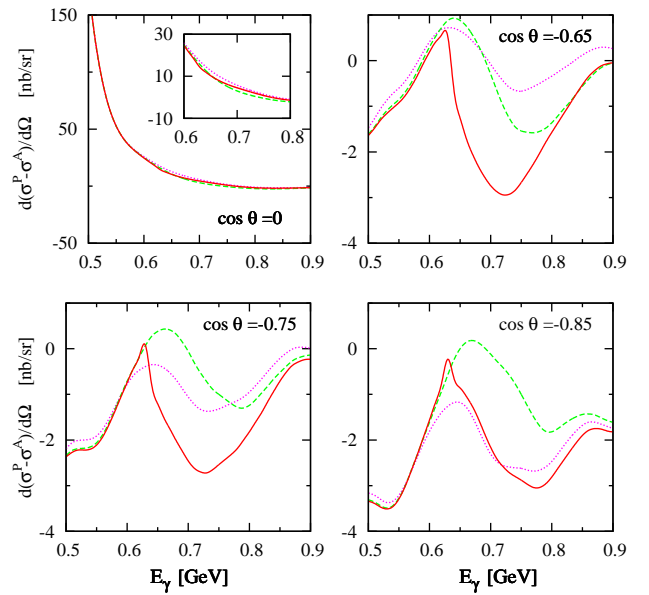


FIG. 16: (Color online) Same as in Fig. 5 but for the differential polarized cross section difference $d(\sigma^P - \sigma^A)/d\Omega$ for parallel and antiparallel spins of photon and deuteron. The insert at $\cos\theta = 0$ shows the results on a larger scale.

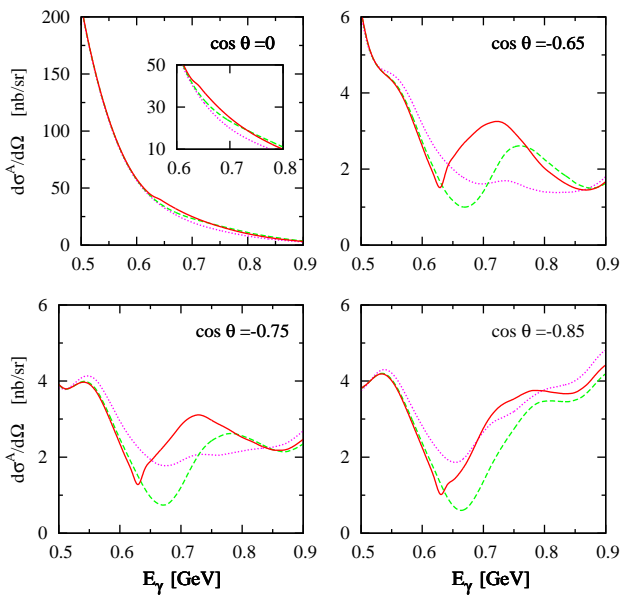


FIG. 15: (Color online) Same as in Fig. 5 but for the differential polarized cross section $d\sigma^A/d\Omega$ for antiparallel spins of photon and deuteron. The insert at $\cos\theta = 0$ shows the results on a larger scale.

circularly polarized photons on a target with spin parallel to the photon spin (left panel), the middle panel σ^A , the one for antiparallel spins of photon and target, and the right panel the spin asymmetry $\sigma^P - \sigma^A$. The lower part in Fig. 17 shows the corresponding ratios to the total photo-absorption cross sections and their difference with respect to the IA value. In contrast to the dou-

bly polarized differential cross sections, one notes here that the doubly polarized total cross sections and their difference are much less affected by rescattering effects. In fact, the dotted, dashed, and solid curves, representing the influence of IA, IA+FOR, and IA+FOR+TBM, respectively, appear almost indistinguishable. It is also obvious that σ^A is much larger than σ^P and, therefore, the spin asymmetry $\sigma^P - \sigma^A$ has negative values. The lower part in Fig. 17 shows in general a weak influence of rescattering effects.

H. The Helicity E -Asymmetry

In this subsection, we discuss the helicity E -asymmetry of the reaction $\vec{\gamma}d \rightarrow \pi^0 d$ near the η -threshold [25]. The helicity dependent photo-absorption cross sections for parallel and antiparallel spins of photon and deuteron are well suited to verify the GDH sum rule [37] and give contributions to the helicity E -asymmetry. This helicity asymmetry appears as an interference between the amplitudes with different parity-exchange properties.

The helicity E -asymmetry for fixed c.m. pion angles of $\cos\theta = 0, -0.65, -0.75,$ and -0.85 are plotted in Fig. 18 versus photon energy. The dotted, dashed, and solid curves represent the results of IA, IA+FOR, and IA+FOR+TBM, respectively. At $\cos\theta = 0$, the effect of FOR and TBM is rather small and the main contribution to the E -asymmetry comes from the IA term. In this case, the E -asymmetry begins with negative values at $E_\gamma = 500$ MeV due to higher positive values in $d\sigma^P/d\Omega$ and increases with increasing photon energy. At extreme

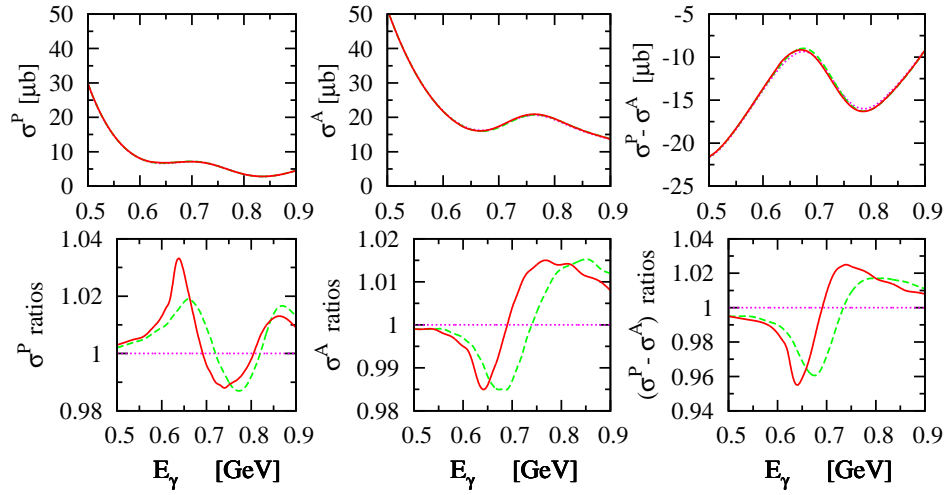


FIG. 17: (Color online) The helicity dependent total photo-absorption cross sections of $\vec{\gamma}d \rightarrow \pi^0 d$ for circularly polarized photons on a longitudinally polarized deuteron target with spin parallel σ^P (upper panel: left) and antiparallel σ^A (upper panel: middle) to the photon spin as functions of photon lab-energy. The upper right panel shows the difference $(\sigma^P - \sigma^A)$, i.e., the deuteron spin asymmetry of total photo-absorption cross section. Curve conventions as in Fig. 5. The lower panels show the corresponding ratios to the cross sections with respect to the IA value.

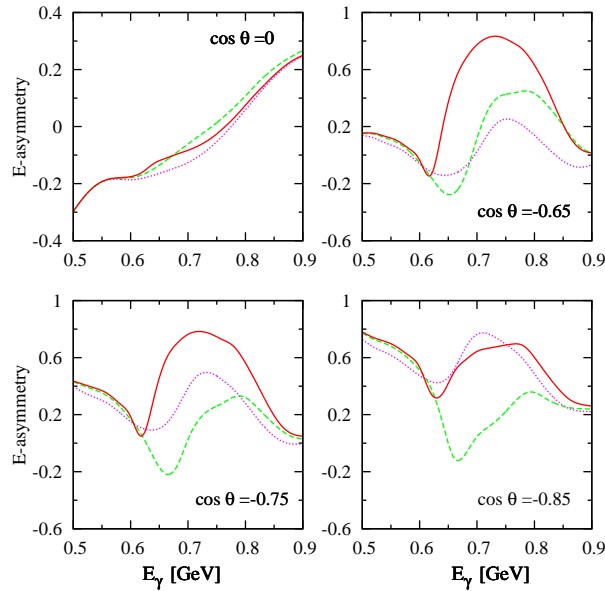


FIG. 18: (Color online) Same as in Fig. 5 but for the helicity E -asymmetry of $\vec{\gamma}d \rightarrow \pi^0 d$.

backward angles, the E -asymmetry decreases with increasing photon energy until a minimum value is reached at about $E_\gamma = 650$ MeV when only IA is considered. Then, it increases until a broad structure is obtained and decreases again.

Considering the FOR and TBM contributions leads, at extreme backward direction, to a strong enhancement for photon energies between 600 and 800 MeV. In this case, one observes a very strong cancellation between FOR and TBM terms which becomes stronger with increasing pion angles. At $\cos\theta = -0.75$, it is obvious that

the IA calculation (dotted curve) lies between IA+FOR (dashed curve) and IA+FOR+TMB (solid curve) predictions. This is not valid at higher and lower pion angles. The inclusion of TBM leads at $\cos\theta = -0.85$ to a very strong cancellation which is much smaller at $\cos\theta = -0.65$.

I. Contribution of $\gamma d \rightarrow \pi^0 d$ to the Deuteron GDH Integral

The GDH sum rule relates the difference between the two photo-absorption cross sections σ^P and σ^A to the anomalous magnetic moment of a particle. For a particle of mass M , charge eQ , anomalous magnetic moment κ , and spin S it reads

$$I^{GDH} = \int_0^\infty \frac{dE'_\gamma}{E'_\gamma} [\sigma^P(E'_\gamma) - \sigma^A(E'_\gamma)] = 4\pi^2 \kappa^2 \frac{e^2}{M^2} S. \quad (58)$$

The anomalous magnetic moment for the proton is $\kappa_p = 1.79$ n.m. and for the neutron it is $\kappa_n = -1.91$ n.m.. Therefore, the numerical results for the GDH sum rule for the proton $I_p^{GDH}(\infty) = 204.8 \mu\text{b}$ and the neutron $I_n^{GDH}(\infty) = 233.2 \mu\text{b}$.

Derivation of the GDH sum rule exclusively relies on very general principles such as Lorentz and gauge invariances, unitarity, crossing symmetry, and causality of the Compton scattering amplitude of a particle. Consequently, from the experimental and theoretical points of view, a test for various targets becomes of great interest.

The GDH sum rule can also be established for the deuteron because the low energy theorem holds its validity for composite systems such as the deuteron. The

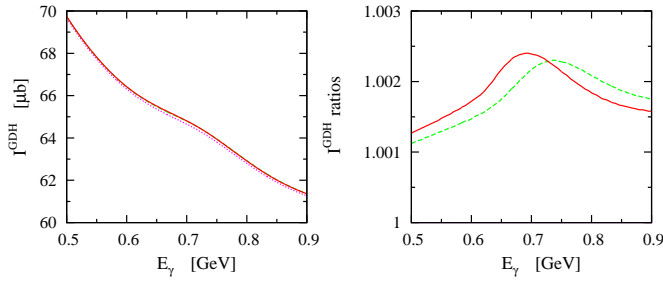


FIG. 19: (Color online) Left part: The Gerasimov-Drell-Hearn integral as a function of the upper integration limit of the $\vec{\gamma}d \rightarrow \pi^0 d$ reaction. Curve conventions as in Fig. 5. Right part: Ratios of the various approximations with respect to IA one. The green dashed and red solid curves show the relative deviations $I_{IA+FOR}^{GDH}/I_{IA}^{GDH}$ and $I_{IA+FOR+TBM}^{GDH}/I_{IA}^{GDH}$, respectively, as functions of photon lab-energy.

deuteron anomalous magnetic moment $\kappa_d = -0.143$ n.m. is relatively small, which yields a small value for the GDH sum rule $I_d^{GDH}(\infty) = 0.65 \mu\text{b}$. Because of its small binding energy, the deuteron has a quite extended spatial structure. The κ_d is small because of an almost complete cancellation of proton and neutron anomalous magnetic moments in the deuteron. When we consider the small GDH sum rule for the deuteron, we expect some cancellation to occur in the deuteron GDH integral as well. Thus, different production channels contributing to the integral must be analyzed separately to understand the overall value of the sum.

In the present work, however, we explicitly evaluate the contribution of $\gamma d \rightarrow \pi^0 d$ to the finite GDH integral up to 900 MeV as depicted in the left panel of Fig. 19 as a function of the upper integration limit [25]. We see that the curves representing various contributions to the scattering amplitude appear almost indistinguishable. In contrast to what we have found in the doubly polarized differential cross sections and the helicity E -asymmetry, we find that rescattering effects are negligible in the GDH integral near the η -threshold. The reason for this stems from the fact that the influence of rescattering effects on the helicity-dependent total cross sections difference $\sigma^P - \sigma^A$, entering the GDH integral, is also negligible (see the upper right panel of Fig. 17). In this case, the reaction is completely dominated by the IA contribution, the FOR and TBM contributions are negligible. Up to an energy of 900 MeV, a value of $I_{IA+FOR+TBM}^{GDH}(900 \text{ MeV}) = 61.36 \mu\text{b}$ to the finite GDH integral for the deuteron is explicitly computed by integration up to 900 MeV.

To clarify the relative size of FOR and TBM effects, we have presented in the right panel of Fig. 19 the ratios of the various approximations with respect to IA, $F_{IA+FOR}^{GDH}/I_{IA}^{GDH}$ (dashed curve) and $F_{IA+FOR+TBM}^{GDH}/I_{IA}^{GDH}$ (solid curve), as functions of photon lab-energy. We see that the effect of the intermediate ηNN three-body interaction is tiny.

J. Sensitivity to the Elementary $\gamma N \rightarrow \pi N$ Amplitude

In what follows, the sensitivity of the results for differential cross section, linear photon Σ -asymmetry, target asymmetries T_{11} and T_{2M} ($M = 0, 1, 2$), and beam-target asymmetry T_{10}^c for circularly polarized photons and vector polarized deuterons to the choice of elementary pion photoproduction amplitude is discussed [24]. We show results near η -threshold, using as elementary reaction amplitudes the ones provided by the dressed electromagnetic multipoles of the effective Lagrangian approach (ELA) from [49] and those obtained using the unitary isobar models MAID2003 [29] and MAID2007 [30]. For the deuteron wave function, we use the CD-Bonn potential [38].

The first comparison (Fig. 20) shows the sensitivity of the results for differential cross section on the elementary $\gamma N \rightarrow \pi N$ amplitude using the CD-Bonn potential [38] for the deuteron wave function. The solid (dotted) curve in Fig. 20 shows the results of modified three-body calculation IA+FOR+TBM using the unitary isobar model MAID2007 [30] (MAID2003 [29]), whereas the dashed curve shows the results of IA+FOR+TBM using the dressed ELA model [49]. We found that the differential cross section presents qualitative, but not quantitative, similar behaviors for different elementary operators. As one can see, the results using different elementary operators are rather different even at forward direction.

At backward direction, one sees that $d\sigma/d\Omega$ decreases with increasing photon lab-energy until a minimum close to the η -threshold is reached. Then the differential cross section increases with increasing the photon lab-energy until a broad plateau in the energy range 680-750 MeV is reached and decreases again. It is clear that the computations with different elementary amplitudes are quite different with a larger cross section predicted using MAID than the one obtained with ELA. In general, we obtain smaller values using ELA than using MAID. In addition, the plateau obtained using ELA appears as a peak at photon energy of about 700 MeV using MAID. When compared the results using the two versions of MAID, we see that the results using MAID2003 and MAID2007 are still quantitatively different but not qualitatively, specially at extremely backward direction. This discrepancy shows up the differences among elementary pion photoproduction operators. This means that the differential cross section is sensitive to the choice of the elementary amplitude.

For the reaction $\gamma d \rightarrow \pi^0 d$ at both forward and backward pion angles, spin asymmetries allow one to draw specific conclusions about details of the reaction mechanism. Therefore, we present in Fig. 21 the linear photon Σ -asymmetry as a function of photon lab-energy at various $\cos\theta$ using different elementary amplitudes and the deuteron wave function from CD-Bonn potential [38]. One sees that the values of Σ -asymmetry at $\cos\theta=0$ are larger (in absolute size) than its values at extreme back-

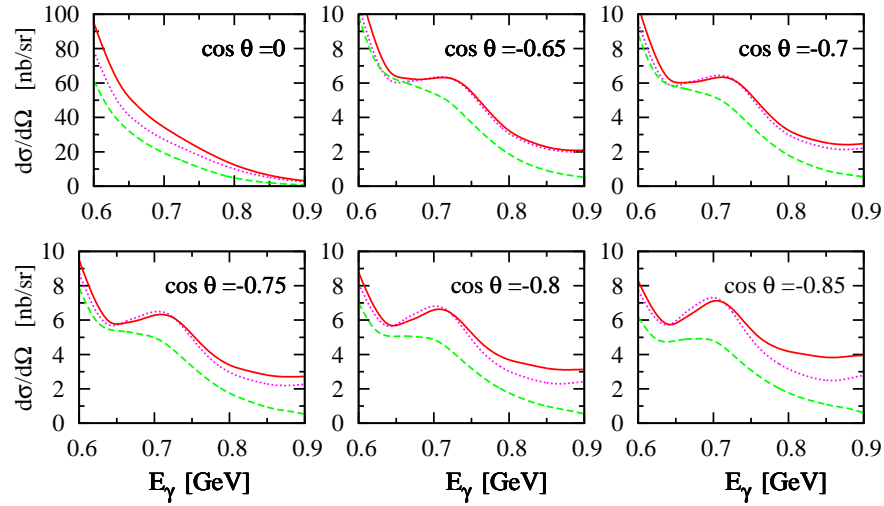


FIG. 20: (Color online) Differential $\gamma d \rightarrow \pi^0 d$ cross section using different elementary amplitudes and the deuteron wave function from CD-Bonn potential [38]. Curve conventions: green dashed, IA+FOR+TBM using ELA [49]; magenta dotted, IA+FOR+TBM using MAID2003 [29]; red solid, IA+FOR+TBM using MAID2007 [30].

ward pion angles. We would like to point out that in extremely forward and backward pion emission, i.e. for $\theta = 0$ and π , the Σ -asymmetry has to vanish because in that case the differential cross section cannot depend on the azimuthal angle ϕ , since at $\theta = 0$ or π the angle ϕ is undefined or arbitrary. It is also clear from Fig. 21 that the Σ -asymmetry is sensitive to the choice of elementary amplitude both at forward and backward directions.

If we focus our attention on the vector T_{11} and tensor T_{2M} ($M = 0, 1, 2$) target asymmetries, it is obvious from Fig. 22 that similar results are obtained. Qualitatively and quantitatively the predictions are rather different at forward and backward directions. From a quantitative point of view the results are very different for the vector and tensor target asymmetries. In other words, we can say that the MAID model provides different predictions for the differential cross section and target asymmetries at forward and backward pion angles. It seems that the results of $\gamma d \rightarrow \pi^0 d$ process are sensitive to the choice of the elementary amplitudes than to the rescattering effects. This shows that the process $\gamma d \rightarrow \pi^0 d$ can serve as a filter for the various elementary amplitudes. As in the case of Σ -asymmetry, the T_{11} , T_{21} , and T_{22} asymmetries have to vanish in extremely forward and backward pion emission, i.e. for $\theta = 0$ and π .

Fig. 23 displays the double polarization T_{10}^c -asymmetry of the $\vec{\gamma}d \rightarrow \pi^0 d$ reaction as a function of photon lab-energy at various $\cos \theta$ using different elementary amplitudes and the deuteron wave function from CD-Bonn potential [38]. The dashed, dotted, and solid curves show the results of the asymmetry T_{10}^c with inclusion of modified three-body calculation IA+FOR+TBM using the dressed ELA model [49], the unitary isobar model MAID2003 [29], and MAID2007 [30], respectively. The T_{10}^c -asymmetry is of important, because it determines the GDH sum rule [37]. It is very clear from Fig.

23 that the results using various elementary amplitudes are quite different at forward and backward pion angles. This difference is more noticeable when one compares the dashed (ELA) with the solid (MAID2007) curves. Comparing the dotted (MAID2003) to the solid (MAID2007) curves reveals that the dependence of the results on the two MAID versions is also considerable. This means that the T_{10}^c -asymmetry is also sensitive to the choice of the elementary pion photoproduction operator on the free nucleon.

K. Dependence on Modern NN Potential Models

As next, the sensitivity of the $\gamma d \rightarrow \pi^0 d$ observables to the choice of modern NN potential model governs the deuteron wave function is discussed [26]. We show results for differential cross section, photon Σ -asymmetry, vector T_{11} and tensor T_{2M} ($M = 0, 1, 2$) deuteron asymmetries, photon-deuteron double polarization T_{10}^c -asymmetry, and the GDH integral for the deuteron using for the deuteron wave function the CD-Bonn potential [38], Bonn potential (full model) [50], and Bonn potential (OBEPQ version) [48]. For the elementary amplitude we use the MAID2007 model [30].

Fig. 24 shows the sensitivity of our results for the differential cross section to the deuteron wave function using the MAID2007 model [30] for the elementary amplitude. The solid, dashed, and dotted curves in Fig. 24 show the results of IA+FOR+TBM using the Bonn potential (full model) [50], Bonn potential (OBEPQ version) [48], and CD-Bonn potential [38], respectively. In general, one sees qualitatively similar behaviors for the differential cross section at backward pion angles. The results using various NN potential models for the deuteron wave function are quite different, specially at the plateau

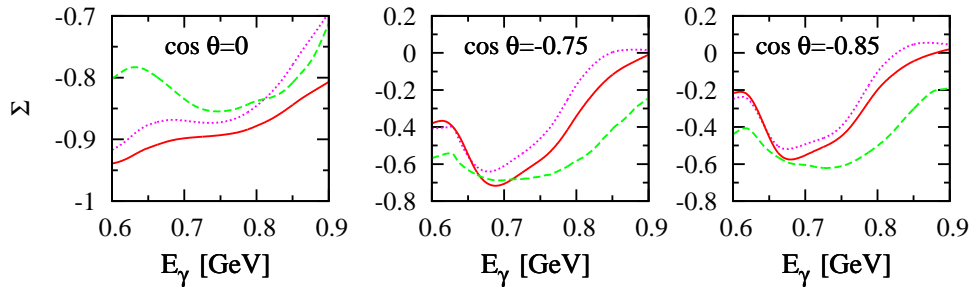


FIG. 21: (Color online) Same as in Fig. 20 but for the linear photon Σ -asymmetry of $\vec{\gamma}d \rightarrow \pi^0 d$.

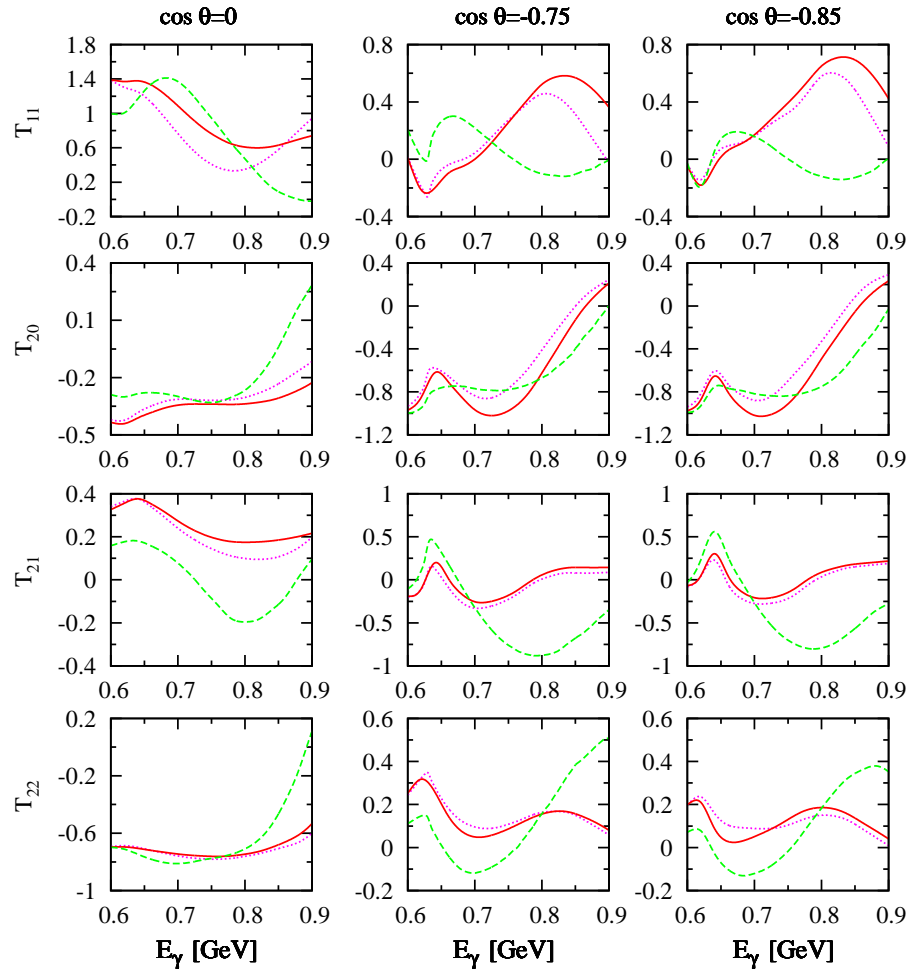


FIG. 22: (Color online) Same as in Fig. 20 but for the target asymmetries T_{11} , T_{20} , T_{21} , and T_{22} of $\vec{\gamma}d \rightarrow \pi^0 d$.

region where sizeable differences are obtained. We found that the results using the deuteron wave function of the CD-Bonn potential is greater than those using Bonn potential (OBEPQ version) and the latter is greater than the ones using Bonn potential (full model). This means that the differential cross section is also sensitive to the choice of the NN potential model used for the deuteron wave function.

The sensitivity of linear photon Σ -asymmetry to the deuteron wave function is displayed in Fig. 25. At

$\cos\theta=0$, one obtains small differences between computations with different NN potential models used for the deuteron wave function. At extreme backward pion angles, one can see that the difference between curves is quite large, in particular at photon lab-energies very close to η -threshold. At η -threshold energy, the solid curve which represents the results using the old full-Bonn potential is far from other curves. This means that the Σ -asymmetry is sensitive to the choice of NN potential model governs the deuteron wave function.

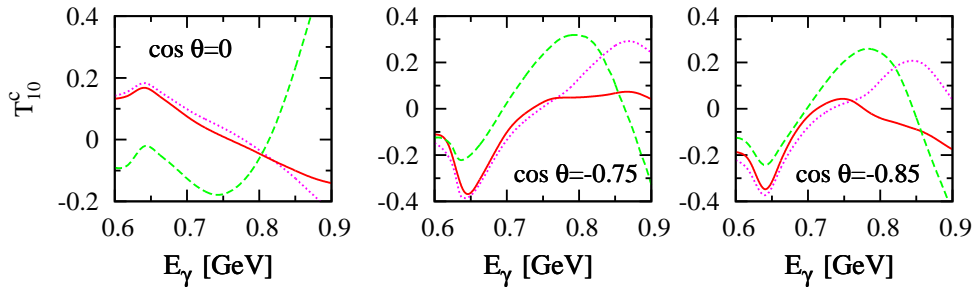


FIG. 23: (Color online) Same as in Fig. 20 but for the double polarization T_{10}^c -asymmetry for circular polarized photons and oriented deuterons of $\vec{\gamma}d \rightarrow \pi^0 d$.

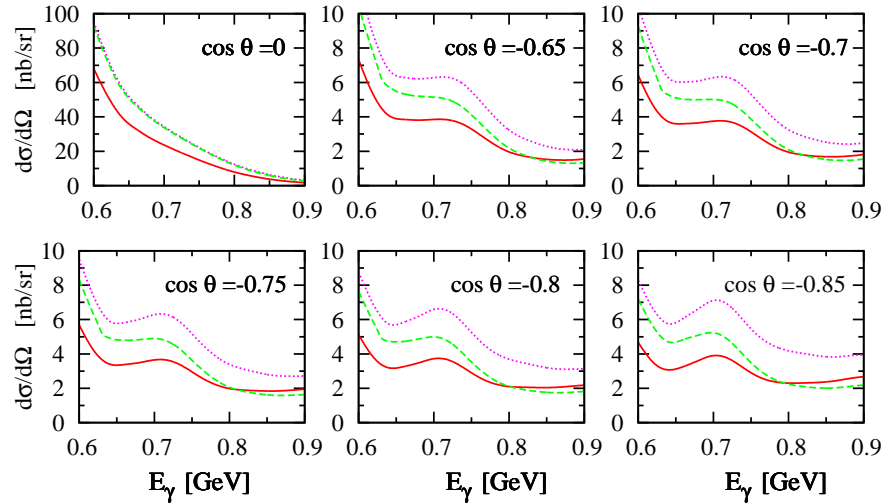


FIG. 24: (Color online) Differential $\gamma d \rightarrow \pi^0 d$ cross section using different deuteron wave functions and the elementary amplitude from MAID2007 [30]. Curve conventions: green dashed, IA+FOR+TBM using Bonn potential (OBEPQ version) [48]; magenta dotted, IA+FOR+TBM using CD-Bonn potential [38]; red solid, IA+FOR+TBM using Bonn potential (full model) [50].

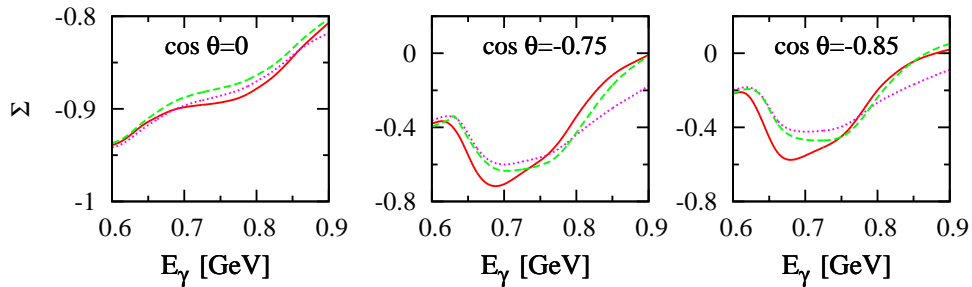


FIG. 25: (Color online) Same as in Fig. 24 but for the linear photon Σ -asymmetry of $\vec{\gamma}d \rightarrow \pi^0 d$.

If we focus our attention on the vector T_{11} and tensor T_{2M} ($M = 0, 1, 2$) target asymmetries, it is obvious from Fig. 26 that similar results are obtained. Qualitatively and quantitatively the predictions are rather different at forward and backward directions. From a quantitative point of view the results are very different for the tensor target asymmetry T_{20} . In other words, we can say that the MAID model provides different predictions for the differential cross section and tensor target

spin T_{20} -asymmetry at forward and backward pion angles. It seems that the results of $\gamma d \rightarrow \pi^0 d$ process are sensitive to the choice of the elementary amplitudes and deuteron wave functions than to the rescattering effects. This shows that the process $\gamma d \rightarrow \pi^0 d$ can serve as a filter for the various elementary amplitudes and different NN potential models used for deuteron wave function.

Fig. 27 displays the role of the double polarization T_{10}^c -asymmetry of the $\vec{\gamma}d \rightarrow \pi^0 d$ reaction as a function of

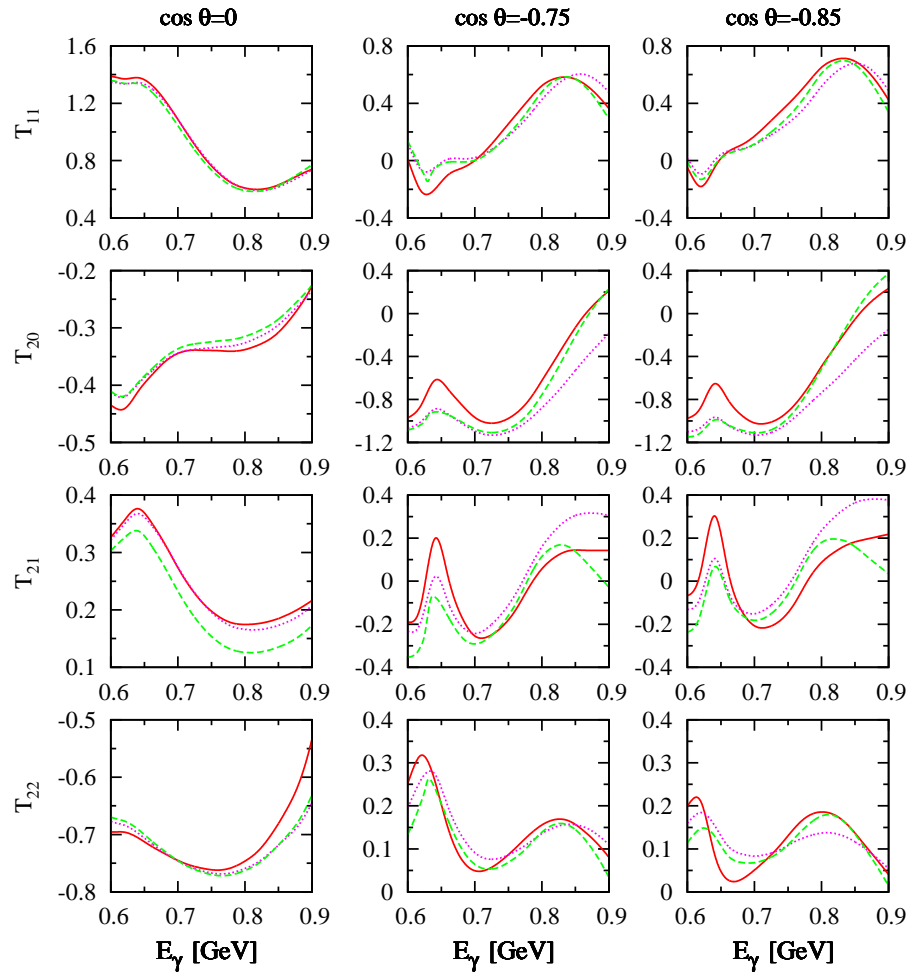


FIG. 26: (Color online) Same as in Fig. 24 but for the target asymmetries T_{11} , T_{20} , T_{21} , and T_{22} of $\gamma\vec{d} \rightarrow \pi^0 d$.

photon lab-energy at various $\cos\theta$ on the choice of NN potential model used for the deuteron wave function. The solid, dashed, and dotted curves in Fig. 27 show the results of IA+FOR+TBM using the Bonn potential (full model) [50], Bonn potential (OBEPQ version) [48], and CD-Bonn potential [38], respectively. In general, one sees that the results using various NN potential models for the deuteron wave function are quite different, specially at energies very close to η -threshold. We found that the results using the deuteron wave function of the CD-Bonn potential is different from those using Bonn potential (OBEPQ version) and Bonn potential (full model). This means that the double polarization T_{10}^c -asymmetry for circular polarized photons and oriented deuterons is also sensitive to the choice of the NN potential model used for the deuteron wave function. As already mentioned above, this asymmetry is of particular interest, because it is related to the spin asymmetry $\sigma^P - \sigma^A$ which determines the GDH sum rule [37].

In Fig. 28 we show the helicity-dependent differential cross section difference $d(\sigma^P - \sigma^A)/d\Omega$ (upper part) and the E -asymmetry (lower part) as functions of photon energy at different values of $\cos\theta$ using the MAID2007

model [30] for the elementary pion photoproduction operator. The dotted, dashed, and solid curves in Fig. 28 show the results of IA+FOR+TBM using the deuteron wave function of the CD-Bonn potential [38], Bonn potential (OBEPQ version) [48], and Bonn potential (full model) [50], respectively. It is clear that the results using various NN potential models for the deuteron wave function are quite different. Even at $\cos\theta = 0$, small differences between results with different deuteron wave functions is obtained. This discrepancy is more noticeable at photon energies around $E_\gamma = 750$ MeV and extreme backward pion angles, and shows up the differences among deuteron wave functions.

If we focus our attention on the helicity-dependent total photoabsorption cross section difference $\sigma^P - \sigma^A$ (left panel in Fig. 29), we see that the curves computed using different deuteron wave functions seem similar. However, these computations provide quite different results for the GDH integral as shown in the right panel of Fig. 29. We obtain larger values using CD-Bonn and OBEPQ potential models than using Bonn (full model).

The explicit evaluation of the contributions from pion and eta production to the finite GDH integral for the

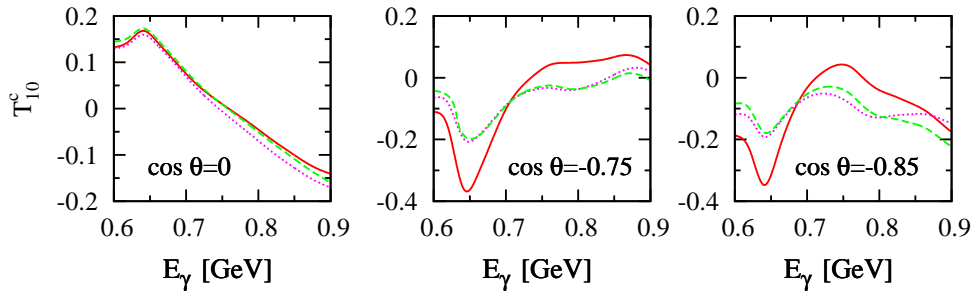


FIG. 27: (Color online) Same as in Fig. 24 but for the double polarization T_{10}^c -asymmetry for circular polarized photons and oriented deuterons of $\vec{\gamma}\vec{d} \rightarrow \pi^0 d$.

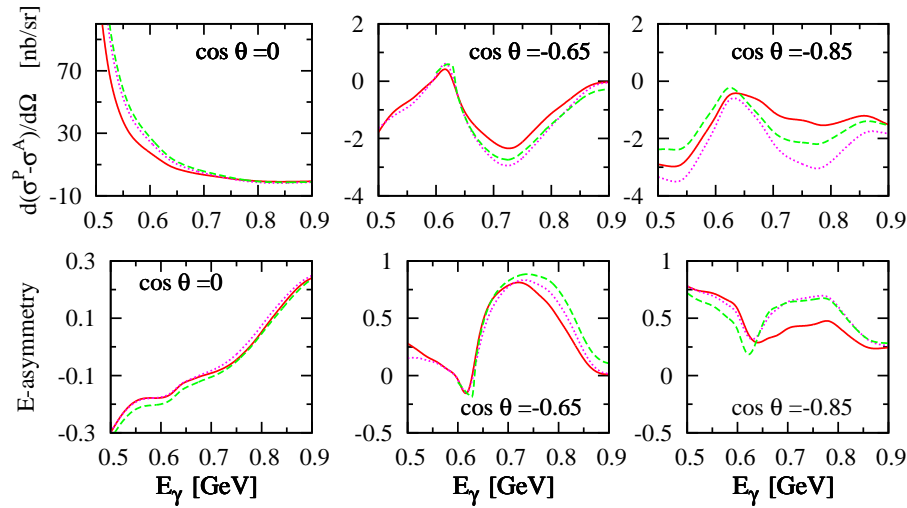


FIG. 28: (Color online) Same as in Fig. 24 but for the differential polarized cross section difference $d(\sigma^P - \sigma^A)/d\Omega$ for parallel and antiparallel helicity states of photon and deuteron (upper part) and the helicity E -asymmetry (lower part) of $\vec{\gamma}\vec{d} \rightarrow \pi^0 d$.

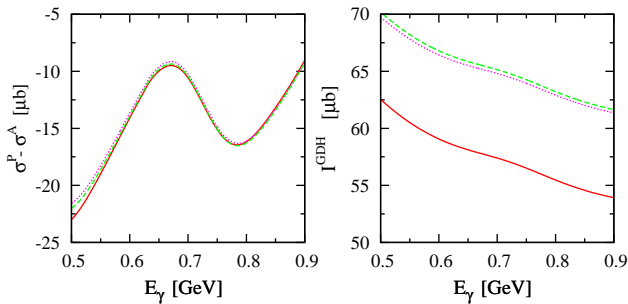


FIG. 29: (Color online) Same as in Fig. 24 but for the helicity-dependent total photoabsorption cross section difference $\sigma^P - \sigma^A$ of $\vec{\gamma}\vec{d} \rightarrow \pi^0 d$ (left panel) and the corresponding GDH integral as a function of the upper integration limit (right panel).

deuteron up to 1.5 GeV was performed in Ref. [51]. Up to an energy of 900 MeV, a value of about $53 \mu\text{b}$ was found for the contribution of the $\gamma d \rightarrow \pi^0 d$ reaction. In the present work, we computed a large positive contribution, $I_{IA+FOR+TBM}^{GDH}(900 \text{ MeV}) = 61.36 \mu\text{b}$, to the value of the finite GDH integral for the deuteron integrated up

to 900 MeV. The difference between both values seems likely to be due to the fact that we used a different NN potential model for the deuteron wave function. Also, the MAID model is used for the elementary pion photoproduction operator in both cases. We would like to mention that the Bonn potential (full model) [50] is originally written in p -space and is energy-dependent that makes its applications in nuclear calculations problematic. To resolve some of the problems, a parameterization of the potential in terms of OBE's in both p -space and r -space is given, which is always called OBEPQ potential [48]. This potential is energy-independent that in turn simplifies its applications in nuclear structure and nucleon-nucleus scattering calculations. It includes the tensor component which is certainly very important in the energy region of large momentum transfers. The CD-Bonn potential [38] is an improved and updated version of the Bonn potential (full model) [50] and the OBEPQ potential [48].

We present in Table I the extracted values of the GDH integral up to 900 MeV for the $\gamma d \rightarrow \pi^0 d$ reaction using MAID2007 as elementary operator and different NN potential models for the deuteron wave function.

TABLE I: Contribution of coherent pion photoproduction on the deuteron to the finite GDH integral explicitly integrated up to $E_\gamma = 900$ MeV in μb using different NN potential models for the deuteron wave functions and the elementary pion photoproduction operator from MAID2007 model [30].

NN potential model	I_{IA}^{GDH}	I_{IA+FOR}^{GDH}	$I_{IA+FOR+TBM}^{GDH}$
CD-Bonn [38]	61.27	61.38	61.36
OBEPQ [48]	61.56	61.67	61.66
Bonn (full model) [50]	53.83	53.94	53.93

After including rescattering effects, we find that CD-Bonn: $I_{IA+FOR+TBM}^{GDH}(900 \text{ MeV}) = 61.36 \mu\text{b}$, OBEPQ: $I_{IA+FOR+TBM}^{GDH}(900 \text{ MeV}) = 61.66 \mu\text{b}$, whereas Bonn (full model): $I_{IA+FOR+TBM}^{GDH}(900 \text{ MeV}) = 53.93 \mu\text{b}$. The latter value is in agreement with the value $I_{\gamma d \rightarrow \pi^0 d}^{GDH}(900 \text{ MeV}) \simeq 53 \mu\text{b}$ predicted in Ref. [51] in which also the Bonn potential (full model) was used. This difference in the values of the deuteron GDH integral - in spite of the tiny dissimilarity shown in the left panel of Fig. 29 - reflects its sensitivity to the choice of NN potential model used for the deuteron wave function.

The deviation of the obtained results is quite large for different deuteron wave functions. An important source for the origin of this strong dependence is the tensor force between two nucleons. A measure of the strength of the tensor force is expressed in terms of the D -state probability P_D obtained for the deuteron [52]. The D -state probabilities for the NN potentials used in the present work are $P_D = 4.25\%$, 4.38% and 4.85% for the Bonn (full) [50], Bonn (OBEPQ) [48], and CD-Bonn [38] potentials, respectively. The results using the deuteron wave function of the CD-Bonn potential, which has a larger value of P_D in comparison to other potentials, are quite different. It was shown by various authors [12, 15] that the spin observables for the $\gamma d \rightarrow \pi^0 d$ process are quite sensitive to the deuteron wave function. It was reported in Ref. [12] that, in the photon energy range 600-700 MeV, the differential cross section and the photon Σ -asymmetry are highly sensitive to the deuteron wave function. The role of the 3D_1 -configuration in the deuteron wave function has also been studied by Kamalov *et al.* [15]. They found that the D -wave contribution becomes manifest at pion angle $\theta > 90^\circ$ for photon energies $E_\gamma > 300$ MeV. The tensor target asymmetries were found to be very sensitive to the deuteron D -state component, in particular in the region of $90^\circ < \theta < 150^\circ$.

From the preceding discussion it is apparent that complete ηNN three-body calculation and the choices of both the elementary operator and deuteron wave function have a visible effect on the differential cross section and spin asymmetries at extreme backward pion angles.

L. Comparison with Experimental Data and Other Theoretical Models

We now turn to a comparison of our results for the differential cross section and the linear photon asymmetry with available experimental data and other theoretical models. Fig. 30 shows a comparison of the results for differential cross section with the experimental data from [21] and CLAS Collaboration [3, 4]. The calculation shown by the dashed curve obtained with the amplitude of the IA alone, while the one shown by the solid curve obtained with the modified three-body amplitude, IA+FOR+TBM. It is clear from Fig. 30 that a satisfactory agreement between our calculation and the experimental data is obtained at forward pion angles near the η -production threshold.

At extremely backward pion angles, one can see that our predictions in the pure IA and with inclusion of modified three-body calculation cannot describe the experimental data from [21], since major discrepancies are evident. Compared to the experimental data from CLAS Collaboration [3, 4], we also found that the theory underestimates the data for differential cross section at backward direction by about one order of magnitude. The same conclusions were drawn by the authors in Ref. [17], where the differential cross section was also far below the data in the same kinematical region.

Now, we turn to the differences obtained between our results and the ones of Ref. [17] for differential cross section. To make the comparison very clear we show in Fig. 31 the modified three-body calculation of the differential cross section. The dashed curve shows the results of IA+FOR+TBM using the MAID2003 amplitude [29] for the elementary $\gamma N \rightarrow \pi N$ process and the Bonn potential (OBEPQ version) [48] for deuteron wave function (the same as in Ref. [17]), while the solid curve displays the corresponding results using the MAID2007 amplitude for the former and the CD-Bonn potential [38] for the latter. Our results given by the dashed curve are in good agreement with the corresponding ones shown in Fig. 3 of Ref. [17]. Nevertheless, we obtain big differences between the dashed and solid curves, specially at extremely backward pion angles. We would like to mention that upgrading MAID2003 to MAID2007 produces differences that may be as larger as 30% at backward pion angles and higher energies. And the use of the CD-Bonn NN potential for the deuteron wave function doubles the cross section in this region. This means in particular that the results of differential cross section are sensitive to elementary amplitudes and deuteron wave functions.

To the best of our knowledge, very few data points are available for the linear photon Σ -asymmetry in the kinematics of the current situation, but with regard to the deuteron and photon-deuteron asymmetries, there are no data exist in the kinematic region of our interest in the present work. We show in Fig. 32 a comparison between our IA+FOR+TBM prediction for the Σ -asymmetry (solid curve) and the experimental data

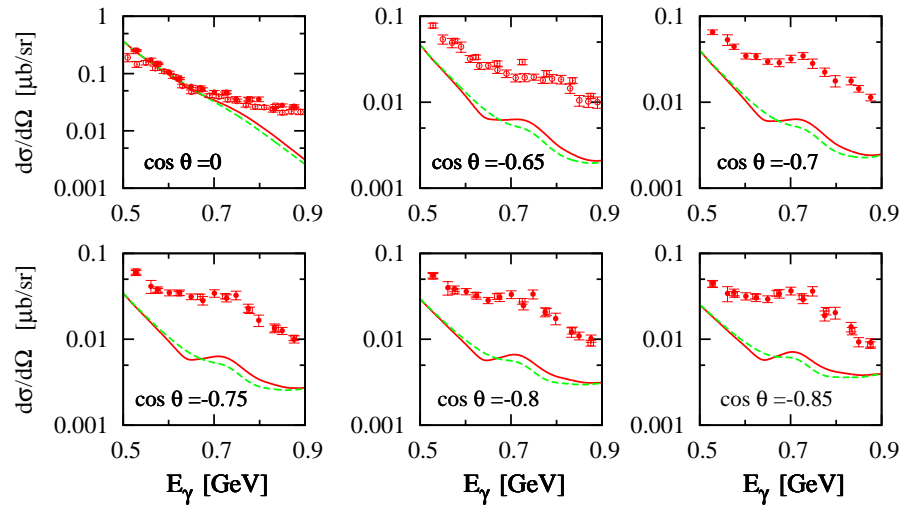


FIG. 30: (Color online) The differential $\gamma d \rightarrow \pi^0 d$ cross section, using the logarithmic scale, as a function of photon lab-energy at various values of $\cos \theta$ using MAID2007 [30] and deuteron wave function from the CD-Bonn potential [38]. The dashed and solid curves show the IA and IA+FOR+TBM calculations, respectively. Experimental data are from [21] (open circles), CLAS Collaboration [3] (open squares), and CLAS Collaboration [4] (solid circles).

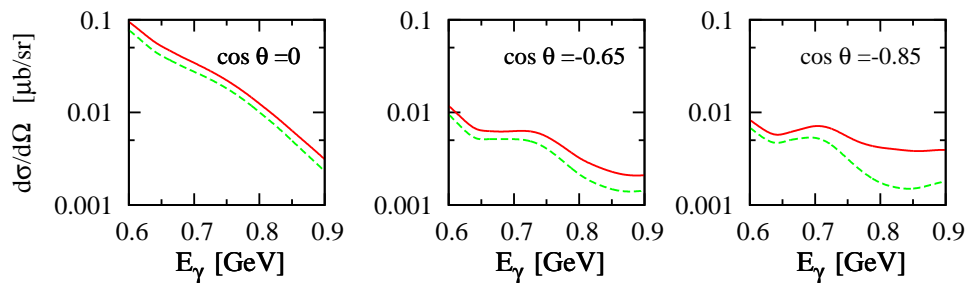


FIG. 31: (Color online) The role of complete three-body calculation on the differential $\gamma d \rightarrow \pi^0 d$ cross section, using the logarithmic scale, as a function of photon lab-energy at various $\cos \theta$. Curve conventions: green dashed, IA+FOR+TBM using MAID2003 [29] and deuteron wave function from Bonn potential (OBEPQ version) [48]; red solid, IA+FOR+TBM using MAID2007 [30] and deuteron wave function from CD-Bonn potential [38].

from YerPhi Collaboration [5] at $\theta=130^\circ$ as a function of photon lab-energy. In Fig. 32 we also exhibit our results with the model predictions of Imanishi *et al.* [53] (dotted curve). This model is based on the Glauber multiple scattering theory and takes into account the contributions from single scattering diagram (IA*) from Ref. [54], double scattering diagram with intermediate πN -rescattering (DS) and that from possible dibaryon resonance (DB) from Ref. [53].

We found that adding the contribution of the intermediate ηNN three-body interaction to the scattering amplitude does not remove the discrepancy with the experimental data. Although, a noticeable influence of rescattering effects is found, one notes that the predictions can hardly provide a reasonable description of the data. The theory is overestimated in the maximum and at lower energies but slightly underestimated in the energy region above $E_\gamma = 800$ MeV. It is also clear that the experimental data on the Σ -asymmetry do not agree with the predictions of Imanishi *et al.* [53], in particular at energies

above $E_\gamma = 750$ MeV. In the region $E_\gamma < 750$ MeV, better agreement was obtained in [53]. The authors of Ref. [53] argue that the main reason of their disagreement with the data could be due to the neglected contributions from three- and higher-order scattering terms.

Comparing our results (solid curve) with the predictions of Imanishi *et al.* [53] (dotted curve), we obtain a strong disagreement, in particular at photon energies above $E_\gamma = 700$ MeV. Their predictions at lower energies are similar to ours, also larger values at all energies are obtained in our case. The Σ -asymmetry is found to be positive in both cases until $E_\gamma \simeq 750$ MeV. At higher energies the Σ -asymmetry change the sign in the case of Imanishi *et al.* predictions [53] which is not the case in ours. This can occur through differences in the elementary amplitude and deuteron wave function. In addition, the intermediate ηN -rescattering, which was neglected in [53], is found to be important near η -threshold (see, for example, Refs. [16, 17, 22]).

We now turn to a comparison of our results for the

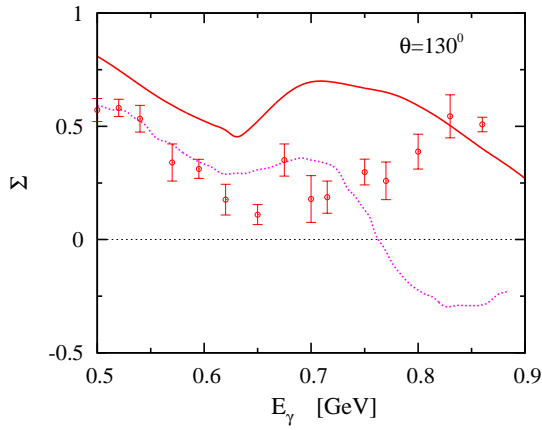


FIG. 32: (Color online) The beam asymmetry Σ for linearly polarized photon of $\gamma d \rightarrow \pi^0 d$ as a function of photon lab-energy at $\theta = 130^\circ$. The red solid curve is the IA+FOR+TBM prediction of the present work, while the magenta dotted curve is the IA*+DS+DB calculation (see text) of Refs. [53, 54] (based on the model of Ref. [21]). Experimental data are from YerPhi Collaboration [5].

tensor target spin asymmetries T_{20} , T_{21} , and T_{22} with available experimental data. There is a reasonable interest and demand in the experimental community for refined calculations and effects which have not been traditionally included in the treatment of two-body deuteron photodisintegration and coherent π^0 -photoproduction on the deuteron [6–8]. The first data on tensor target spin asymmetries T_{20} , T_{21} , and T_{22} of the $\gamma d \rightarrow \pi^0 d$ reaction have been measured at the VEPP-3 storage ring [6]. Fig. 33 shows a comparison of the results for the tensor target spin asymmetries T_{20} , T_{21} , and T_{22} with the experimental data from VEPP-3 [6]. These spin asymmetries are presented as functions of photon energy at $\theta = 90^\circ$ – 145° (left panels) and as functions of pion angle at $E_\gamma = 250$ – 450 MeV (right panels). The solid curve in Fig. 33 shows the results of IA+FOR+TBM using the MAID-2007 amplitude [30] for the elementary operator and the Bonn potential (OBEPQ version) [48] for the deuteron wave function. It is clear from Fig. 33 that the predictions with ηNN three-body contribution can hardly provide a reasonable description of the data. The best agreement is obtained in the case of T_{20} -asymmetry. In the case of T_{21} -asymmetry, the theory is underestimated at pion angles below 140° , but it is slightly overestimated at extremely backward angles. It is noted here that the accuracy of the experimental data [6] was not high because the detection system of the two-body deuteron photodisintegration experiment was not optimal to register neutral pions [7].

Recently, more precise data for the T_{20} -asymmetry have been measured [7]. Our results for the asymmetry T_{20} as a function of photon energy at fixed values of pion angle are plotted in Fig. 34 in comparison with the experimental data from VEPP-3 [7]. The solid curve corresponds to the IA+FOR+TBM calculations using the MAID-2007 model [30] for the elementary amplitude and

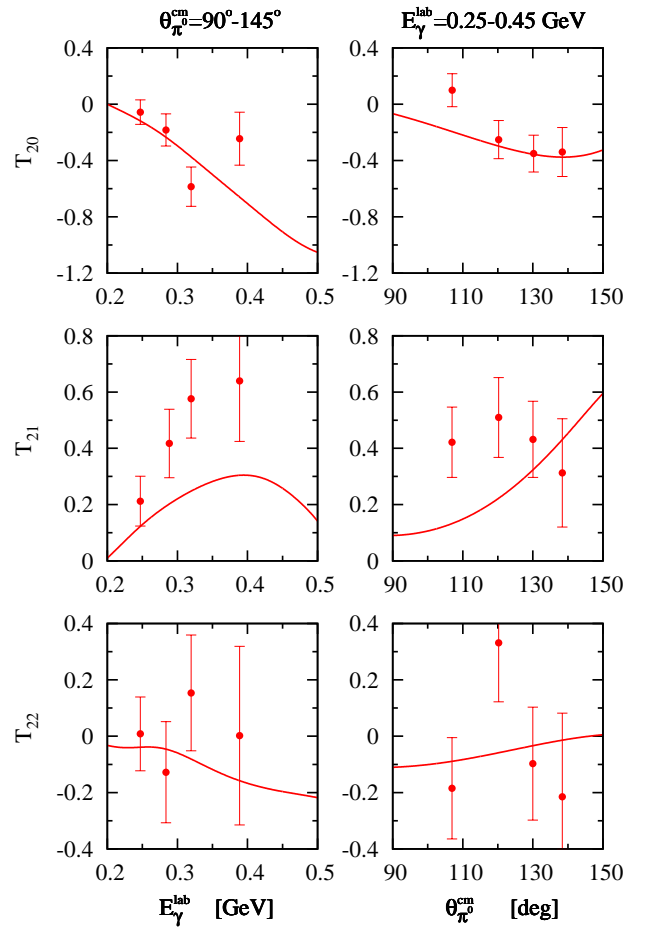


FIG. 33: (Color online) Tensor target spin asymmetries T_{20} , T_{21} , and T_{22} for $\gamma d \rightarrow \pi^0 d$ as functions of photon lab-energy E_γ^{lab} at pion angle $\theta_{\pi^0}^{\text{cm}} = 90^\circ - 145^\circ$ (left panels) and as functions of $\theta_{\pi^0}^{\text{cm}}$ at $E_\gamma^{\text{lab}} = 250 - 450$ MeV (right panels). The solid curve corresponds to the IA+FOR+TBM calculation using the MAID-2007 model [30] for the elementary amplitude and the Bonn potential (OBEPQ) [48] for the deuteron wave function. Experimental data are from VEPP-3 [6].

the Bonn potential (OBEPQ) [48] for the deuteron wave function. It is observed that the IA+FOR+TBM calculations and the experimental data are consistent in the photon energy region below 400 MeV. At $E_\gamma > 400$ MeV, one sees that the calculations slightly underestimate the data.

Figure 35 shows a comparison between our results for the T_{20} -asymmetry as a function of pion angle at fixed values of photon energy and the experimental data from the VEPP-3 storage ring [7]. The solid curve corresponds also here to the IA+FOR+TBM calculations using the MAID-2007 model [30] for the elementary amplitude and the Bonn potential (OBEPQ) [48] for the deuteron wave function. The best agreement between theory and experiment is seen at photon energies close to the $\Delta(1232)$ -resonance region. At photon energies below (above) 340 MeV, one sees that the theory overestimates (underesti-

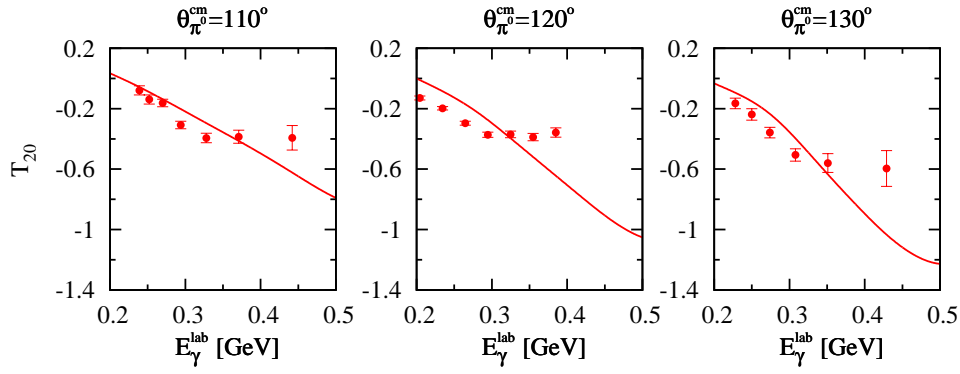


FIG. 34: (Color online) The tensor target spin asymmetry T_{20} for $\gamma\vec{d} \rightarrow \pi^0 d$ as a function of photon lab-energy E_{γ}^{lab} at pion angle $\theta_{\pi^0}^{\text{cm}} = 110^\circ$ (left panel), 120° (middle panel), and 130° (right panel). The solid curve corresponds to the IA+FOR+TBM calculation using the MAID-2007 model [30] for the elementary amplitude and the Bonn potential (OBEPQ) [48] for the deuteron wave function. Experimental data are from VEPP-3 [7].

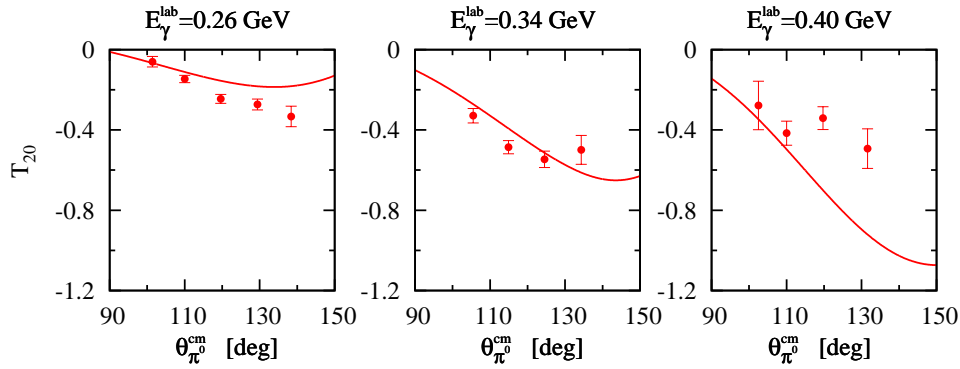


FIG. 35: (Color online) The tensor target spin asymmetry T_{20} for $\gamma\vec{d} \rightarrow \pi^0 d$ as a function of pion angle $\theta_{\pi^0}^{\text{cm}}$ at photon lab-energies $E_{\gamma}^{\text{lab}} = 260$ MeV (left panel), 340 MeV (middle panel), and 400 MeV (right panel). The solid curve corresponds to the IA+FOR+TBM calculation using the MAID-2007 model [30] for the elementary amplitude and the Bonn potential (OBEPQ) [48] for the deuteron wave function. Experimental data are from VEPP-3 [7].

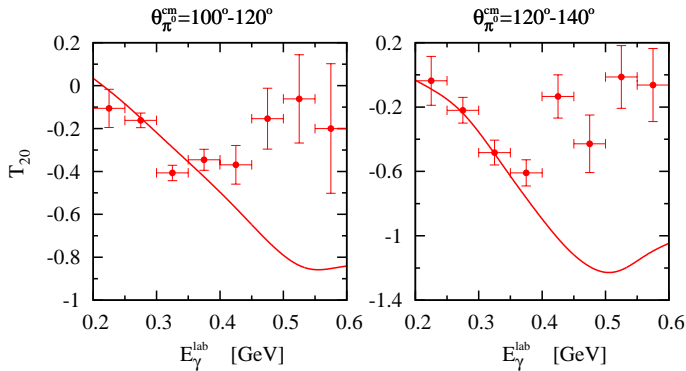


FIG. 36: (Color online) The tensor target spin asymmetry T_{20} for $\gamma\vec{d} \rightarrow \pi^0 d$ as a function of photon lab-energy E_{γ}^{lab} at pion angle in regions $\theta_{\pi^0}^{\text{cm}} = 100^\circ - 120^\circ$ (left panel) and $\theta_{\pi^0}^{\text{cm}} = 120^\circ - 140^\circ$ (right panel). The solid curve corresponds to the IA+FOR+TBM calculation using the MAID-2007 model [30] for the elementary amplitude and the Bonn potential (OBEPQ) [48] for the deuteron wave function. Experimental data are from VEPP-3 [8].

mates) the experimental data at backward pion angles.

Most recently, much more precise data for the T_{20} asymmetry in coherent photoproduction of π^0 -meson from the deuteron has been measured in the VEPP-3 storage ring [8]. The asymmetry T_{20} is plotted in Fig. 36 as a function of photon energy at pion angle in regions 100° - 120° (left panel) and 120° - 140° (right panel) in comparison with the recent experimental data from Ref. [8]. The solid curve corresponds again to the IA+FOR+TBM calculations using the MAID-2007 model [30] for the elementary amplitude and the Bonn potential (OBEPQ) [48] for the deuteron wave function. One can see from Fig. 36 that a good agreement between our predictions for IA+FOR+TBM and experimental data is obtained at photon energies less than 400 MeV. At photon energies above 400 MeV, one can see that the calculations of IA+FOR+TBM contradict the data. In this case, the predictions considerably underestimate the experimental data.

Recently, the helicity E -asymmetry of π^0 -photoproduction on the free proton has been measured by the CBELSA/TAPS Collaboration [55]. It was found

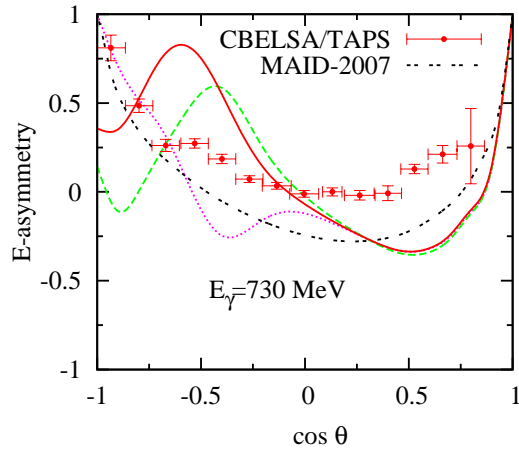


FIG. 37: (Color online) The helicity E -asymmetry of $\vec{\gamma}d \rightarrow \pi^0 d$ versus $\cos \theta$ in the γd c.m. frame at $E_\gamma = 730$ MeV. Notation of the curves as in Fig. 5, while the black double-dashed curve shows the results of $\vec{\gamma}p \rightarrow \pi^0 p$ using the MAID2007 model [30]. The experimental data of π^0 -photoproduction off free protons are taken from the CBELSA/TAPS Collaboration [55].

that the E -asymmetry revealed remarkable differences in the predictions of MAID2007 model [30] even in the second resonance region around $E_\gamma = 750$ MeV. The origin of these discrepancies remains unclear. Therefore, we displayed in Fig. 37 the E -asymmetry as a function of $\cos \theta$ at $E_\gamma = 730$ MeV in comparison with the experimental data of $\vec{\gamma}p \rightarrow \pi^0 p$ from [55]. The dotted, dashed, and solid curves show the results of IA, IA+FOR, and IA+FOR+TBM, respectively. The double-dashed curve displays the results of π^0 -photoproduction on the free proton using MAID2007 model [30]. At very small pion angles, the E -asymmetry is mostly determined by the elementary amplitude. This is not the case at backward angles, where sizeable differences between the results on the nucleon and deuteron are obtained. When rescattering effects are considered, the E -asymmetry exhibits a peak structure which is due to the presence of the $S_{11}(1535)$ resonance in the ηN -rescattering diagram. A very big difference between IA and IA+FOR is obtained at $\theta = 180^\circ$. The inclusion of TBM reduces this difference to about one half. The large differences between experimental data and predictions shown in Ref. [55] are also observed here even if the FOR and TBM effects are taken into account. These differences may be due to interference with contributions from resonances other than $S_{11}(1535)$. It was shown in [55] that the E -asymmetry is highly sensitive to the contributions from s -channel resonances.

Possible explanation of the existing discrepancy between our predictions and the experimental data at high photon energies can be attributed to the contributions from two-body mechanisms in the photoproduction amplitude, e.g. meson-exchange current, isobar configuration in the deuteron wave function, etc, and other res-

onance amplitudes besides the $S_{11}(1535)$ contribution. One might expect that the influence of these effects maybe important for the theoretical description of tensor target spin asymmetries. For example, it was shown in Ref. [55] that the helicity E -asymmetry is very sensitive to the contributions from s -channel resonances. In addition, meson-exchange currents were found to be quite significant for π^+ -photoproduction on ^3He in Ref. [56]. The role of two-body effects from hadronic rescattering and electromagnetic meson-exchange currents on coherent η -photoproduction from the deuteron in the region of the $S_{11}(1535)$ resonance was investigated in [57]. It was found that two-body effects give significant contributions to polarization observables of the $\gamma d \rightarrow \eta d$ reaction at backward angles and higher energies, as there are several observables which are very sensitive to hadronic rescattering and meson-exchange currents. It is intuitively clear that as long as small pion angles are considered where the two-nucleon effects are minimal, the magnitude of the spin asymmetries should be mostly determined by the elementary amplitude. With increasing pion angles, small internuclear distances come into play and thus corrections to the IA calculation from the two-nucleon mechanisms become more and more important.

It is also clear that the πN elastic scattering cross sections are much larger than the $\pi N \rightarrow \eta N$ cross sections, and $N(1520)\frac{3}{2}^-$ also strongly couples to the πN channel in the considered energy region. Therefore, the two-step processes including $N(1520)\frac{3}{2}^-$ and the three-body πNN processes are expected to have contribution similar to $N(1535)\frac{1}{2}^-$ and three-body ηNN processes.

IV. CONCLUSIONS AND OUTLOOK

The main object of this review was to incorporate the rescattering amplitudes in the formalism for coherent π^0 -photoproduction from the deuteron near the η -production threshold to study the effects of rescattering on unpolarized differential and total cross sections as well as on various polarization observables. For the elementary $\gamma N \rightarrow \pi^0 N$ amplitude, the realistic unitary isobar model MAID2007 [30] has been used. The deuteron wave function used in our computation is obtained from the realistic high-precision CD-Bonn potential [38]. As for the deuteron amplitude, we have considered in addition to the pure IA also the two-step process with πN - and ηN -rescattering and all terms in the multiple scattering series within a three-body model. For the hadronic and electromagnetic two-body amplitudes taken into account in the calculation of the rescattering diagrams, only the $S_{11}(1535)$ -resonance was considered in the π - and η -exchange contributions. The three-body problem for the intermediate ηNN system was solved only for the lowest s -wave three-body configuration 1S_0 ($J^\pi = 0^-$; $T = 1$). The π - and η -photoproduction reactions on the nucleon as well as their interactions with nucleons were assumed to be proceed exclusively via the extraction of

the $S_{11}(1535)$ -resonance.

We have presented results for the unpolarized differential and total cross sections, all beam, target, and beam-target spin asymmetries corresponding to polarized photons and/or oriented deuterons, the helicity-dependent differential and total cross sections, the helicity E -asymmetry, and the deuteron GDH integral. The sensitivity of our results to the elementary $\gamma N \rightarrow \pi^0 N$ amplitude and the deuteron wave function is investigated. In addition, we have compared our predictions with the available experimental data and other theoretical models. Our main conclusions are as follows.

In general, the strongest influence of rescattering effects appears at extreme backward pion angles in the photon energy range $E_\gamma \simeq 600$ -800 MeV. We found that already in the IA a shoulder appears in the differential cross section at photon lab-energy slightly above $E_\gamma=700$ MeV. The inclusion of rescattering effects shifts the peak position to lower energies and make it more pronounced. Our calculations showed also that the differential cross section is influenced by the inclusion of rescattering effects. The interference of the pure IA and complete three-body calculation has been found very important. Thus, we conclude that the three-body problem of the ηNN system is of special importance for understanding the reaction dynamics. The total cross section is found to be much less affected by rescattering contributions. We also found that most of spin asymmetries of the differential cross section are sensitive to the inclusion of rescattering effects. Some asymmetries, in particular T_{21} , T_{11}^c , T_{21}^c , T_{22}^c , T_{10}^l , and $T_{2\pm 2}^l$, seem to provide a signature of the TBM contribution at photon energies 600-800 MeV and extreme backward direction. Indeed, our calculations show that a broad enhancement (with the width of the order of 100 MeV) appears in the energy behavior of the spin asymmetries at backward pion angles in the η -threshold region. This enhancement becomes more pronounced as pion angles increases. On the contrary, the spin asymmetries of the total cross section are found to be much less affected by rescattering contributions. The influence of FOR and TBM effects is quite marginal although not negligible.

The results of the helicity-dependent differential cross sections for parallel and antiparallel spins of photon and deuteron as well as their difference are found to be sensitive to rescattering effects. A quite strong dependence of their results on the intermediate ηNN three-body calculation is found, especially at photon energies between 600 and 800 MeV at extreme backward direction. As may be expected, the role of rescattering effects in the $\gamma d \rightarrow \pi^0 d$ reaction in the energy region considered in this work is rather unimportant for the helicity-dependent total cross sections and their difference. This conclusion is also valid for the corresponding GDH integral for the deuteron, where the curves represent the different rescattering contributions are found to be indistinguishable. We also considered the role of rescattering effects on the helicity E -asymmetry. As our calculation shows, the E -

asymmetry is much more sensitive to rescattering effects at extreme backward pion angles. Within our model, we also evaluated the contribution of the $\vec{\gamma} \vec{d} \rightarrow \pi^0 d$ reaction to the GDH integral for the deuteron integrated up to 900 MeV. A values of $I_{IA+FOR+TBM}^{GDH}(900MeV) = 61.36 \mu\text{b}$ is obtained. The sensitivity of the obtained results for the deuteron GDH integral to the choice of NN potential model used for the deuteron wave function is investigated and a large dependence is found.

We have also studied the influence of the elementary $\gamma N \rightarrow \pi N$ amplitude and the deuteron wave function on the differential cross section and polarization observables. Calculations showed that these observables are sensitive to the choice of both the elementary amplitude and the deuteron wave function than to the rescattering effects. In many cases the deviation among results obtained using different elementary amplitudes and various deuteron wave functions is very large. Indeed, we have shown that updating the unitary isobar MAID2003 model [29] to MAID2007 [30] produces differences that may be as large as 30% at extreme backward pion angles and higher energies. And the use of CD-Bonn NN potential [38] for deuteron wave function doubles the differential cross section in this kinematic region. Thus, the process $\gamma d \rightarrow \pi^0 d$ can serve as a filter for different elementary amplitudes and various deuteron wave functions since its predictions for differential cross section and spin asymmetries show very different values when one varies the elementary amplitudes and/or the deuteron wave functions employed.

In comparison with the experimental data from [3, 4, 21] for the differential cross section and from YerPhi Collaboration [5] for the linear photon asymmetry at pion angle of 130° , major discrepancies are found, specially at extremely backward pion angles. It was shown that the inclusion of a full three-body calculation can in no way resolve the discrepancy between the experimental data and theoretical prediction. We have also compared our results for the linear photon asymmetry at pion angle of 130° with with the old predictions of Imanishi *et al.* [53] and significant differences are also found.

As already mentioned in the previous section, a possible source for the existing differences between our predictions for $d\sigma/d\Omega$, Σ , and T_{2M} ($M = 0, 1, 2$) and the experimental data could be the neglected effects from two-nucleon mechanisms in the photoproduction amplitude, e.g. meson-exchange current, isobar configuration in the deuteron wave function, etc, and other resonance amplitudes besides the $S_{11}(1535)$ contribution. One might expect that these influence maybe particularly important for the theoretical description of spin asymmetries. For example, meson-exchange currents were found to be quite significant for π^+ -photoproduction on ^3He in Ref. [56]. It is also clear that the πN elastic scattering cross sections are much larger than the $\pi N \rightarrow \eta N$ cross sections, and $N(1520)\frac{3}{2}^-$ also strongly couples to the πN channel in the considered energy region. Therefore, the two-step processes including $N(1520)\frac{3}{2}^-$ and the three-body πNN

processes are expected to have comparable contribution like $N(1535)\frac{1}{2}^-$ and three-body ηNN processes. Indeed, we cannot assert that the suggested effects are sufficient to explain the features of the entire set of available data. If such effects are really quite important, their inclusion would tend to diminish the relative size of the $d\sigma/d\Omega$ peak and its manifestation. In this case, we will have to face again the same question about the origin of the cusp structure observed in the differential cross section at backward pion angles near the threshold of η -production. Additional significant contributions to the GDH integral from the double-pion production channels can be expected. Such contributions for the $\gamma d \rightarrow \pi\pi NN$ reaction with NN -FSI have been explicitly evaluated in [51] up to 2.2 GeV and a value of $I_{\gamma d \rightarrow \pi\pi NN}^{GDH}(2.2 \text{ GeV})=159.34 \mu\text{b}$ was obtained.

In order to draw further conclusions, it would be very desirable to have more precise experiments for spin asymmetries of the $\gamma d \rightarrow \pi^0 d$ reaction around the η -threshold region at backward direction. This clearly poses a more detailed test of the underlying model. Therefore, there is a way for further improvements of the present model.

Acknowledgments

I am gratefully acknowledge very useful discussions with N. Akopov, S. Al-Thoyaib, and A. Hemmdan. I am deeply indebted to D. M. Nikolenko, I. A. Rachek, M. I. Levchuk, and V. V. Gauzshtein for useful discussions and supplying us with the recent experimental data.

APPENDIX A: EXPLICIT EXPRESSIONS FOR UNPOLARIZED DIFFERENTIAL CROSS SECTION AND VARIOUS SPIN ASYMMETRIES

Here, we list the explicit expressions for the unpolarized differential cross section and the various spin asymmetries in terms of the reduced t -matrix elements [22]:

(i) The unpolarized differential cross section

$$\frac{d\sigma_0}{d\Omega} = \frac{\mathcal{K}}{3} \sum_{m'_d m_d} |t_{m'_d 1 m_d}|^2. \quad (\text{A1})$$

(ii) The photon spin asymmetry for linearly polarized photons and unpolarized deuterons

$$\Sigma \frac{d\sigma_0}{d\Omega} = -\frac{\mathcal{K}}{3} \sum_{m'_d m_d} t_{m'_d 1 m_d}^* t_{m'_d -1 m_d}. \quad (\text{A2})$$

(iii) The target spin asymmetry for vector polarized deuterons and unpolarized photons

$$T_{11} \frac{d\sigma_0}{d\Omega} = \sqrt{\frac{2}{3}} \mathcal{K} \Im m \sum_{m_d} (t_{m_d 1 -1}^* t_{m_d 10} + t_{m_d 10}^* t_{m_d 11}). \quad (\text{A3})$$

(iv) The target spin asymmetries for tensor polarized deuterons and unpolarized photons

$$T_{20} \frac{d\sigma_0}{d\Omega} = \frac{\mathcal{K}}{3\sqrt{2}} \sum_{m_d} (|t_{m_d 11}|^2 + |t_{m_d 1-1}|^2 - 2|t_{m_d 10}|^2), \quad (\text{A4})$$

$$T_{21} \frac{d\sigma_0}{d\Omega} = \sqrt{\frac{2}{3}} \mathcal{K} \Re e \sum_{m_d} (t_{m_d 1-1}^* t_{m_d 10} - t_{m_d 10}^* t_{m_d 11}), \quad (\text{A5})$$

$$T_{22} \frac{d\sigma_0}{d\Omega} = \frac{2\mathcal{K}}{\sqrt{3}} \Re e \sum_{m_d} t_{m_d 1-1}^* t_{m_d 11}. \quad (\text{A6})$$

(v) The beam-target spin asymmetries for circularly polarized photons and vector polarized deuterons

$$T_{10}^c \frac{d\sigma_0}{d\Omega} = \frac{\mathcal{K}}{\sqrt{6}} \sum_{m_d} (|t_{m_d 11}|^2 - |t_{m_d 1-1}|^2), \quad (\text{A7})$$

$$T_{11}^c \frac{d\sigma_0}{d\Omega} = -\sqrt{\frac{2}{3}} \mathcal{K} \Re e \sum_{m_d} (t_{m_d 1-1}^* t_{m_d 10} + t_{m_d 10}^* t_{m_d 11}). \quad (\text{A8})$$

(vi) The beam-target spin asymmetries for circularly polarized photons and tensor polarized deuterons

$$T_{21}^c \frac{d\sigma_0}{d\Omega} = \sqrt{\frac{2}{3}} \mathcal{K} \Im m \sum_{m_d} (t_{m_d 10}^* t_{m_d 11} - t_{m_d 1-1}^* t_{m_d 10}), \quad (\text{A9})$$

$$T_{22}^c \frac{d\sigma_0}{d\Omega} = -\frac{2\mathcal{K}}{\sqrt{3}} \Im m \sum_{m_d} t_{m_d 1-1}^* t_{m_d 11}. \quad (\text{A10})$$

(vii) The beam-target spin asymmetries for linearly polarized photons and vector polarized deuterons

$$T_{10}^l \frac{d\sigma_0}{d\Omega} = \sqrt{\frac{2}{3}} \mathcal{K} \Im m \sum_{m_d} t_{m_d 11}^* t_{m_d -11}, \quad (\text{A11})$$

$$T_{11}^l \frac{d\sigma_0}{d\Omega} = -\sqrt{\frac{2}{3}} \mathcal{K} \Im m \sum_{m_d} t_{m_d 1-1}^* t_{m_d -10}, \quad (\text{A12})$$

$$T_{1-1}^l \frac{d\sigma_0}{d\Omega} = \sqrt{\frac{2}{3}} \mathcal{K} \Im m \sum_{m_d} t_{m_d 11}^* t_{m_d -10}. \quad (\text{A13})$$

(viii) The beam-target spin asymmetries for linearly polarized photons and tensor polarized deuterons

$$T_{20}^l \frac{d\sigma_0}{d\Omega} = \frac{\sqrt{2}}{3} \mathcal{K} \Re e \sum_{m_d} (t_{m_d 10}^* t_{m_d -10} - t_{m_d 11}^* t_{m_d -11}), \quad (\text{A14})$$

$$T_{21}^l \frac{d\sigma_0}{d\Omega} = \sqrt{\frac{2}{3}} \mathcal{K} \Re e \sum_{m_d} t_{m_d 10}^* t_{m_d -11}, \quad (\text{A15})$$

$$T_{2-1}^l \frac{d\sigma_0}{d\Omega} = \sqrt{\frac{2}{3}} \mathcal{K} \Re e \sum_{m_d} t_{m_d 10}^* t_{m_d -1-1}, \quad (\text{A16})$$

$$T_{22}^l \frac{d\sigma_0}{d\Omega} = -\frac{\mathcal{K}}{\sqrt{3}} \sum_{m_d} t_{m_d 1-1}^* t_{m_d -11}, \quad (\text{A17})$$

$$T_{2-2}^l \frac{d\sigma_0}{d\Omega} = -\frac{\mathcal{K}}{\sqrt{3}} \sum_{m_d} t_{m_d 11}^* t_{m_d -1-1}. \quad (\text{A18})$$

APPENDIX B: AN ELEMENTARY PION PHOTOPRODUCTION OPERATOR

The invariant amplitude for pion photoproduction from the nucleon

$$\gamma(E_\gamma, \vec{q}, \vec{\epsilon}_\lambda) + N(E_N, \vec{p}) \rightarrow \pi(E_\pi, \vec{k}) + N'(E'_N, \vec{p}'), (\text{B1})$$

can be written as [39]

$$T_{\gamma N \rightarrow \pi N'} = \bar{u}(p') \left[\sum_{i=1}^4 A_i(s, u, t) \Gamma_i \right] u(p), \quad (\text{B2})$$

where

$$\begin{aligned} s &= (q+p)^2 = (k+p')^2, \\ u &= (q-p')^2 = (k-p)^2, \\ t &= (q-k)^2 = (p-p')^2, \end{aligned} \quad (\text{B3})$$

and

$$\begin{aligned} \Gamma_1 &= i\gamma_5 \not{q}, \\ \Gamma_2 &= i\gamma_5 [k \cdot \epsilon (p+p') \cdot q - k \cdot q (p+p') \cdot \epsilon], \\ \Gamma_3 &= i\gamma_5 (k \cdot q \not{\epsilon} - k \cdot \epsilon \not{q}), \\ \Gamma_4 &= \epsilon_{\mu\nu\rho\sigma} \gamma^\mu k^\nu \epsilon^\rho q^\sigma. \end{aligned} \quad (\text{B4})$$

The matrix γ_5 and antisymmetric tensor $\epsilon_{\mu\nu\rho\sigma}$ are fixed according to the conditions

$$\gamma_5 = + \begin{pmatrix} 0 & 1 \\ 1 & 0 \end{pmatrix} \quad \text{and} \quad \epsilon_{0123} = +1. \quad (\text{B5})$$

In the spinor form, the matrix T reads

$$\langle m_2 | T | \lambda m_1 \rangle = \langle m_2 | \mathcal{L} + i\vec{\sigma} \cdot \vec{K} | \lambda m_1 \rangle. \quad (\text{B6})$$

Contributions of the amplitudes A_i to the matrix T (B6) in an arbitrary frame are as follows

$$\mathcal{L}_1 = NN' \left[-\frac{\vec{p} \cdot \vec{S}}{E_+} + \frac{\vec{p}' \cdot \vec{S}}{E'_+} + E_\gamma \frac{\vec{\epsilon} \cdot \vec{C}}{E_+ E'_+} \right] A_1, \quad (\text{B7})$$

$$\begin{aligned} \vec{K}_1 &= NN' \left[\vec{\epsilon} \left(E_\gamma + E_\gamma \frac{\vec{p} \cdot \vec{p}'}{E_+ E'_+} - \frac{\vec{p} \cdot \vec{q}}{E_+} - \frac{\vec{p}' \cdot \vec{q}}{E'_+} \right) \right. \\ &\quad \left. + \vec{q} \left(\frac{\vec{p} \cdot \vec{\epsilon}}{E_+} + \frac{\vec{p}' \cdot \vec{\epsilon}}{E'_+} \right) - \vec{p} E_\gamma \frac{\vec{p}' \cdot \vec{\epsilon}}{E_+ E'_+} \right. \\ &\quad \left. - \vec{p}' E_\gamma \frac{\vec{p} \cdot \vec{\epsilon}}{E_+ E'_+} \right] A_1, \end{aligned} \quad (\text{B8})$$

$$\mathcal{L}_2 = 0, \quad (\text{B9})$$

$$\vec{K}_2 = 2NN' (\vec{\epsilon} \cdot \vec{p}' p \cdot q - \vec{\epsilon} \cdot \vec{p} p' \cdot q) \left(\frac{\vec{p}}{E_+} - \frac{\vec{p}'}{E'_+} \right) A_2, \quad (\text{B10})$$

$$\mathcal{L}_3 = -NN' \frac{1}{E_+ E'_+} [\vec{k} \cdot \vec{\epsilon} \vec{q} \cdot \vec{C} + k \cdot q \vec{\epsilon} \cdot \vec{C}] A_3, \quad (\text{B11})$$

$$\begin{aligned} \vec{K}_3 &= NN' \left\{ \left(1 - \frac{\vec{p} \cdot \vec{p}'}{E_+ E'_+} \right) (\vec{\epsilon} k \cdot q + \vec{q} \vec{k} \cdot \vec{\epsilon}) \right. \\ &\quad \left. + \vec{p} \left[\left(-\frac{E_\gamma}{E_+} + \frac{\vec{p}' \cdot \vec{q}}{E_+ E'_+} \right) \vec{k} \cdot \vec{\epsilon} + \frac{\vec{p}' \cdot \vec{\epsilon} k \cdot q}{E_+ E'_+} \right] \right. \\ &\quad \left. + \vec{p}' \left[\left(-\frac{E_\gamma}{E'_+} + \frac{\vec{p} \cdot \vec{q}}{E_+ E'_+} \right) \vec{k} \cdot \vec{\epsilon} + \frac{\vec{p} \cdot \vec{\epsilon} k \cdot q}{E_+ E'_+} \right] \right\} A_3, \end{aligned} \quad (\text{B12})$$

$$\begin{aligned} \mathcal{L}_4 &= NN' \frac{1}{E_+ E'_+} \left[-\vec{\epsilon} \cdot \vec{C} E_\gamma (E_+ + E'_+) \right. \\ &\quad \left. + \vec{p} \cdot \vec{S} (E_+^2 + \vec{p} \cdot \vec{p}') \right. \\ &\quad \left. - \vec{p}' \cdot \vec{S} (E_+^2 + \vec{p} \cdot \vec{p}') \right] A_4, \end{aligned} \quad (\text{B13})$$

$$\begin{aligned} \vec{K}_4 &= NN' \left\{ -\vec{\epsilon} \left[k^0 \left(\frac{\vec{p} \cdot \vec{q}}{E_+} - \frac{\vec{p}' \cdot \vec{q}}{E'_+} \right) \right. \right. \\ &\quad \left. \left. - E_\gamma \left(\frac{\vec{p} \cdot \vec{k}}{E_+} - \frac{\vec{p}' \cdot \vec{k}}{E'_+} \right) + \frac{\vec{p}' \cdot \vec{q} \vec{k} \cdot \vec{p} - \vec{p} \cdot \vec{q} \vec{k} \cdot \vec{p}'}{E_+ E'_+} \right] \right. \\ &\quad \left. + \vec{q} \left[k^0 \left(\frac{\vec{p} \cdot \vec{\epsilon}}{E_+} - \frac{\vec{p}' \cdot \vec{\epsilon}}{E'_+} \right) - \frac{\vec{\epsilon} \cdot \vec{p} \vec{k} \cdot \vec{p}' - \vec{\epsilon} \cdot \vec{p}' \vec{k} \cdot \vec{p}}{E_+ E'_+} \right] \right. \\ &\quad \left. - \vec{k} \left[E_\gamma \left(\frac{\vec{p} \cdot \vec{\epsilon}}{E_+} - \frac{\vec{p}' \cdot \vec{\epsilon}}{E'_+} \right) + \frac{\vec{C} \cdot \vec{S}}{E_+ E'_+} \right] \right\} A_4, \end{aligned} \quad (\text{B14})$$

where $\vec{S} = \vec{q} \times \vec{\epsilon}$, $\vec{C} = \vec{p} \times \vec{p}'$, $E_\pm = E \pm M_N$, $E'_\pm = E' \pm M_N$, $N = \sqrt{E_+ / 2M_N}$, and $N' = \sqrt{E'_+ / 2M_N}$.

The photoproduction operator in the c.m. frame has the well-known form [40]

$$\begin{aligned} \langle m_2 | T_{\gamma N \rightarrow \pi N}^* | \lambda m_1 \rangle = & \frac{4\pi W_{\gamma N}}{M_N} \langle m_2 | i\vec{\sigma} \cdot \vec{\epsilon}_\lambda^* F_1 \\ & + \vec{\sigma} \cdot \hat{k}^* \vec{\sigma} \cdot (\hat{q}^* \times \vec{\epsilon}_\lambda^*) F_2 \\ & + i\vec{\sigma} \cdot \hat{q}^* \hat{k}^* \cdot \vec{\epsilon}_\lambda^* F_3 \\ & + i\vec{\sigma} \cdot \hat{k}^* \hat{k}^* \cdot \vec{\epsilon}_\lambda^* F_4 | m_1 \rangle, \end{aligned} \quad (\text{B15})$$

where $W_{\gamma N} = \sqrt{s}$ and the superscript asterisk is used for the corresponding quantities in the γN c.m. frame. A comparison of the above \mathcal{L}_i and K_i equations in the c.m. frame with Eq. (B15) gives the following relation between the amplitudes A_i and F_i

$$\begin{pmatrix} A_1 \\ A_2 \\ A_3 \\ A_4 \end{pmatrix} = \frac{4\pi}{k^* E_\gamma^*} \begin{pmatrix} W_+ & -W_- & -2M_N \frac{k \cdot q}{W_-} & -2M_N \frac{k \cdot q}{W_+} \\ 0 & 0 & 1 & -1 \\ 1 & 1 & \frac{W_- W_+ - k \cdot q}{W_-} & \frac{W_- W_+ - k \cdot q}{W_+} \\ 1 & 1 & -\frac{k \cdot q}{W_-} & -\frac{k \cdot q}{W_+} \end{pmatrix} \times \begin{pmatrix} \sqrt{\frac{E_- E'_-}{E_+ E'_+}} \frac{1}{W_-} F_1 \\ \sqrt{\frac{E_+ E'_+}{E_- E'_-}} \frac{1}{W_+} F_2 \\ \sqrt{\frac{E_+}{E'_+}} \frac{1}{W_+} F_3 \\ \sqrt{\frac{E_-}{E'_-}} \frac{1}{W_-} F_4 \end{pmatrix}. \quad (\text{B16})$$

where $W_\pm = W_{\gamma N} \pm M_N$. One should emphasize that all variables in Eq. (B16) are taken in the c.m. frame, in particular

$$E_\gamma^* = \frac{s - M_N^2}{2\sqrt{s}} = \frac{W_+ W_-}{2W_{\gamma N}} = \sqrt{E_+ E_-}, \quad (\text{B17})$$

$$\begin{aligned} k^* &= \frac{\sqrt{[W_{\gamma N}^2 - (M_N + m_\pi)^2][W_{\gamma N}^2 - (M_N - m_\pi)^2]}}{2W_{\gamma N}} \\ &= \sqrt{E_+ E'_-}. \end{aligned} \quad (\text{B18})$$

APPENDIX C: THREE-BODY TREATMENT OF THE ηNN INTERACTION

In this appendix we briefly review the basic features of three-body techniques for the application to the full dynamics in the intermediate ηNN three-body system [41]. The ηNN system consists of two nucleons, N_1 and N_2 , and an η -meson, which will be denoted as particle 1, 2 and 3, respectively. In the c.m. frame the basic free particle states $|\vec{p}_i, \vec{q}_i\rangle$ will be characterized as usual by a pair of vectors \vec{p}_i and \vec{q}_i , where \vec{p}_i is the relative momentum of a (jk) pair ($j \neq i \neq k$) and \vec{q}_i denotes

the relative momentum of the unpaired particle i with respect to the c.m. frame of the pair (jk) .

In order to approximate the three-body equations in such a way that they become practically solvable, it is customary to introduce a separable ansatz for each two-body interaction. In our case this approximation has also a physical motivation because of the strong dominance of the s -wave pole terms in the low-energy ηN - and NN -scattering matrices. Thus, we will assume that the two-body driving forces can be approximated by rank-one separable potentials, which, when regarded as operators in the three-body Hilbert space, have the form

$$v_i = \gamma_i \int \frac{d^3 q}{(2\pi)^3} |i, \vec{q}\rangle \langle i, \vec{q}|, \quad (\text{C1})$$

with i being the channel index. In detail one has

$$|i, \vec{q}\rangle = \begin{cases} |N_1(\vec{q}), (N_2\eta)\rangle & \text{for } i = 1, \\ |N_2(\vec{q}), (N_1\eta)\rangle & \text{for } i = 2, \\ |\eta(\vec{q}), (N_1 N_2)\rangle & \text{for } i = 3. \end{cases} \quad (\text{C2})$$

Here the ket $|i, \vec{q}\rangle = |i\rangle \otimes |\vec{q}\rangle$ is defined such that

$$\langle \vec{p}', \vec{q}' | i, \vec{q}' \rangle = \langle \vec{p}' | i \rangle \langle \vec{q}' | \vec{q}' \rangle = (2\pi)^3 \epsilon_i(\vec{q}) \delta(\vec{q} - \vec{q}') f_i(\vec{p}') \quad (\text{C3})$$

with

$$\epsilon_i(\vec{q}) = \begin{cases} 2E_i(\vec{q}) & \text{for } i = 3, \\ \frac{E_i(\vec{q})}{M_N} & \text{for } i = 1, 2, \end{cases} \quad (\text{C4})$$

where $f_i(\vec{p}') = \langle \vec{p}' | i \rangle$ is the usual vertex function of the separable representation. For $i = 3$ the Pauli principle for the nucleons is already incorporated, i.e., $P_{12}|3, \vec{q}\rangle = -|3, \vec{q}\rangle$, where P_{12} is the nucleon exchange operator.

The asymptotic channel wave function, describing the free motion of a particle “ i ” with momentum \vec{q} relative to the interacting pair (jk) , is given by

$$|\phi_i(W, \vec{q})\rangle = G_{\eta NN}(W) |i, \vec{q}\rangle, \quad (\text{C5})$$

where $G_{\eta NN}(W)$ is the free ηNN Green's function depending on the total three-body energy W . For the moment being we drop spin-isospin indices. Then, expressing the separable ηN - and NN -scattering matrices, acting in three-particle space, in terms of the two-body matrix elements, we find

$$\begin{aligned} \langle \vec{p}', \vec{q}' | t_i(W) | \vec{p}, \vec{q} \rangle &= (2\pi)^3 \delta(\vec{q}' - \vec{q}) \langle \vec{p}' | t_i(W_i(W, \vec{q})) | \vec{p} \rangle \\ &= (2\pi)^3 \delta(\vec{q}' - \vec{q}) f_i^*(\vec{p}') \\ &\quad \times \tau_i(W_i(W, \vec{q})) f_i(\vec{p}), \end{aligned} \quad (\text{C6})$$

where the propagator of a pair (jk) in the presence of a spectator “ i ” reads

$$\begin{aligned} \tau_i(W_i) &= \left[\frac{1}{\gamma_i} - \frac{1}{(2\pi)^3} \int \frac{d^3 p}{\epsilon_j(\vec{p}) \epsilon_k(\vec{p})} \right. \\ &\quad \left. \times \frac{|f_i(\vec{p})|^2}{W_i - E_j(\vec{p}) - E_k(\vec{p}) + i\epsilon} \right]^{-1}. \end{aligned} \quad (\text{C7})$$

Here $W_i(W, \vec{q})$ denotes the invariant mass of the subsystem (j, k) , defined by putting the spectator particle “ i ” on mass shell, i.e.,

$$W_i(W, \vec{q}) = \sqrt{W^2 - 2W E_i(\vec{q}) + M_i^2}. \quad (\text{C8})$$

For the particle energies we use the relativistic expressions $E_i(\vec{p}) = \sqrt{p^2 + M_i^2}$. The separable ansatz leads to a system of coupled equations of the familiar Lippman-Schwinger form [58]

$$\begin{aligned} X_{ij}(W, \vec{q}', \vec{q}) &= Z_{ij}(W, \vec{q}', \vec{q}) \\ &+ \sum_{k=1}^3 \int \frac{d^3 q''}{(2\pi)^3 \epsilon_k(q'')} Z_{ik}(W, \vec{q}', \vec{q}'') \\ &\times \tau_k(W_k(W, \vec{q}'')) X_{kj}(W, \vec{q}'', \vec{q}). \end{aligned} \quad (\text{C9})$$

The amplitudes $X_{ij}(W)$ define the transitions between the channel states (C2), i.e. collisions of the type “ $j + (ik) \rightarrow i + (jk)$ ”, where (ik) and (jk) refer to interacting two-particle states. The driving terms $Z_{ij}(W)$ are represented by the matrix elements of the free ηNN Green's function

$$Z_{ij}(W, \vec{q}', \vec{q}) = (1 - \delta_{ij}) \langle i, \vec{q}' | G_{\eta NN}(W) | j, \vec{q} \rangle. \quad (\text{C10})$$

Explicitly, one finds for $i \neq j$

$$Z_{ij}(W, \vec{q}', \vec{q}) = \frac{f_i^*(\vec{p}_i(\vec{q}', \vec{q})) f_j(\vec{p}_j(\vec{q}', \vec{q}))}{W - E_i(\vec{q}') - E_j(\vec{q}) - E_k(\vec{q}' + \vec{q}) + i\epsilon}, \quad (\text{C11})$$

where the momenta $\vec{p}_i(\vec{q}', \vec{q})$ and $\vec{p}_j(\vec{q}', \vec{q})$ are given in terms of \vec{q}' and \vec{q} . For simplicity, we use the nonrelativistic relations

$$\vec{p}_i(\vec{q}', \vec{q}) = \vec{q} + \frac{\mu_i}{M_k} \vec{q}' \quad \text{and} \quad \vec{p}_j(\vec{q}', \vec{q}) = \vec{q}' + \frac{\mu_j}{M_k} \vec{q}, \quad (\text{C12})$$

where the reduced mass in i th channel reads

$$\mu_i = \frac{M_j M_k}{M_j + M_k}. \quad (\text{C13})$$

The next step to be taken towards an explicit evaluation of the three-body equations is the antisymmetrization of the basic amplitudes with respect to the exchange of the nucleons N_1 and N_2 for which we follow mainly the work of [59]. It affects only the channels $i = 1$ and $i = 2$ because the channel $i = 3$ is already antisymmetric by construction as pointed out above. Consider the system of equations, which couple the amplitudes X_{ij} for the possible transitions from the channel $j = 3$. In the operator form we have explicitly

$$\begin{aligned} X_{13} &= Z_{13} + Z_{12} \tau_2 X_{23} + Z_{13} \tau_3 X_{33}, \\ X_{23} &= Z_{23} + Z_{21} \tau_1 X_{13} + Z_{23} \tau_3 X_{33}, \\ X_{33} &= Z_{31} \tau_1 X_{13} + Z_{32} \tau_2 X_{23}. \end{aligned} \quad (\text{C14})$$

Taking into account the identity of the nucleons, it is easy to find the following relations [59]

$$\tau_1 = \tau_2, \quad Z_{13} = -Z_{23}, \quad Z_{31} = -Z_{32}, \quad \text{and} \quad Z_{12} = Z_{21}. \quad (\text{C15})$$

With the help of this symmetry one can reduce (C14) to a system of only two coupled equations

$$\begin{aligned} (X_{13} - X_{23}) &= 2Z_{13} - Z_{12} \tau_2 (X_{13} - X_{23}) \\ &+ 2Z_{13} \tau_3 X_{33}, \end{aligned} \quad (\text{C16})$$

$$X_{33} = Z_{31} \tau_1 (X_{13} - X_{23}). \quad (\text{C17})$$

Before defining the explicitly antisymmetrized amplitudes, it is convenient to introduce a new channel notation. From now on we denote the channel with a spectator nucleon as “ N^* ” and the one with a spectator meson as “ d ”. The corresponding channel wave functions $|N^*, \vec{q}\rangle$ and $|d, \vec{q}\rangle$ are assumed to be antisymmetrized with respect to the nucleons, in detail

$$|N^*, \vec{q}\rangle = \frac{1}{\sqrt{2}} (|1, \vec{q}\rangle - |2, \vec{q}\rangle) \quad \text{and} \quad |d, \vec{q}\rangle = |3, \vec{q}\rangle. \quad (\text{C18})$$

Defining the driving terms in a symbolic notation by

$$\begin{aligned} Z_{N^*N^*} &= -\frac{1}{2}(Z_{12} + Z_{21}) = -Z_{12}, \\ Z_{dN^*} &= Z_{31}, \quad \text{and} \\ Z_{N^*d} &= Z_{13}, \end{aligned} \quad (\text{C19})$$

and the properly antisymmetrized amplitudes by

$$X_d = X_{33}, \quad X_{N^*d} = \frac{1}{2}(X_{13} - X_{23}), \quad (\text{C20})$$

one arrives at the following set of equations:

$$\begin{aligned} X_{N^*d} &= Z_{N^*d} + Z_{N^*d} \tau_d X_d \\ &+ Z_{N^*N^*} \tau_{N^*} X_{N^*d}, \end{aligned} \quad (\text{C21})$$

$$X_d = 2 Z_{dN^*} \tau_{N^*} X_{N^*d}, \quad (\text{C22})$$

where the amplitudes X_d and X_{N^*d} describe the two different transitions $\eta d \rightarrow \eta d$ and $\eta d \rightarrow N^* N$, respectively, which are realized in ηd scattering.

Now, we will consider in addition the coupling to the πNN channel via the two-body reaction $\eta N \rightarrow \pi N$, whereas we will neglect the coupling to the two-pion channel $\pi\pi NN$. Its inclusion into the three-body formalism would require the use of phenomenological approaches, which in any case seem to be very ambiguous. Due to the smallness of the $N^* \rightarrow \pi\pi N$ decay probability we believe that this neglect will not significantly influence our results. A treatment of the resulting coupled channel problem within the Faddeev approach was developed, e.g., in [60, 61]. Accordingly, we extend the channel $|N^*\rangle$ to the following two-component form:

$$|N^*\rangle = \begin{pmatrix} |N^*(\eta)\rangle \\ |N^*(\pi)\rangle \end{pmatrix}. \quad (\text{C23})$$

The corresponding coupled channel t -matrix is given by

$$t_{N^*} = |N^*\rangle \tau_{N^*} \langle N^*|, \quad (\text{C24})$$

with the N^* -propagator

$$\tau_{N^*}(W_{N^*}) = \left[\frac{1}{\gamma_{N^*}} - \frac{1}{(2\pi)^3} \sum_{\alpha \in \{\pi, \eta\}} \int \frac{M_N}{2E_\alpha(\vec{p})E_N(\vec{p})} \times \frac{|f_{N^*}^{(\alpha)}(\vec{p})|^2}{W_{N^*} - E_N(\vec{p}) - E_\alpha(\vec{p}) + i\epsilon} d^3p \right]^{-1}, \quad (\text{C25})$$

where $f_{N^*}^{(\alpha)}(\vec{p}) = \langle \vec{p} | N^*(\alpha) \rangle$. Turning now to the three-body problem, we obtain a set of three coupled equations, namely

$$X_{N^*d} = Z_{N^*d}^{(\eta)} + Z_{N^*d}^{(\eta)} \tau_d^{(\eta)} X_d^{(\eta)} + Z_{N^*d}^{(\pi)} \tau_d^{(\pi)} X_d^{(\pi)} + (Z_{N^*N^*}^{(\eta)} + Z_{N^*N^*}^{(\pi)}) \tau_{N^*} X_{N^*d}, \quad (\text{C26})$$

$$X_d^{(\eta)} = 2 Z_{dN^*}^{(\eta)} \tau_{N^*} X_{N^*d}, \quad (\text{C27})$$

$$X_d^{(\pi)} = 2 Z_{dN^*}^{(\pi)} \tau_{N^*} X_{N^*d}, \quad (\text{C28})$$

where the driving terms are given in analogy to (C19) for $\alpha \in \{\pi, \eta\}$ by

$$\begin{aligned} Z_{N^*N^*}^{(\alpha)} &= -\frac{1}{2}(Z_{12}^{(\alpha)} + Z_{21}^{(\alpha)}), \\ Z_{dN^*}^{(\alpha)} &= Z_{31}^{(\alpha)} \quad \text{and} \\ Z_{N^*d}^{(\alpha)} &= Z_{13}^{(\alpha)}, \end{aligned} \quad (\text{C29})$$

with analogous definitions for $Z_{ij}^{(\alpha)}$ as in (C10), i.e.,

$$Z_{ij}^{(\alpha)}(W, \vec{q}', \vec{q}) = (1 - \delta_{ij}) \langle i, \vec{q}' | G_{\alpha NN}(W) | j, \vec{q} \rangle. \quad (\text{C30})$$

The set of equations (C26) through (C28) is the formal basis of the present calculation. Its solution gives the required symmetrized rearrangement amplitudes and thus amounts to solving the ηNN -problem.

-
- [1] B. Krusche and S. Schadmand, Prog. Part. Nucl. Phys. **51**, 399 (2003); V. Burkert and T.-S.H. Lee, Int. J. Mod. Phys. E **13**, 1035 (2004); A. Thomas, Eur. Phys. J. A **28**, Suppl. 1, 161 (2006); K. Helbing, Prog. Part. Nucl. Phys. **57**, 405 (2006); A.M. Sandorfi *et al.*, AIP Conf. Proc. **1155**, 71 (2009); H.R. Weller *et al.*, Prog. Part. Nucl. Phys. **62**, 275 (2009); B. Krusche, Eur. Phys. J. Special Topics **198**, 199 (2011); I. Jaegle *et al.*, Eur. Phys. J. A **47**, 89 (2011).
- [2] R.A. Arndt, W.J. Briscoe, I.I. Strakovsky, and R.L. Workman, Phys. Rev. C **66**, 055213 (2002) [SAID database: <http://gwdac.phys.gwu.edu>].
- [3] Y. Ilieva (for the CLAS Collaboration), presented at 17th International IUPAP Conference on Few-Body Problems in Physics (FB17), JLAB-PHY-03-47; Y. Ilieva (for the CLAS Collaboration), nucl-ex/03090177; Y. Ilieva, CLAS-NOTE 2007-006, <http://www1.jlab.org/ul/Physics/Hall-B/clas/index.cfm>.
- [4] Y. Ilieva, B.L. Berman, A. E. Kudryavtsev, I.I. Strakovsky, and V.E. Tarasov (for the CLAS Collaboration), Eur. Phys. J. A **43**, 261 (2010).
- [5] F.V. Adamian *et al.*, Phys. Lett. B **232**, 296 (1989); F.V. Adamian *et al.*, Czech. J. Phys. B **36**, 945 (1986); F.V. Adamian *et al.*, JETP Lett. **39**, 710 (1984).
- [6] I.A. Rachek *et al.*, Phys. Rev. Lett. **98**, 182303 (2007); D.M. Nikolenko *et al.*, JETP Lett. **89**, 432 (2009); D.M. Nikolenko *et al.*, Phys. Atom. Nucl. **73**, 1322 (2010); I.A. Rachek *et al.*, J. Phys. Conf. Ser. **295**, 012106 (2011).
- [7] I.A. Rachek *et al.*, Few-Body Syst. **58**, 29 (2017); I.A. Rachek *et al.*, Proc. of the 23rd Eur. Conf. on Few-Body Problems in Physics (EFB23), Aarhus, Denmark, August 8-12, (2016); S.A. Zevakov *et al.*, Bull. Russ. Acad. Sci. Phys. **79**, 864 (2015); S.A. Zevakov *et al.*, Bull. Russ. Acad. Sci. Phys. **78**, 611 (2014).
- [8] D.M. Nikolenko *et al.*, Phys. Part. Nucl. **48**, 102 (2017).
- [9] J.H. Koch and R.M. Woloshyn, Phys. Rev. C **16**, 1968 (1977).
- [10] P. Bosted and J.M. Laget, Nucl. Phys. A **296**, 413 (1978); J.M. Laget, Phys. Rep. **69**, 1 (1981).
- [11] P. Wilhelm and H. Arenhövel, Few-Body Syst. Suppl. **7**, 235 (1994); P. Wilhelm and H. Arenhövel, Nucl. Phys. A **593**, 435 (1995); P. Wilhelm and H. Arenhövel, Nucl. Phys. A **609**, 469 (1996).
- [12] H. Garcilazo and E.M. de Guerra, Phys. Rev. C **52**, 49 (1995); H. Garcilazo and E.M. de Guerra, Phys. Rev. C **49**, R601 (1994).
- [13] F. Blaazer, B.L.G. Bakker, and H.J. Boersma, Nucl. Phys. A **568**, 681 (1994); F. Blaazer, B.L.G. Bakker, and H.J. Boersma, Nucl. Phys. A **590**, 750 (1995); F. Blaazer, PhD dissertation (Free University of Amsterdam, 1995).
- [14] A.K. Kerman, H. McManus, and R.M. Thaler, Ann. Phys. (N.Y.) **8**, 551 (1959).
- [15] S.S. Kamalov, L. Tiator, and C. Bennhold, Nucl. Phys. A **547**, 559 (1992); S.S. Kamalov, L. Tiator, and C. Bennhold, Few-Body Syst. **10**, 143 (1991); S.S. Kamalov, L. Tiator, and C. Bennhold, Phys. Rev. C **55**, 98 (1997).
- [16] A.E. Kudryavtsev *et al.*, Phys. Rev. C **71**, 035202 (2005).
- [17] A. Fix, Eur. Phys. J. A **26**, 293 (2005).
- [18] E.M. Darwish, N. Akopov, and M. El-Zohry, AIP Conf. Proc. **1370**, 242 (2011); E.M. Darwish, N. Akopov, and M. El-Zohry, J. At. Mol. Sci. **2**, 187 (2011); E.M. Darwish, N. Akopov, and M. El-Zohry, PoS **ICHEP2010**, 185 (2010); M. El-Zohry, PhD dissertation (Yerevan State University, 2011).
- [19] E.M. Darwish, J. Phys. Soc. Jpn. **83**, 084201 (2014).
- [20] E.M. Darwish and S.S. Al-Thoyaib, Ann. Phys. (N.Y.) **351**, 35 (2014).
- [21] A. Imanishi *et al.*, Phys. Rev. Lett. **54**, 2497 (1985).
- [22] E.M. Darwish and A. Hemmdan, Ann. Phys. (N.Y.) **356**, 128 (2015).
- [23] E.M. Darwish and H. Mansour, *Coherent π -production off deuteron near η -threshold: a theoretical overview* (LAP LAMBERT Academic Publishing, 2015).
- [24] E.M. Darwish and S.S. Al-Thoyaib, J. Phys. Soc. Jpn. **84**, 124201 (2015).
- [25] E.M. Darwish, A. Hemmdan, and N.T. El-Shamy, Int. J. Mod. Phys. E **24**, 1550064 (2015).

- [26] E.M. Darwish, Chin. Phys. Lett. **32**, 122501 (2015).
- [27] E.M. Darwish, Chin. Phys. Lett. **33**, 041301 (2016).
- [28] E.M. Darwish, H.M. Abou-Elsebaa, and K.S.A. Hassaneen, Braz. J. Phys. (2018), in print.
- [29] O. Hanstein, D. Drechsel, and L. Tiator, Nucl. Phys. A **632**, 561 (1998); D. Drechsel, O. Hanstein, S. Kamalov, and L. Tiator, Nucl. Phys. A **645**, 145 (1999); *MAID2003 Program*: <http://wwwkph.kph.uni-mainz.de/MAID/maid2003/>.
- [30] D. Drechsel, S. Kamalov and L. Tiator, Eur. Phys. J. A **34**, 69 (2007); *MAID2007 Program*: <http://wwwkph.kph.uni-mainz.de/MAID/maid2007/>.
- [31] J.D. Bjorken and S.D. Drell, *Relativistic Quantum Mechanics* (McGraw-Hill, New York, 1964).
- [32] H. Arenhövel, Few-Body Syst. **4**, 55 (1988).
- [33] H. Arenhövel, Int. J. Mod. Phys. E **18**, 1226 (2009).
- [34] E.M. Robson, *Elementary Theory of Angular Momentum* (Wiley New York, 1957).
- [35] A.R. Edmonds, *Angular Momentum in Quantum Mechanics* (Princeton University Press, New Jersey, 1957).
- [36] H. Arenhövel, Few-Body Syst. **27**, 141 (1999).
- [37] S.B. Gerasimov, Yad. Fiz. **2**, 598 (1965) [Sov. J. Nucl. Phys. **2**, 430 (1966)]; S.D. Drell and A.C. Hearn, Phys. Rev. Lett. **16**, 908 (1966).
- [38] R. Machleidt, F. Sammarruca, and Y. Song, Phys. Rev. C **53**, R1483 (1996); R. Machleidt, Phys. Rev. C **63**, 024001 (2001).
- [39] M.I. Levchuk *et al.*, Phys. Rev. C **74**, 014004 (2006).
- [40] G.F. Chew, M.L. Goldberger, F.E. Low, and Y. Nambu, Phys. Rev. **106**, 1345 (1957).
- [41] A. Fix and H. Arenhövel, Nucl. Phys. A **697**, 277 (2002).
- [42] A. Fix and H. Arenhövel, Phys. Lett. B **492**, 32 (2000).
- [43] C. Bennhold and H. Tanabe, Nucl. Phys. A **530**, 625 (1991).
- [44] A. Fix and H. Arenhövel, Eur. Phys. J. A **19**, 275 (2004).
- [45] A. Fix and H. Arenhövel, Phys. Rev. C **68**, 044002 (2003).
- [46] V. Hejny *et al.*, Eur. Phys. J. A **6**, 83 (1999).
- [47] J. Haidenbauer, Y. Koike, and W. Plessas, Phys. Rev. C **33**, 439 (1986).
- [48] R. Machleidt, Adv. Nucl. Phys. **19**, 189 (1989).
- [49] C. Fernández-Ramírez, E. Moya de Guerra, and J.M. Udías, Ann. Phys. (N.Y.) **321**, 1408 (2006); C. Fernández-Ramírez, E. Moya de Guerra, and J.M. Udías, Phys. Lett. B **660**, 188 (2008).
- [50] R. Machleidt, K. Holinde, and Ch. Elster, Phys. Rep. **149**, 1 (1987).
- [51] H. Arenhövel, A. Fix, and M. Schwamb, Phys. Rev. Lett. **93**, 202301 (2004); M. Schwamb, Eur. Phys. J. **A28** Suppl. 1, 39 (2006); M. Schwamb, Phys. Rep. **485**, 109 (2010).
- [52] B.D. Day, Phys. Rev. Lett. **47**, 226 (1981); M. Hjorth-Jensen, T.T.S. Kuo, and E. Osnes, Phys. Rep. **261**, 125 (1995).
- [53] A. Imanishi *et al.*, Nuovo Cim. A **100**, 735 (1988).
- [54] A.A. Zayats and A.S. Omelaenko, Sov. J. Nucl. Phys. **34**, 373 (1981) [Yad. Fiz. **34**, 671 (1981)].
- [55] M. Gottschall *et al.*, Phys. Rev. Lett. **112**, 012003 (2014).
- [56] J.A. Gómez Tejedor, S.S. Kamalov, and E. Oset, Phys. Rev. C **54**, 3160 (1996).
- [57] F. Ritz and H. Arenhövel, Phys. Rev. C **64**, 034005 (2001).
- [58] C. Lovelace, Phys. Rev. **135**, B1225 (1964).
- [59] I.R. Afnan and A.W. Thomas, Phys. Rev. C **10**, 109 (1974).
- [60] T. Ueda, Phys. Lett. B **141**, 157 (1984).
- [61] K. Miyagawa, T. Ueda, T. Sawada, and S. Takagi, Nucl. Phys. A **459**, 93 (1986).